LUND UNIVERSITY

Development of optical diagnostics of plasma-related phenomena and applications

Bao, Yupan

2022

Document Version:
Publisher's PDF, also known as Version of record

Development of optical diagnostics of plasma-related phenomena and applications

YUPAN BAO
DIVISION OF COMBUSTION PHYSICS | FACULTY OF ENGINEERING | LUND UNIVERSITY

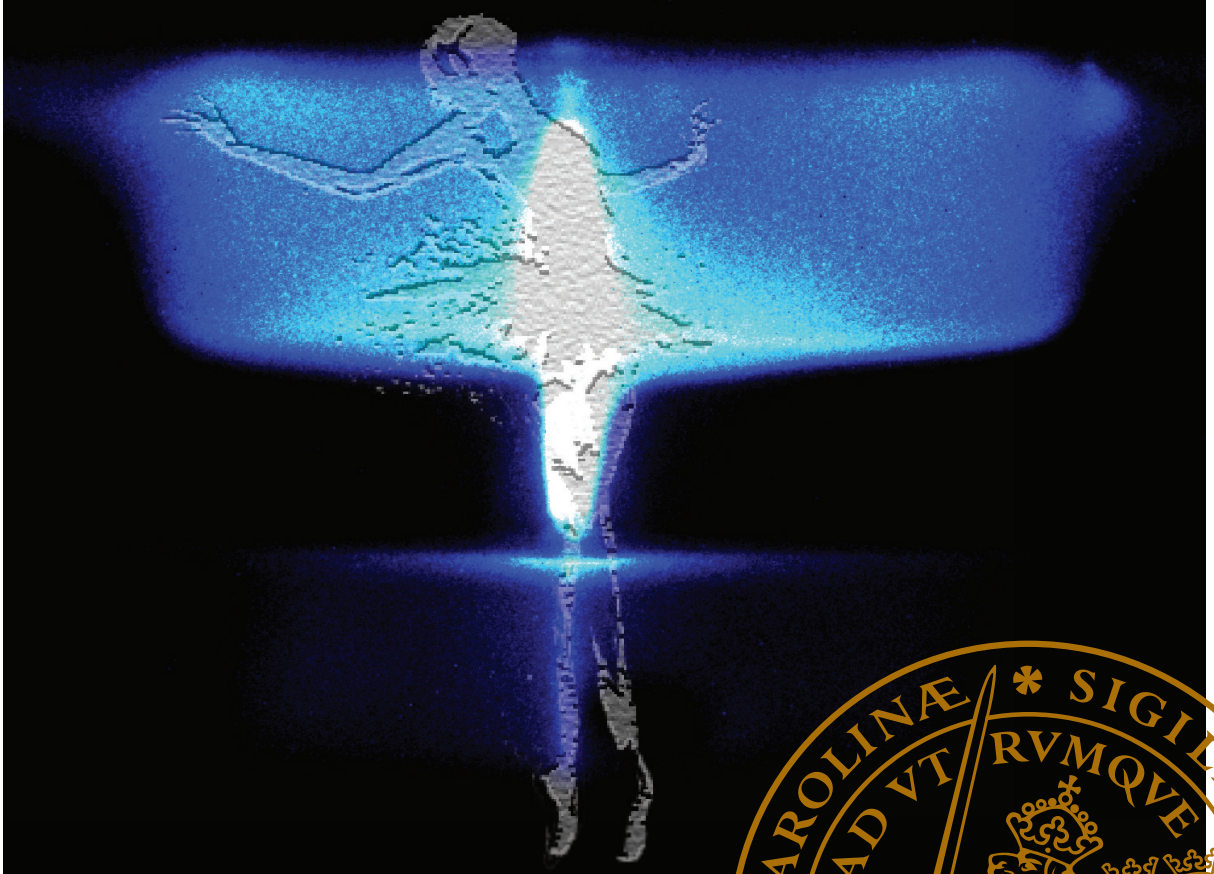

Development of optical diagnostics of plasma-related phenomena and applications

Development of optical diagnostics of plasma-related phenomena and applications

by Yupan Bao

LUND
UNIVERSITY

Thesis for the degree of Physics
Thesis advisors: Dr. Andreas Ehn,
Prof. Joakim Bood, Prof. Marcus Aldén
Faculty opponent: Prof.Christoffer Laux

To be presented, with the permission of the Faculty of Engineering of Lund University, for public criticism in the Rydberg lecture hall (Rydbergsalen) at the Department of Physics on Tuesday, the 5th of April 2022 at 9:15.

Organization
LUND UNIVERSITY

Department of Physics
Box 118
SE–221 00 LUND
Sweden

Document name
DOCTORAL DISSERTATION

Date of disputation
2022-04-05

Sponsoring organization

Author(s)
Yupan Bao

Title and subtitle
Development of optical diagnostics of plasma-related phenomena and applications:

Abstract
Optical diagnostics techniques based on coded imaging were developed and applied for plasma-related phenomena and applications. The signal of interest is first encoded with a sinusoid pattern either by structured laser illumination or implement of a diffractive optical element, such as a grating, along the optical path of the signal. The coded signal will then be extracted from the raw data by a lock-in based algorithm, such as frequency recognition algorithm for multiple exposures (FRAME).

Two types of non-thermal plasma sources, i.e., gliding arc discharges and nanosecond pulsed discharges, were investigated. Volumetric information of molecular distributions around a gliding arc was captured using laser-induced fluorescence with structured illumination and FRAME. Laser scattering imaging during the formation of a nanosecond pulsed discharge on a flat methane-air flame was extracted from luminous plasma emission using structured laser illumination. Furthermore, a technique named periodic shadowing was applied for streak camera measurements, where both higher temporal contrast and effective dynamic range were achieved.

The gliding arc plasma discharge was also applied in an industrial prototype burner as plasma-assisted combustion has been proven to be a promising technique to increase energy efficiency as well as reduce environmentally harmful emission. With the help of 0.1% additional energy, the lean blow-out limit of a hundred kilowatt burner was extended from a global equivalence ratio of 0.47 to 0.45.

Key words
non-thermal plasma, plasma-assisted combustion, laser diagnostics, spectroscopy, coded imaging

Classification system and/or index terms (if any)

Supplementary bibliographical information

Language
English

ISSN and key title

ISBN
978-91-8039-158-0 (print)
978-91-8039-157-3 (pdf)

Recipient's notes

Number of pages
181

Price

Security classification

Development of optical diagnostics of plasma-related phenomena and applications

by Yupan Bao

LUND
UNIVERSITY

A doctoral thesis at a university in Sweden takes either the form of a single, cohesive research study (monograph) or a summary of research papers (compilation thesis), which the doctoral student has written alone or together with one or several other author(s).

In the latter case the thesis consists of two parts. An introductory text puts the research work into context and summarizes the main points of the papers. Then, the research publications themselves are reproduced, together with a description of the individual contributions of the authors. The research papers may either have been already published or are manuscripts at various stages (in press, submitted, or in draft).

Cover illustration front: Image of a flame stimulated by a nanosecond pulsed discharge with a ballet dancer.

Cover illustration back: NyTeknik, Nummer 17, 23 april 2020.

Funding information: This thesis work was funded by the Swedish Research Council (2021-04506, 2015-05321), Knut & Alice Wallenberg Foundation (2019.0084) and the European Research Council (669466, 852394).

Faculty of Engineering, Department of Physics

ISBN: 978-91-8039-158-0 (print)
ISBN: 978-91-8039-157-3 (pdf)
ISSN: 1102-8718

Printed in Sweden by Media-Tryck, Lund University, Lund 2022

To my family

致我的家人

bù yǐ wù xǐ， bù yǐ jǐ bēi

不 以 物 喜， 不 以 己 悲

Contents

Abstract

Optical diagnostics techniques based on coded imaging were developed and applied for plasma-related phenomena and applications. The signal of interest is first encoded with a sinusoid pattern either by structured laser illumination or implement of a diffractive optical element, such as a grating, along the optical path of the signal. The coded signal will then be extracted from the raw data by a lock-in based algorithm, such as frequency recognition algorithm for multiple exposures (FRAME).

Two types of non-thermal plasma sources, i.e., gliding arc discharges and nanosecond pulsed discharges, were investigated. Volumetric information of molecular distributions around a gliding arc was captured using laser-induced fluorescence with structured illumination and FRAME. Laser scattering imaging during the formation of a nanosecond pulsed discharge on a flat methane-air flame was extracted from luminous plasma emission using structured laser illumination. Furthermore, a technique named periodic shadowing was applied for streak camera measurements, where both higher temporal contrast and effective dynamic range were achieved.

The gliding arc plasma discharge was also applied in an industrial prototype burner as plasma-assisted combustion has been proven to be a promising technique to increase energy efficiency as well as reduce environmentally harmful emission. With the help of 0.1% additional energy, the lean blow-out limit of a hundred kilowatt burner was extended from a global equivalence ratio of 0.47 to 0.45.

Popular summary

Plasma, known as the fourth state of matter, is a macroscopically neutral substance consisting of positively and negatively charged particles. Unlike the other three fundamental states of matter (solid, liquid and gas), which exist closely to our everyday life, lightning during a thunderstorm is one of the few naturally stimulated plasma on earth. Earth aside, however, plasma is believed to be the majority of all existing cosmic matter, such as the ionosphere of the Earth (from an altitude of 50 km to several thousands of km), the cosmic wind, and even the sun. Since the 1950's, plasma has been vastly investigated as it is the only physical environment for thermonuclear reactions including nuclear fusion and fission.

The major difference between each state of matter is how strongly particles are bonded to each other. In solid state, for example, particles are bonded so closely and tightly to each other that certain structure is maintained, sometimes in the form of crystal lattice. In liquid state, particles become a bit loose but still attract each other. With higher temperature or lower pressure, the distance between each particles becomes larger and eventually they become independent from each other in gas phase. If the temperature of a gas is increased to certain degree that the energy of the electrons is high enough to escape from an atom or a molecule, leaving the particle become ionized, a high-temperature plasma will be created. High-temperature plasma, also called thermal plasma, has been applied in many industrial applications, such as plasma cutting and plasma propulsion engine for space travel.

The main target of this thesis, however, is the other type of plasma: cold plasma, also named as non-thermal plasma. Unlike thermal plasma, the electron temperature of non-thermal plasma is much higher than the temperature of other heavy particles. The non-thermal plasma, used in this thesis, is produced by accelerating electrons with high voltage to break the bond that connects the electrons and the ions/atoms. In practice, this is achieved in two ways: by a nanosecond (10^{-9} second) pulsed power supply or by an alternating current power supply. For most cases studied in this thesis, the plasma is produced within a combustion system where new chemical reactions and pathways are introduced to assist and/or control the flame. Historically, flame, or more precisely fire, has also been referred to as the fourth classical elements in ancient cultures, along with water, earth and air.

Furthermore, optical diagnostics have been developed to investigate plasma-related phenomena with high temporal and spatial resolution. The optical tech-

niques, that have been developed in this thesis, utilized that an image can be presented either in their spatial domain or in the frequency domain, similar to the wave-particle duality, where every existing thing in the universe can be described as either a particle or a wave. This dual representation of images allows us to mitigate strong plasma luminescence when capturing weak optically-induced signal, and to capture the dynamics and 3D distributions of molecular species in a plasma, to mention a few. We believe these optical techniques are particularly advantageous for diagnosing plasma-related phenomena and applications since plasmas are high energetic and particularly luminous.

科普简介

等离子，即物质的第四态，是由分别带正电和负电的粒子组成的宏观中性物质。与其他三种生活中随处可见的基本物质状态（固体、液体和气体）不同，等离子体与日常生活关系较远。例如，闪电是自然界中为数不多已知的能产生等离子体的自然现象。然而，若离开地球表面，宇宙的绝大部分却被认为是由组成等离子体的。例如，距地球表面 50 公里至数千公里的电离层、太空中的宇宙风，甚至熊熊燃烧的太阳都是等离子体。自 1950 年以来，作为热核反应（核聚变和裂变）的唯一物理环境，等离子体开始被广泛研究。

每类物质状态相互之间能够被区分的主要原因是粒子间彼此结合的强度发生变化。例如，在固态环境下，粒子彼此紧密结合且保持某种特殊结构 （通常以晶格的形式）。在液态条件下，粒子间的作用力变得松散，但仍然相互吸引。随着温度的升高或压力的降低，粒子之间的距离逐渐增大，最终它们在气体状态下相互独立。如果气体的温度进一步升高，电子的能量也会随之升高。当电子的能量高到足以使其从原子或分子中逃逸出时，就会产生高温等离子体。高温等离子体，又称热等离子体，已在许多工业应用中得到广泛的应用，如等离子切割和用于太空旅行的等离子推进发动机等。

本文的主要研究的对象是另一种等离子体：冷温等离子体，也称为冷等离子体。与热等离子体不同，冷等离子体的电子温度远高于其他重粒子（如原子和分子）的温度。本文中使用的冷等离子体是利用在高电压环境下加速的电子破坏连接电子和分子或原子之间的相互作用力而产生的。在实践中，分别通过纳秒（10^{-9} 秒）脉冲电源或交流电源实现。对于本文研究的大多数情况，等离子体是通过某燃烧系统产生的。得益于等离子体的引入，燃烧系统中产生的新的化学反应路径可被用于加强火焰的燃烧和控制火焰的稳定。巧合的是，与等离子作为现在科学的四种基本物质状态之一相似，在古代文化中，火焰（火），也被认为是组成物质的基本元素之一。如古希腊的四元素说（土气水火），印度佛教的四界（地水火风），以及中国的五行（金木水火土）。

除了冷等离子体外，本文也着重于针对等离子体检测的光学诊断技术的发展及研究。本文所研究的光学诊断技术主要基于图像可以分别在空间域或频域呈现的原理，具有高时间分辨率和高空间分辨率的特点。该原理类似于波粒二象性中对任何物质的描述都可以以粒子或波的形态进行，而这种图像的双重表达方式使我们能够在有强等离子体放射光的干扰下捕获到微弱的有效信号，并能通过捕捉到的信号重构等离子体中不同粒子的瞬时动态变化和三维分布等信息。我们相信，研究这些光学诊断技术对于研究等离子体及其相关应用具有很大的帮助。

Populärvetenskaplig sammanfattning på svenska [1]

Plasma, känt som materiens fjärde tillstånd, är ett makroskopiskt neutralt ämne som består av positivt och negativt laddade partiklar. Till skillnad från de andra tre tillstånden av materia (fast, flytande och gas), som finns nära vårt vardagliga liv, blixtar under ett åskväder är en av få naturligt stimulerade plasma på jorden. Bortsett från jorden, tros plasma vara majoriteten av all existerande kosmisk materia, såsom jordens jonosfär (från en höjd av 50 km till flera tusen km), den kosmiska vinden och till och med solen. Sedan 1950-talet har omfattande undersökningar av plasma genomförts eftersom det är den enda fysiska miljön för termonukleära reaktioner inklusive kärnfusion och fission.

Den största skillnaden mellan varje materiatillstånd är hur starkt partiklar är bundna till varandra. I fast tillstånd, till exempel, är partiklar bundna så tätt till varandra att viss struktur bibehålls, ibland i form av kristall. I flytande tillstånd blir partiklar lite lösa men attraherar fortfarande varandra. Med högre temperatur eller lägre tryck blir avståndet mellan varje partikel större och så småningom blir de oberoende av varandra i gasfas. Om temperaturen på en gas höjs till en viss grad så att elektronernas energi är tillräckligt hög för att fly från en atom eller en molekyl, vilket gör att partikeln blir joniserad, skapas ett högtemperaturplasma. Högtemperaturplasma, även kallad termisk plasma, har använts i många industriella tillämpningar, såsom plasmaskärning och plasmaframdrivningsmotorer för rymdresor.

Fokus för denna avhandling är dock den andra typen av plasma: kall plasma, även kallad icke-termisk plasma. Till skillnad från termisk plasma är elektrontemperaturen för icke-termisk plasma mycket högre än temperaturen för andra tunga partiklar. Den icke-termiska plasman, som används i denna avhandling, produceras genom att accelerera elektroner med hög spänning som kan bryta bindningen som förbinder elektronerna och jonerna/atomerna. I praktiken uppnås detta på två sätt: med en nanosekund (10^{-9} sekund) pulsad strömförsörjning eller genom en växelströmskälla. För de flesta fall som studeras i denna avhandling produceras plasman i ett förbränningssystem där nya kemiska reaktioner och vägar introduceras för att assistera och/eller kontrollera lågan. Historiskt sett har låga, eller mer exakt eld, också kallats de fjärde klassiska elementen i antika kulturer, tillsammans med vatten, jord och luft.

Vidare har optisk diagnostik utvecklats för att undersöka plasmarelaterade fenomen med hög tids- och rumsupplösning. De optiska teknikerna, som har utvecklats i denna avhandling, utnyttjade att en bild kan presenteras antingen i

[1] Den svenska texten är översatt av Sebastian Nilsson.

deras rumsliga domän eller i frekvensdomänen, liknande våg-partikeldualiteten, där varje existerande sak i universum kan beskrivas som antingen en partikel eller en våg. Denna dubbla representation av bilder tillåter oss att dämpa den starka plasmaluminiscensen för att kunna se svag optiskt inducerad signal och att fånga 3D-fördelningar av molekylära arter i en plasma är några exempel på användingsområden. Vi tror att dessa optiska tekniker är särskilt fördelaktiga för att diagnostisera plasmarelaterade fenomen och tillämpningar eftersom plasma är högenergiskt och ljusstark.

List of publications

I **Improved temporal contrast of streak camera measurements with periodic shadowing**
Y. Bao, V. Kornienko, D. Lange, W. Kiefer, T. Eschrich, M. Jäger, J. Bood, E. Kristensson and A. Ehn
Optics Letters, 46(22)(2021), 5723-5726

II **Single-shot 3D imaging of hydroxyl radicals in the vicinity of a gliding arc discharge**
Y. Bao, K. Dorozynska, P. Stamatoglou, C. Kong, T. Hurtig, S. Pfaff, J. Zetterberg, M. Richter, E. Kristensson and A. Ehn
Plasma Sources Science and Technology, 30.4(2021), 04LT04

III **Plasma discharge effects on swirl flames in a scaled Siemens energy dry low emission burner**
X. Liu, A. Subash, **Y. Bao**, Z. Li, A. Ehn, T. Hurtig, J. Larfeldt, D. Lörstad, T. Nilsson and C. Fureby
Manuscript accepted in AIAA Journal

IV **Experimental Investigation of the Influence of Plasma Discharge on Flame Characteristics at a Siemens Dry Low Emission Industrial Prototype Burner under Atmospheric Conditions**
A. Subash, X. Liu, **Y. Bao**, T. Hurtig, J. Larfeldt, C. Fureby and A. Ehn
Manuscript to be submitted

V **Formation dynamics of a four-nanosecond single-pulse plasma in a flat flame at atmospheric pressure**
Y. Bao, K. Zhang, C. Kong, T. Hurtig and A. Ehn
Manuscript submitted to the Proceedings of the Combustion Institute

VI **Experimental study of the effect of a single nanosecond discharge pulse on a flat CH_4-Air flame at atmospheric pressure**
C. Kong, **Y. Bao**, J. Ravelid, K. Zhang, T. Hurtig, J. Bood and A. Ehn
Manuscript in preparation

Related Work

Hydroxyl radical dynamics in a gliding arc discharge using high-speed PLIF imaging
Z. Wang, P. Stamatoglou, C. Kong, J. Gao, **Y. Bao**, M. Aldén, A. Ehn and M. Richter
Manuscript submitted to Plasma Research Express.

A rotating gliding arc discharge in a scaled Siemens dry low emission burner
A. Subash, **Y. Bao**, X. Liu, J. Larfeldt and C. Fureby, A. Ehn and T. Hurtig
Manuscript to be submitted.

Author contributions

Paper I: Improved temporal contrast of streak camera measurements with periodic shadowing
Y. Bao, V. Kornienko, D. Lange, W. Kiefer, T. Eschrich, M. Jäger, J. Bood, E. Kristensson and A. Ehn
Optics Letters, 46(22)(2021), 5723-5726

I prepared and performed the experiment together with V. Kornienko. I analyzed the data with V. Kornienko. I wrote the manuscript with V. Kornienko, with help from all other co-authors. I was the main responsible for this paper.

Paper II: Single-shot 3D imaging of hydroxyl radicals in the vicinity of a gliding arc discharge
Y. Bao, K. Dorozynska, P. Stamatoglou, C. Kong, T. Hurtig, S. Pfaff, J. Zetterberg, M. Richter, E. Kristensson and A. Ehn
Plasma Sources Science and Technology, 30.4(2021), 04LT04

I prepared the optical set-up together with K. Dorozynska, with help from A. Ehn, E. Kristensson and S. Stamatoglou. I prepared the gliding arc set-up together with C. Kong. K.Dorozynska, P. Stamatoglou and I performed the experiment together. I analyzed the data, with help from K. Dorozynska, E. Kristensson and A. Ehn. I wrote the paper, with help from K. Dorozynska and A. Ehn and input from all co-authors. I was the main responsible for this paper.

Paper III: Plasma discharge effects on swirl flames in a scaled Siemens energy dry low emission burner
X. Liu, A. Subash, **Y. Bao**, Z. Li, A. Ehn, T. Hurtig, J. Larfeldt, D. Lörstad, T. Nilsson and C. Fureby
Manuscript accepted in AIAA Journal

I participated in the performance of this experiment.I was actively involved in the discussions regarding the data analysis, interpretation of the results and writing the manuscript. I was main responsible for analyzing and writing the spectrum results.

Paper IV: Experimental Investigation of the Influence of Plasma Discharge on Flame Characteristics at a Siemens Dry Low Emission Industrial Prototype Burner under Atmospheric Conditions
A. Subash, X. Liu, **Y. Bao**, T. Hurtig, J. Larfeldt, C. Fureby and A. Ehn
Manuscript to be submitted

I participated in the performance of this experiment.I was actively involved in the

discussions regarding the data analysis, interpretation of the results and writing the manuscript. I was main responsible for analyzing and writing the spectrum results.

Paper V: Formation dynamics of a four-nanosecond single-pulse plasma in a flat flame at atmospheric pressure
Y. Bao, K. Zhang, C. Kong, T. Hurtig and A. Ehn
Manuscript submitted to the Proceedings of the Combustion Institute

I prepared and preformed the experiment with help from K. Zhang. I analyzed the data. I wrote the manuscript with A. Ehn, with input from all other co-authors. I was the main responsible for this paper.

Paper VI: Experimental study of the effect of a single nanosecond discharge pulse on a flat CH_4-Air flame at atmospheric pressure
C. Kong, **Y. Bao**, J. Ravelid, K. Zhang, T. Hurtig, J. Bood and A. Ehn
Manuscript in preparation

I prepared and preformed the experiment with C. Kong for the formaldehyde and temperature measurements. I prepared and preformed the experiment for the spectroscopy, with help from J. Ravelid. I analyzed the data for the temperature and spectrum measurements. I helped C. Kong in writing with my main responsible for the sections related to the temperature and spectrum results.

Chapter 1

Introduction

Plasma originated from the Ancient Greek word $\pi\lambda\acute{\alpha}\sigma\mu\alpha$ (something moldable), and was first systematically studied by Tonks and Langmuir in the 1920s [1, 2, 3]. Abundant in the universe, plasma is created when electrons are detached from an atom or a molecule. Bonded electrons can be knocked out, for example, by collisions between fast moving atoms/molecules/electrons or by absorption of high energy photons. Depending on the temperature, plasma can be categorized in two major types: thermal plasma and non-thermal plasma. Thermal plasma, or hot plasma, refers to the kind of plasma which has reached thermodynamic equilibrium in which the temperature of the electrons and gas are the same. On the other hand non-thermal plasma, or cold plasma, contains electrons with temperatures much higher than the gas (for example, $T_{electron} \approx 10000$ K while $T_{gas} \approx 1000$ K). Typical ranges of the electron temperature and electron density

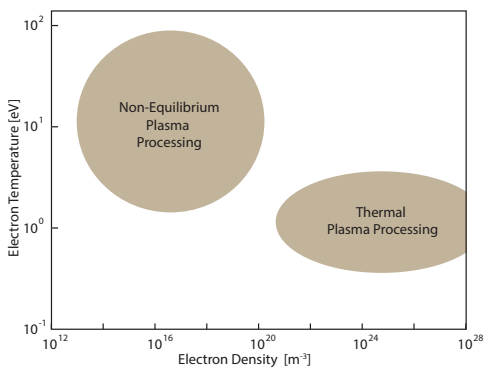

Figure 1.1: Typical ranges of the electron temperature and electron density of thermal and non-thermal plasmas. Figure adapted from [4].

of thermal and non-thermal plasma is given in figure 1.1.

To reach thermodynamic equilibrium, thermal plasma is formed at either extremely high temperatures, e.g., along with nuclear fusion reactions such as within the sun, or by applying electrical energy strong and long enough such that the gas temperature and electron temperature are equilibrated by collisions and recombination of electrons and charged particles, such as an electric arc or a continuous microwave plasma. Non-thermal plasma, on the contrary, keeps most of the thermal energy in electrons and contains a large amount of high-energetic electrons without excessive heating of the gas. This feature, i.e., being chemically active due to the massive amounts of free electrons produced with high energy efficiency, makes non-thermal plasma a robust technology in many industrial and scientific applications [5], e.g., air pollution control [6, 7, 8], surface treatment [9, 10], hydrocarbon/methane/ethanol reforming [11, 12], analytical chemistry [13], analytical spectrometry [14], wound healing [15], tooth bleaching [16], anti-coagulation of blood [17] and plasma-assisted combustion (PAC) [18, 19].

Energy is essential for industrialized society. Energy sources that are clean, affordable and reliable is urgently needed to avoid excessive damage to the environment. Plasma-assisted combustion has been proven to be a promising technique to increase energy efficiency and reduce environmentally harmful emission [18, 19], which are among the most important solutions for sustainable energy according to the perspective article published in *Nature* 2012 [20]. Over the last decades, PAC has been found to be able to significantly extend the flame explosion limit [21] and lean blow-off limit of an engine [22, 23], as well as reduce the ignition energy and the flame initiation time [18] . Kinetics studies of PAC show that O_3 [24], $O_2(^1_a\Delta_g)$ [25] and atomic O [26, 27] created by a plasma are key species for PAC in lean conditions. In this thesis, two kinds of non-thermal plasma are studied for plasma-assisted combustion: a glow-type gliding arc discharge and a nanosecond pulsed discharge (NPD).

The alternating current (AC) gliding arc discharge with an average power around 80 W has been applied in a down-scaled Siemens Energy burner with thermal power between 78-98 kW (see figure 1.2a). With the help of additional 0.1 % total power, the lean blow-out limit (LBO) of the burner has been extended from global equivalence ratio of 0.47 to 0.45 without any significant increase of nitrogen oxides (NO_x) emissions. More discussions about the this work can be found in paper III, IV, and section 4.3.

The nanosecond pulsed discharge with a pulse duration of 4 ns (FWHM) has been applied on a lifted flat methane-air flame (see figure 1.2b). Different from

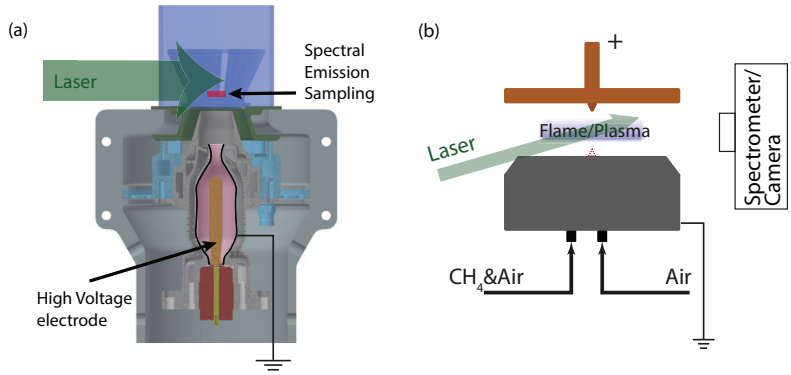

Figure 1.2: (a) Sketch of the Siemens Energy Dry Low Emission burner (SGT-750). (b) Sketch of the flat flame for nanosecond pulsed discharge.

most reported studies of NPD which operated with a repetitive frequency from tens to hundreds of kilohertz, investigation of the NPD in this thesis is focused on single pulse stimulation. Flame speed, gas temperature, rotational and vibrational temperature acquired from $N_2(C)$ spectrum, distribution of formaldehyde and the images of the laser scattering signals have been measured using different optical diagnostic techniques. More discussions about the this work can be found in paper V, VI, and section 4.4.

While current and voltage information can be measured with electrical methods for investigations of plasma and plasma-assisted combustion, many other parameters are measured using optical diagnostics. Accurate measurements, with high spatial and temporal resolution, for dynamics, radical and active species distributions, electron density, gas temperature, and electron temperature, to name a few, are crucial for understanding different plasma mechanisms, fundamental chemistry and dynamic processes of plasma-assisted combustion. A summary of optical diagnostics for different parameters of non-thermal plasma, including relevant references, can be found in table 1.1 (page 8) of Dr.Zhu's PhD thesis [28].

Development of advanced optical diagnostics, as another task for this thesis, is focused on solving one major problem of optical diagnostics for plasma-related phenomena and applications: background interference of plasma emission. Plasma emission refers to the strong, continuous and broadband spontaneous emission from excited species in a plasma. For plasma interacting with ambient air, where nitrogen is the major species, most of the plasma emission comes from excited nitrogen, N_2^*. A straightforward and frequently-used method to avoid plasma emission for laser-related diagnostics is to apply a very short camera gate of several nanosecond using, for example, an iCCD camera.

Images given in figure 1.3 show two examples where both plasma emission and laser-induced fluorescence (LIF) of hydroxyl radicals (OH) are captured. Since the LIF signal has a lifetime of a few nanoseconds, a camera gate of 10 ns is long enough to capture all LIF signal with minimal plasma emission (figure 1.3, left). However, when the signal of interest is too weak (figure 1.3, right), it is impossible to distinguish the signal from the plasma emission interference by simply using a short camera gate.

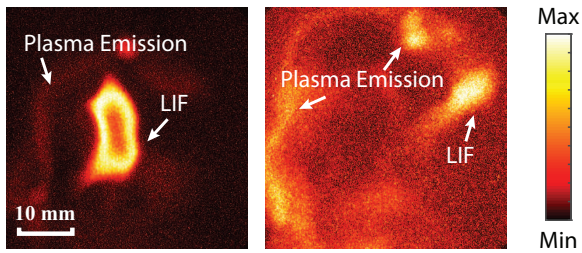

Figure 1.3: Typical signal of planar laser-induced fluorescence of OH with plasma emission from a gliding arc discharge (single shot image with 10 ns gate). The signal to interference ratios are 6:1 (left) and 1:1 (right). Figure adapted from paper II.

Optical diagnostic techniques based on coded imaging were developed and introduced to diagnostics of plasma-related phenomena in this thesis. With the signal of interest coded with a certain modulation, plasma emission can be automatically removed by lock-in analysis. In paper I, periodic shadowing is applied in streak camera measurements for development of ultrafast phenomena with high temporal contrast. In paper II, volumetric information of OH distributions around gliding arc discharges are given by laser-induced fluorescence with the frequency recognition algorithm for multiple exposures (FRAME) technique. In paper V, structured illumination is applied on laser scattering measurement to capture the formation dynamic of a nanosecond pulsed discharge on a flat methane-air flame.

Fundamentals of the plasma discharge and optical diagnostics employed in this thesis are given in Chapter 2. Principles of coded imaging and lock-in analysis are demonstrated in Chapter 3, together with optical techniques where they have been implemented. Experimental set-up and results of four projects related to (1) streak camera, (2) volumetric study of OH around a gliding arc, (3) PAC on a prototype industrial burner and (4) nanosecond pulsed discharge, are presented in Chapter 4. Finally a short conclusion and potential possibilities for future activities are discussed in Chapter 5.

Chapter 2

Plasma discharge and optical diagnostics

In this chapter, fundamentals of plasma discharge and optical diagnostics are discussed. Various references are included with focus on the two types of non-thermal plasma that have been used in this thesis: gliding arc discharge and nanosecond pulsed discharge. The three most frequently used optical diagnostic techniques for plasma-related diagnostics are discussed in details: optical emission spectroscopy, laser-induced fluorescence and laser-induced scattering.

2.1 Plasma Discharge

2.1.1 Fundamental of Plasma Physics

An indispensable property, or the most important criteria, of a plasma is its macroscopic neutrality. A substance can not be called a "plasma" if it is not electronically neutral. Hence, the most fundamental parameter for plasma is: the *Debye length*, the largest distance where the macroscopic neutrality of a plasma can be obtained without any external forces. The *Debye length*, λ_D, is defined as [1, 2, 3]

$$\lambda_D = \sqrt{\frac{\epsilon_0 k_B T_e}{n_e q_e^2}} \tag{2.1}$$

where ϵ_0 is the permittivity of free space, k_B is the Boltzmann's constant, T_e is the electron temperature, n_e is the electron number density and q_e is the charge of an electron. A typical number for the *Debye length* is 10^{-4} m for a gas discharge, 10^{-3} m for the Earth's ionosphere and could be several meters in space.

The sphere with radius equal to the *Debye length* is defined as the *Debye sphere*. As a result of the collective electromagnetic field of all the charged particles inside said *Debye sphere*, all the charged particles within it are screened off from any electrostatic field outside. This effect is called *Debye shielding effect*. In order to make it work, the dimension of a plasma should be much larger than the *Debye length* while the average distance between electrons ($\approx n_e^{1/3}$) should be much smaller than the *Debye length*. This criterion is defined as the *plasma approximation*, where the *plasma parameter*, normally denoted Λ (also referred to as g in some text books)

$$\Lambda = \frac{1}{n_e \lambda_d^3} \tag{2.2}$$

should be much higher than 1.

To maintain its macroscopic neutrality while experiencing external electromagnetic disturbances, a plasma will oscillate like a spring. The oscillation frequency of this movement is called *plasma frequency*. Similar to a spring, the oscillation of the plasma can be defined as

$$\frac{\partial^2 n_e'(\mathbf{r}, t)}{\partial t^2} + \omega_{pe}^2 n_e'(\mathbf{r}, t) = 0 \tag{2.3}$$

where ω_{pe} is the plasma frequency:

$$\omega_{pe} = (\frac{n_0 e^2}{\epsilon_0 m})^{1/2} \tag{2.4}$$

with n_0 the number density of the ions and m the effective mass of the electron..

2.1.2 Gas Breakdown

- **Townsend Breakdown** Townsend breakdown is a gas ionization process where free electrons are accelerated by an external electric field. The electrons will collide with gas molecules, and additional electrons will be produced due to a multiplication of avalanches. The initial free electrons are mainly produced from the metal surface of the cathode, from where electrons escape in the form of thermionic emission (with heating), field electron emission (with an external electric field) or a combination of both. For an electron generated from the cathode, the number of ionization events performed by it when travelling from cathode to anode is characterized by the *ionization coefficient* (also named as *Townsend's coefficient* for ionization) $\alpha\ cm^{-1}$ given as

  $$dN_e/dx = \alpha N_e \tag{2.5}$$

  where N_e is the number of electrons and x is the path length. As one electron will be kicked out for each ionization event, for electrodes separated with a distance of d, the number of electrons reaching the anode without any secondary electron emission will be $N_0 e^{\alpha d}$, i.e., the current will be $i = i_0 e^{\alpha d}$ given an initial current $i_0 = eN_0$. This process is defined as the avalanche of the electrons.

  To sustain a discharge, secondary electron emission and multiplication of avalanches is required. Secondary electron emission refers to the production of electrons by particles such as ions and photons that are created or altered by the primary electrons. If only considering the ion-electron emission, the current leaving the cathode can be given as

  $$i = i_0 + \gamma_i i_0 (e^{\alpha d} - 1) \tag{2.6}$$

  where γ_i is the *secondary ion-electron emission coefficient*, representing the number of electrons emitted per incident positive ion, and $i_0(e^{\alpha d} - 1)$ is the number of ions created by primary electrons that has travelled back to the cathode. The current includes all these electrons arriving at the anode will then be

  $$i_2 = i_0(1 + \mu)e^{\alpha d} \tag{2.7}$$

with

$$\mu = \gamma_i(e^{\alpha d} - 1) \tag{2.8}$$

In this way, the current with a third (or n) number of avalanches can be written as

$$\begin{aligned} i_3 &= i_0(1 + \mu + \mu^2)e^{\alpha d} \\ &... \\ i_n &= i_0(1 + \mu + \mu^2 + ... + \mu^n)e^{\alpha d} = \frac{1 - \mu^n}{1 - \mu} i_0 e^{\alpha d} \end{aligned} \tag{2.9}$$

If other processes such as photoemission and electrons induced by metastable atoms are also included, the *effective secondary emission coefficient*, γ, is used instead of γ_i. Furthermore, equation 2.9 will hold with $\mu = \gamma(e^{\alpha d} - 1)$ instead of equation 2.8. Detailed discussion about γ can be found in many text books about discharge physics. For example, the effective secondary emission coefficient for both ion-electron emission and photoemission can be given as

$$\gamma = \gamma_i + \gamma_\mu \zeta \alpha_\mu / \alpha \tag{2.10}$$

where γ_μ is the *photoemission secondary emission coefficient*, ζ is the probability of a photon reaching the cathode without being absorbed and α_μ is the number of photons emitted by ionized particles produced by one electron per centimeter.

As given in equation 2.9, if $\mu > 1$, the current will increase to infinity and would thus lead to a breakdown. A discharge is defined as self-sustaining if $\mu = 1$. Applying $\mu = \gamma(e^{\alpha d} - 1) = 1$ and a conventional empirical formula for α proposed by Townsend:

$$\alpha = Ape^{-Bp/E} \tag{2.11}$$

where A and B are determined by experimental measurements, the Paschen's law is introduced by which the breakdown voltage for electrodes with a space of d can thus be given as

$$V = Ed = \frac{Bpd}{C + pd} \tag{2.12}$$

where $C = ln\frac{A}{ln(1/\gamma+1)}$. Examples of the Paschen curve of several gases are given in figure 2.1 where the breakdown voltage V is plotted dependent on the product of the pressure and space between the electrodes as pd.

As a multiplication of electron avalanches is required, the breakdown time of a Townsend breakdown is usually of the order of 10^{-5} s to 10^{-3} s. At

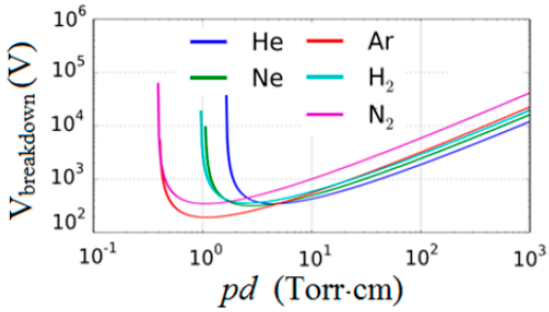

Figure 2.1: Paschen curves for five different gases at 760 Torr. Figure reproduced from [29].

high *pd* or with high-voltage pulses, where luminous plasma emission from the breakdown can be achieved within a few nanoseconds, the Townsend breakdown mechanism is no longer valid, as there is no time for the ions to travel to the cathode. Such a scenario can be interpreted by the streamer process instead.

- **Streamer Process** Streamer theory applies when the electric field induced by avalanches and photon ionization is not negligible ($\alpha d >> 1$) as the space-charge field strength is on the same order as the applied filed. The streamer can be treated as "a weakly ionized thin channel formed from the primary avalanche in a sufficiently strong electric field" [30]. If secondary avalanches, initiated by electrons generated by e.g. photon emission from excited atoms/molecules, are strong enough such that the number of electrons created by them is large, the avalanche exhausts its reserves of amplification. In this case a streamer will be formed. Once a streamer is formed, the current will increase abruptly and strong plasma emission will be observed immediately. If the streamer is formed at the anode surface where the maximum number of space charge is achieved, it will propagate to the cathode and is called "cathode-directed" or "positive". This is usually the situation for plane electrodes. However, if the number of electrons increases very fast, for example, with very high-voltage field and/or a pin-to-pin electrode configuration, the avalanche can transform into a streamer before reaching the anode. If the streamer is formed not far from the cathode and mostly propagates towards the anode, it will be called "anode-directed" or "negative". Detailed discussions of mechanisms and formation criteria for different streamers can be found in Chapter 12 of the reference [30].

2.1.3 Gas Discharge

There are many different ways to categorize different discharges, for example, by the geometry of the electrodes, dielectric barrier discharges (DBD), plasma jets, gliding arcs and hollow cathode discharges. By the properties of the electric field, there are radio frequency discharges, microwave discharges and nanosecond discharges. By the different breakdown processes, the major kinds of discharge are listed below [30]:

- **Dark discharge** Dark discharge describes the situation when the current is extremely small ($10^{-10} \approx 10^{-5}$ A) such that the ionization is too small to emit any appreciable light. When the current is large enough, a dark discharge can transform to a glow discharge.

- **Glow discharge** Glow discharge is a stable discharge that is characterized as a self-sustaining discharge with a cold cathode emitting electrons due to secondary emission. A potential drop of several hundred volts is usually observed at the surface of the cathode with a typical current from 10^{-4} A to 10^{-1} A (this is necessary for the glow discharge to be self-sustaining).

- **Arc discharge** Arc discharge is a result of the current increase of a glow discharge. It is quasi-steady and self-sustaining. Instead of several hundred volts, as for a glow discharge, the potential fall is only about 10 V for arc discharge. As the current is high ($\approx 1 - 10^5$ A), the cathode will be heated up and thermionic emission of electrons will dominate instead of secondary electron emission induced by positive ions. In some extreme cases, a significantly abrupt increase in current can create a spark discharge.

- **Spark discharge** Spark discharge is a transient discharge resulting from the dramatic increase of current after the breakdown channel has been developed throughout the entire gap between the cathode and anode. It is formed most likely at atmospheric pressure or above when the voltage reaches the breakdown level of a gap usually longer than 1 cm. Lightning, for example, is a spark discharge where the breakdown takes place between two clouds or between a cloud and the ground. A spark usually comes with a sound, as in a spark plug of an engine or the thunder during lightning. The sound comes from the shock wave generated by the rapid change in pressure caused by a massive release of Joule heat as a high current passes through the spark channel.

- **Corona discharge** Corona discharges will occur when and only when the field is sharply non-uniform. Otherwise, an increase of voltage between

the electrodes will only lead to a spark. For a corona discharge, the field near one or both electrodes must be much stronger than the remainder of the gap. A typical situation is when the characteristic size r of the electrodes is much smaller than the gap between two electrodes (d). For extreme cases, corona discharge can be formed even without any ground electrode. Similar to the streamer process, corona discharge can be either "positive" or "negative". Unlike an arc or a spark which often accompanies by bright plasma emission, the luminosity of a corona is rather weak.

2.1.4 Non-thermal Plasma

To avoid excessive gas heating, non-thermal plasmas are usually created with a limited current. Non-thermal plasma sources are more often characterized by either the configuration of the electrodes, such as dielectric barrier discharge [31, 32], plasma jets [33], hollow cathode discharges [34] and gliding arcs [35], or by the properties of the electric field, such as radio frequency discharge [36], microwave discharges [37] and nanosecond discharges [38]. Whereas in terms of the physical properties, glow discharge and corona discharge are the two major sources of non-thermal plasma. A review of different non-thermal plasma sources and various applications can be found in [39].

Glow discharge refers to a stable and self-sustaining discharge with a cold cathode emitting electrons due to secondary emission. Most of the applications of glow discharge are carried out at low pressures (a few torr) [40] as the plasma/discharge tends to translate to an arc discharge (a thermal plasma) at atmospheric pressure. However, stable atmospheric-pressure glow discharge has been achieved under special conditions, e.g. (1) using Helium as dilute gas, (2) applying a high-frequency (from kHz to radio frequency) source, (3) inserting an insulating plate on one of the electrodes or having a brush-style upper electrode [41, 42, 43]. The atmospheric glow-type gliding arc discharge plasma used in this thesis is produced by an AC power supply with a frequency of 35 kHz.

Corona discharge [44] occurs when and only when the electric field is sharply non-uniform. A weakly ionized plasma will be created adjacent to ($\approx$ 1 mm) the sharp edge as the local field is much stronger than the breakdown strength of the gas. If the remaining gas also breaks down, e.g. too high voltage or pure voltage increase without non-uniform configuration, a spark discharge will be formed [30]. To circumvent the transition to a spark discharge with increasing voltage (for higher power and better efficiency), a pulsed corona can be applied [45].

At atmospheric pressure, the glow-to-arc transition and corona-to-spark transition can be prevented in many different ways. Dielectric barrier discharge (DBD), first invented in 1857 by Werner von Siemens [46] for ozone generation, is the most widely used approach. The core of DBDs is the dielectric material between the two electrodes, which limits the average current density and unify the distribution of the discharge. Since the limitation on current is less effective at high frequencies, DBDs are normally operated below 10 MHz [31] with the electron temperature of 1-10 eV [32]. During the past century DBD has been applied in many applications including air pollution control [6, 7], surface treatment [47], silent discharge (SD) CO_2 lasers [48, 49], excimer UV lamps [50, 51], analytical chemistry [13], analytical spectrometry [14], skin treatment [15, 52] and anti-coagulation of blood [17].

Due to the restricted volume where the plasma can be formed, corona discharge and DBD have limited performance in many applications, such as material processing (e.g. polyimide etching [53]) and some medical applications (e.g. skin treatment [54]). Plasma jet and hollow cathode discharge (HCD) stand out in these applications. In a plasma jet, the discharge is normally generated by radio frequency power within two concentric electrodes filling with gases. The ionized particles will exit the jet through a nozzle with the velocity typically around 10 cm/s [33]. Considerable concentration of the active species can be measured at less than 10 cm from the exit [54, 55]. In a hollow cathode, the break down voltage is lower while the number of charged particles are orders of magnitude higher due to the hollow cathode effects such as the pendulum effect, i.e. secondary electrons created by electrons oscillating in the tube [34]. At atmospheric pressure, the diameter of the hollow cathode are in micrometer range and hence referred to as microhollow cathode discharge (MHCD).

Radio-frequency (RF) [56] discharge and microwave discharge [37] refer to discharges generated by electromagnetic waves in the wavelength of RF (typically 13.56 MHz [56]) and microwave respectively (typically 2.45 GHz [37]) . RF discharges are most often used as ion sources where the RF field is induced by the alternating current surrounding a dielectric tube which is filled with target gas, such as in a RF-plasma jet. Microwave discharge, unlike other sources, does not need any electrodes. The freedom of its configuration allows it to be generated in various environment (even in free space). However, auxiliary components required for generation of microwave discharge make it rather expensive [57].

2.1.5 Gliding Arc Discharge

A gliding arc discharge (GAD) is a quasi-equilibrium plasma column that is ignited in the narrowest gap between two diverging electrodes in a laminar or turbulent gas flow. When generated, the plasma is close to thermal equilibrium but the gas temperature will soon fall to about 1000 - 2000 K while the electron temperature remains around 0.8 eV (9000-10000 K) [58, 59]. This feature is very attractive for efficiently accelerating chemical-reactivity as the high-temperature electrons generates reactive species and up to 45% of the electrical energy could be directly absorbed in endothermal reactions [35]. Compared to other non-thermal plasma sources, the gliding arc discharge is widely used for its simplicity, feasibility at atmospheric pressure and economically accessibility. In recent years, in addition to these conventional applications as mentioned above, GAD has also been used in CO_2/CH_4 conversion [60, 61, 62] and toluene removal [63, 64].

Due to the complexity of a GAD, in terms of arc-to-glow transition, 3D geometry of the discharge, the formation of cathode spots [65], different interactions with the various gas flow conditions, a comprehensive model of GAD is still under development. By assuming the supplied power and energy losses of the plasma column are homogeneously distributed, a simple model developed from Ohm's law [66, 67] can show that the transition from thermal to non-thermal plasma of a DC discharge happens when the arc length reaches the critical value,

$$l_{crit} = V_0^2/(4WR) \tag{2.13}$$

where V_0, W and R are the voltage, power per unit length and internal resistance of the power supply. While some researchers reported that a fast transition to non-thermal plasma will take place when discharge column exceeds the critical value and the column can be stretched as long as three times larger than the critical length until a short-cut takes place in the upstream [59, 66, 68], other groups [69] questioned this observation believing the transition between thermal to non-thermal is smooth. The length, radius and (reduced) electric filed of the after-transition plasma column is of critical importance as such period has a low enough gas temperature for applications in general material processing techniques [70]. The most direct proof of the existence and good characters of non-thermal plasma is the measurements of translational, rotational, vibrational and electron temperatures. The rotational and vibrational temperature can be obtained from the emission spectra, such as N_2 $(C-B, \Delta\nu = -2, -1, 0)$ bands [59], NO $A-X(0,1)$ and OH $A-X(0,0)$ bands [58, 71]; the translation temperature could be measured by planar laser-induced Rayleigh scattering [58]; and the electron temperature can be estimated using the translational temperature,

the length of the plasma column and the voltage over the arc column that have been measured simultaneously [58].

2.1.6 Nanosecond Pulsed Discharge

Nanosecond pulsed discharges (NPD) refers to the discharge that are generated by high-voltage pulse supply with pulse duration less or around 10 ns (FWHM). Nanosecond pulsed discharge and sub-picoosecond pulsed discharge (with a pulse duration up to several hundreds nanoseconds) have been used to generate non-thermal plasma for many decades. For example, NPD demonstrated both higher energy efficiency and removal ratio for NO removal compared with other discharge methods such as DBD [72]. High efficient synthesis of MoO_3 nanoscale architectures was achieved by a 40 ns discharge without any catalysts or external substrate heating [73]. Repetitive NPD has been applied in large facilities with total thermal power above 50 kW to extend the operating conditions of the flame [22, 23]. A review of plasma-assisted ignition and combustion using NPD can be found in [74] including both experimental measurements and kinetic mechanisms.

Pulse duration and the rise time of the high-voltage NPD are two very important parameters for the plasma generated. Studies has shown that the shorter the pulse is, the higher the yields for active radicals will be [75, 76]. Higher yields for reactive species are often connected to lower heat release, where less energy is used on heating of the gas. For sub-picosecond pulsed discharges longer than 100 ns, thermal plasma can be built through a streamer-glow-arc process [77].

2.2 Optical diagnostics of plasma discharge

Optical diagnostics, especially laser-based methods, have been applied for plasma-related applications at atmospheric pressure in recent years, as they can be used for in-situ and non-intrusive measurements with high spatiotemporal resolution [78, 79]. Frequently used optical diagnostic methods that have been applied for diagnostics of plasma-related phenomena are Laser-Induced Rayleigh Scattering for measurement of gas temperature [58], Optical Emission Spectroscopy for electron [80], rotational and vibrational temperatures [58, 59, 71] along with the distribution of excited species [81], Planar Laser-Induced Fluorescence (PLIF) for distribution of ground-state species [63], and high-speed photography for dynamic processes [82].

2.2.1 Light-matter interaction

When light passes through a cloud of particles, it can interact with the them. The interaction between incident light and an atom/molecule/electron can be categorized into three different processes: elastic scattering, inelastic scattering and excitation of an atom/molecule (see figure 2.2a). Elastic scattering refers to the scattering of light where the wavelength of the scattered light remains the same, i.e., no energy exchange between the photon and the particle occurs. Elastic scattering of light with particles whose sizes are much smaller than the

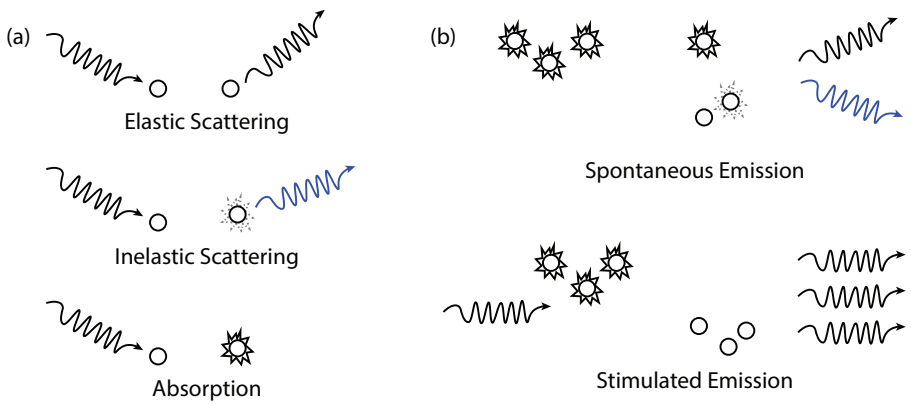

Figure 2.2: (a) Interaction of light with an atom/molecule where the photon can either be elastically scattered, inelastically scattered or absorbed by the atom/molecule, leaving the it unchanged, in a vibrationally/rotationally excited state or an electronically excited state. (b) Spontaneous and stimulated emission from electronically excited atoms/molecules. The color change of the light indicates a shift of the wavelength compared to the incoming light.

wavelength of the light is called Rayleigh scattering, while elastic scattering of electrons is called Thomson scattering. In an inelastic scattering process, on the contrary, scattered light will either gain or lose energy, resulting in a shift of the wavelength. For example, in Raman scattering, scattering with an increase of photon energy gained from the vibrational energy of the molecule is called an anti-Stokes Raman scattering, while Stokes Raman scattering indicates an energy loss in the scattered light. The third process presented in figure 2.2a is the excitation of an atom/molecule with the light being absorbed. Absorption of light usually takes place when the wavelength of the incident light matches a certain transition of the atom/molecule, leaving the atom/molecule in an excited state.

For excited atoms/molecules, they will eventually return to the ground state. Relaxation of an excited particle is usually accompanied by the emission of radiation. There are two types of emission: spontaneous emission and stimulated emission (see figure 2.2b). As defined by the name, spontaneous emission occurs spontaneously without any external disturbance. Spontaneous emission is more likely to take place when the atom/molecule has been electronically excited and the direction of the emitted photons is random. Relaxation from vibrational or rotational excited states are usually achieved by a radiationless process, such as collisional quenching. And if there exists more than one lower state to which the deexcitation is allowed, the wavelength of the emitted light will vary, leaving the atom/molecule in different states. For stimulated emission, however, an incident photon is required to stimulate the transition resulting in an emitted photon that is identical in wavelength, polarization and propagation direction to the incident photon. If the same stimulated emission is multiplied for many times, amplification of light will be achieved and a device based on this technique is called laser, i.e., light amplification by stimulated emission of radiation.

2.2.2 Emission Spectroscopy

Ideally, the signal intensity of spontaneous emission is the product of three parameters, the wavelength-dependent optical response of the spectrometer $R(\lambda)$, the Einstein coefficient for the spontaneous emission A, and the population of the excited state $n_{excited}$:

$$I_\lambda = R(\lambda) \times A \times n_{excited} \tag{2.14}$$

The optical response of a spectrometer can be calibrated with a standard light source, and the Einstein coefficient is usually given by theoretical calculations or

experimental values for commonly used atoms and molecules. The population of the excited state can therefore be determined by the emission spectrum.

The population of an excited state, or more precisely the population distribution of a certain excited state, is related to many parameters, such as the gas temperature, the pressure and the excitation/ionization degree of the plasma. The emission spectrum of a plasma discharge can be considered as the fingerprint of a given discharge and can be used as a technique to categorize it. For example, the emission spectrum measured from a gliding arc discharge with different flow rates of the gas shows the transition of the plasma from glow-type to spark-type with increasing gas flow rates [81]. Significant differences of the spectrum captured in a plasma actuator powered by two different plasma generators with similar input power was observed in [83], showing that the majority of the energy goes to the flow heating when powered by an RF plasma generator, whereas a significant amount of energy is wasted on electrodes and surrounding metal hardware when powered by a pulsed DC plasma generator.

Optical emission spectroscopy is most often used to determine energy distribution or temperature components of a plasma. The vibrational and rotational temperature of the most frequently observed plasma emissions can be calculated by fitting the spectra with a line-by-line radiation software named SPECAIR. For the determination of gas temperature of non-thermal plasma (reviewed in [84]), $N_2(C-B)$ and $OH(A-X)$ transitions at atmospheric pressure and $N_2^*(B-X)$ transition at lower pressures are mostly commonly used. The $N_2(C-B)$ transition between 280 nm and 550 nm is often the dominant emission for plasma running with N_2. Observation of $N_2(C-B)$ emission also provides evidence of the presence of N_2 in the plasma reactor as N_2 can hardly be created by any electronic dissociation process. As one of the most studied electronically excited states, $OH(A)$ can be easily produced by non-thermal plasmas with the presence of water vapor. Besides direct excitation from the ground state, $N_2(C)$ and $OH(A)$ could also be produced from, for example, excitation of metastable $N_2(A)$ state, or dissociation of other polyatomic molecules containing OH. It is thus necessary to validate if the translational-rotational equilibrium has been reached before assuming the gas temperature is equal to the rotational temperature. For example, at atmospheric pressure, translation-rotational equilibrium can be achieved by collisions between the excited molecules and the ambient gas before the relaxation of the excited atoms/molecules takes place.

2.2.3 Spectrum of diatomic molecules: N_2 and O_2

Molecular spectra can be very complicated compared to atomic spectra. Detailed discussion of either nitrogen or oxygen spectrum could be a book in itself. In the following paragraphs, fundamentals of diatomic molecular spectra will first be briefly introduced, followed by discussions of two spectra that are related to this thesis: the $C^3\Pi_u \leftarrow B^3\Pi_g$ transition of nitrogen and the $b^1\Sigma_g^+(v'=0) \leftarrow X^3\Sigma_g^-(v''=0)$ transition of oxygen.

The energy of a diatomic molecule can be simplified as

$$\varepsilon_{total} = \varepsilon_{electronic} + \varepsilon_{vibration} + \varepsilon_{rotation} \tag{2.15}$$

using the Born-Oppenheimer Approximation which assumes that the electronic, vibrational and rotational energies are independent of each other. The rotational energy levels of a rigid diatomic molecule can be given by

$$\varepsilon_{rotation} = BJ(J+1)\ cm^{-1} \tag{2.16}$$

where $J = 0, 1, 2 ...$ is the *rotational quantum number* and B is the *rotational constant*. The vibrational energy levels of a simple harmonic oscillator are given by

$$\varepsilon_{vibration} = (\nu + \frac{1}{2})\bar{\omega_{osc}}\ cm^{-1} \tag{2.17}$$

where $\nu = 0, 1, 2 ...$ is the *vibrational quantum number* and $\bar{\omega_{osc}}$ is called the *zero-point energy* with $\nu = 0$.

For an electronic transition of a diatomic molecule, all transitions with different vibrational quantum numbers are allowed, although with vastly varying strengths due to the Franck-Condon factor for transitions with different $\Delta\nu$. Each set of such transitions are called a *band* and conventionally denoted by their vibrational quantum numbers as $(\nu',\ \nu'')$ where the upper state comes first with a single prime. Examples of different bands of the $C^3\Pi_u \leftarrow B^3\Pi_g$ transition of nitrogen can be found in figure 2.4.

The transition energy of a certain band can be written as

$$\Delta\varepsilon_{total} = \bar{\nu}(\nu', \nu'') + B'J'(J'+1) - B''J''(J''+1) \tag{2.18}$$

where $\bar{\nu}(\nu', \nu'')$ is the rotational free energy difference of an electronic-vibrational transition and is also defined as the *band origin*. ν, B and J with a single prime represent the upper state. For different electronic transitions, different selection rules of J may apply. Transitions with the same ΔJ are referred as a branch: $\Delta J = -2, -1, 0, 1, 2$ as the O, P, Q, R and S branch respectively.

For the R and P branch where $\Delta J = \pm 1$, the transition energy can be written as

$$\Delta\varepsilon_{total} = \bar{\nu}(\nu', \nu'') + (B' + B'')m + (B' - B'')m^2 \tag{2.19}$$

where m = ± 1, ± 2, ... is $-(J' + 1)$ for the P branch and $(J'' + 1)$ for the R branch. An example of the transitions of P, Q, R branch with $B' < B''$ is shown in figure 2.3. In this situation, the P branch appears at the lower wavenumbers of the band origin while R branch on the higher wavenmuber side. As $B' - B''$ is negative, a maximum wavenumber will be reached for the R branch. The point where the maximum separation from the band origin is reached is called the *band head*. Note that for transitions with a higher B', the band head will appear in the P branch.

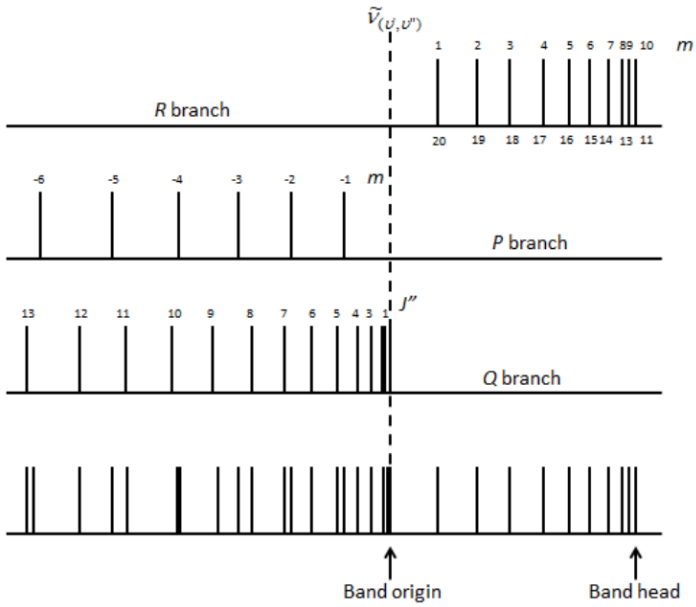

Figure 2.3: An example of the rotational fine structure of a vibration-electronic transition for a diatomic molecule where the rotational constant is smaller for the upper state, i.e., $B' < B''$. Note that the wavenumber instead of wavelength is used here. Figure reproduced from [85].

- **The $C^3\Pi_u \leftarrow B^3\Pi_g$ transition of nitrogen** The most important and frequently observed plasma emission, especially when running with air at atmospheric pressure, is the $C^3\Pi_u \leftarrow B^3\Pi_g$ transition of nitrogen. The capital Greek letter Π shows that the axial component of the total orbital angular momentum of the electrons for both states is 1; the number 3 means that the total electron spin momentum S equals 1, as $2S + 1 = 3$; small u/g indicates the symmetry of the state with g as *gerade* (even in German) and u as *ungerade* (odd in German); C and B are the notation

for the electronic energy levels. A typical emission spectrum of N_2, taken from a NPD-stimulated flame, is given in figure 2.4 where several bands with $\Delta\nu$ = -2 to 4 are captured. In the energy level diagram presented to the right of the spectrum, transition bands with same $\Delta\nu$ are marked with identical colors. The intensity ratio between different bands and rotational structures are dependent on the temperature. Temperature fitting of the spectrum and comparison between different spectra captured with different applied voltage of NPD will be discussed in section 4.4.2.

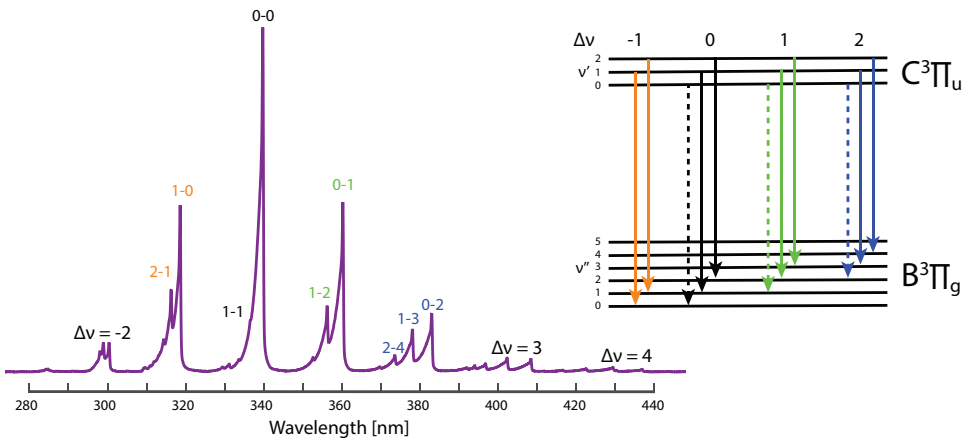

Figure 2.4: Emission spectrum of N_2 captured from a NPD-stimulated flame. The vibrational quantum numbers of each band are labeled above. Diagram of the vibrational energy level of $N_2(C^3\Pi_u \leftarrow B^3\Pi_g)$ with four bands where $\Delta\nu$ equal to -1, 0 , 1 and 2 respectively. Same color is used for transitions from same band.

- **Oxygen A band** $(b^1\Sigma_g^+(v'=0) \leftarrow X^3\Sigma_g^-(v''=0))$ Another interesting and important spectrum that has been observed in this thesis project is the oxygen A band. Emission lines from molecular O_2 can be observed when the combustion is lean, i.e., excess of O_2. As one task of plasma-assisted combustion is to push the lean blow-out limit of a flame to reduce NO_x emission, a flame that is running with PAC is usually very lean (below 0.5 as in the Siemens burner). Therefore, emission from molecular oxygen, which can hardly be observed due to fast quenching in rich flames, can be captured. The strongest emission of molecular oxygen in the visible range is the A-band $(b^1\Sigma_g^+(v'=0) \leftarrow X^3\Sigma_g^-(v''=0))$ around 760 nm. Unlike the $N_2(C-B)$ transition, the upper and lower states of oxygen A band both have a zero axial angular momentum component. For Σ states, a special superscript with + or - applies. It indicates that the wave function of the electron remains unchanged (designated by +) or changed in sign only (designated by -) upon a reflection in a plane containing the nuclei.

The Oxygen A band is a magnetic dipole transition with four branches: P (PP), R (RR), RQ and PQ. As previously noted, the R and P branches represent $\Delta J = +1$ and -1 respectively. A speciality of the oxygen A band is the Q branch with $\Delta J = 0$. It is split into two with different ΔN, where N is the quantum number of the angular momentum without spin. For the RQ branch, $\Delta N = +1$ and for the PQ branch, $\Delta N = -1$. An example of the measured spectrum of the A band and a diagram of the four kinds of transitions is presented in figure 2.5. The R and RQ (or P and PQ) transitions have similar strengths but slightly different energies (see figure 2.5b). The splitting of P and PQ is well-resolved in the spectrum as shown in figure 2.5 while it is hard to identify the R and RQ due the band head. The dashed circles in 2.5b represent the antisymmetric levels between which the transitions are not allowed due to the zero nuclear spin of O_2. More detailed information about the spectrum of oxygen A band could be found in the literature [86, 87, 88, 89].

An emission spectrum taken from measurements in a complex system, i.e., the large-scale industrial burner investigated in this work, is shown in figure 2.5a. In addition to the O_2 A-band spectrum, two atomic spectral lines from Potassium impurities (D-lines, 4p to 4s) are also observed. As the atomic emission from K* is much stronger than the molecular emission from O_2, a small amount of K contaminated on the electrode surface will produce considerable emission when excited by the discharge. More discussion about this measurement will be discussed in section 4.3.3.

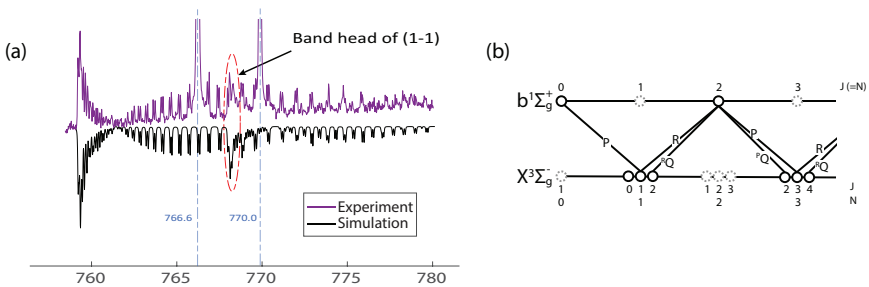

Figure 2.5: (a) Single-shot spectrum of the O_2 A band measured in the Siemens burner compared with simulation spectrum generated by PGOPHER [90]. (b) Diagram of the magnetic dipole transition of O_2 A band. Note that the transition between J = 0 to J = 0 is forbidden.

2.2.4 Laser-induced Fluorescence

Laser-induced fluorescence (LIF) is an optical diagnostics technique where the target species is excited with a laser and the fluorescence, i.e., the spontaneous emission from the excited species, is subsequently captured. As the wavelength of the laser can be tuned for a certain transition of a species, and the fluorescence signal is not restricted in a certain direction (usually isotropic), LIF has been widely used for two-dimensional imaging of selective species for various physical, chemical and medical applications.

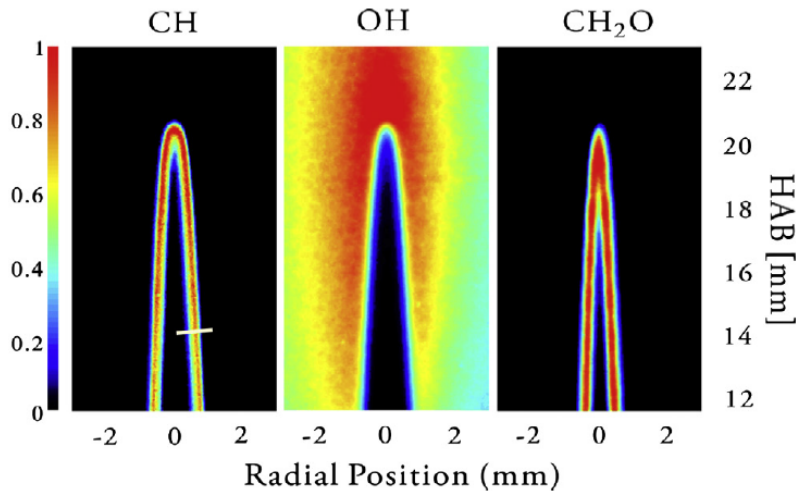

Figure 2.6: Quasi-simultaneous PLIF imaging of CH, OH and CH_2O of a premixed conicaol flame. HAB: height above the burner. Figure adapted from [91].

Two-dimensional laser-induced fluorescence, often referred to as planar laser-induced fluorescence (PLIF), of intermediate species such as the methylidyne radical (CH), hydroxyl radical (OH) and formaldehyde (CH_2O) is often carried out in combustion of hydrocarbons. For example, PLIF of CH and CH_2O is often used for instantaneous detection of the flame front. As shown in figure 2.6, two adjacent thin layers of CH (located upstream of the preheat zone) and CH_2O are revealed by PLIF, indicating the position of the flame front. In addition, heat release rate imaging of a flame can be acquired by the pixel-by-pixel multiplication of simultaneously captured PLIF signals of OH and CH_2O [92].

Important for both combustion diagnostics and plasma-related diagnostics, OH can be easily produced by a plasma when interacting with water vapour and is often used as a marker for the post-flame zone of a hydrocarbon/air flame (see figure 2.6). The energy level diagram for OH LIF is given in figure 2.7.

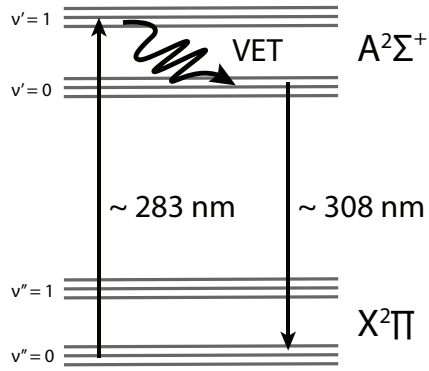

Figure 2.7: Energy level diagram of OH LIF where different levels of each vibrational state indicate rotational structure with different J.

For OH LIF used in this thesis, OH is excited through the $Q_1(8)$ transition of $X^2\Pi_(\nu'' = 0) \leftarrow A^2\Sigma^+(\nu' = 1)$ by UV laser light at 283.92 nm[1]. The dominating part of the fluorescence signal of OH LIF comes from the (0,0) band: $A^2\Sigma^+(\nu' = 0) \leftarrow X^2\Pi_(\nu'' = 0)$ where vibrational energy transfer (VET) of the excited state has been accomplished before the transition.

[1] $Q_1(8)$, also labeled as $Q_{11}(8)$, refers to the transition where $\Delta J = 0$, $J'' = 8$ and the axial angular momentum quantum number including nuclear spin F with $F' = F'' = 1$

Chapter 3

Coded Imaging

An important task of optical diagnostics is to extract useful information from captured data. This is particularly important for plasma-related diagnostics as the signal of interest is usually accompanied by luminous plasma emission. Different techniques established on coded imaging have been applied in this thesis to suppress the background interferences. This chapter will start from a short introduction of the principle of imaging coding and continue with detailed discussions of techniques that has been used in this thesis, e.g., Periodic Shadowing and Frequency Recognition Algorithm for Multiple Exposures (FRAME).

3.1 Fourier Transform and imaging coding

3.1.1 Fourier Transform

The core theory for the coded imaging used in this thesis is the Fourier transform of images. Mathematically, Fourier transform refers to the transfer of functions depending on space to functions depending on spatial frequency while inverse Fourier transform does it vice versa. The equations of 1D and 2D Fourier transform are given in Equation 3.1 and 3.2 respectively:

$$\begin{aligned} F(\nu) &= \int_{-\infty}^{\infty} f(x) e^{-2\pi i \nu x} dx \\ f(x) &= \int_{-\infty}^{\infty} F(\nu) e^{2\pi i \nu x} d\nu \end{aligned} \tag{3.1}$$

$$\begin{aligned} F(\nu, \upsilon) &= \int_{-\infty}^{\infty} \int_{-\infty}^{\infty} f(x, y) e^{-2\pi i (\nu x + \upsilon y)} dx dy \\ f(x, y) &= \int_{-\infty}^{\infty} \int_{-\infty}^{\infty} F(\upsilon, \nu) e^{2\pi i (\nu x + \upsilon y)} d\nu d\upsilon \end{aligned} \tag{3.2}$$

with functions depending on space represented by $f(x)$ ($f(x, y)$) and variable x and y while functions depending on spatial frequency represented by $F(\upsilon)$ ($F(\nu, \upsilon)$) with spatial (temporal) frequencies ν and υ.

Detailed analysis of Fourier Transform can be found in many text books. In the following paragraphs, some examples of 2D Fourier Transform, which are important for understanding techniques used in thesis, are discussed in detail.

3.1.2 Spatial and Fourier Domain of images

Three different examples of images with their spatial domain and the corresponding Fourier Domain, i.e., the absolute value of the real part of the Fourier components, are shown in figure 3.1. Instead of RGB images, monochrome images are used here as all results captured in this thesis, and with most of optical diagnostics techniques, are monochrome images.

The spatial domain of an image is just the conventional way of presenting an image as in figure 3.1a-c. The two images are selected as they represent two different features: the one with chili peppers as shown in figure 3.1a, has more details compared with the one with the word 'plasma' as shown in figure 3.1b. This difference is demonstrated in their Fourier domain as the Fourier Domain

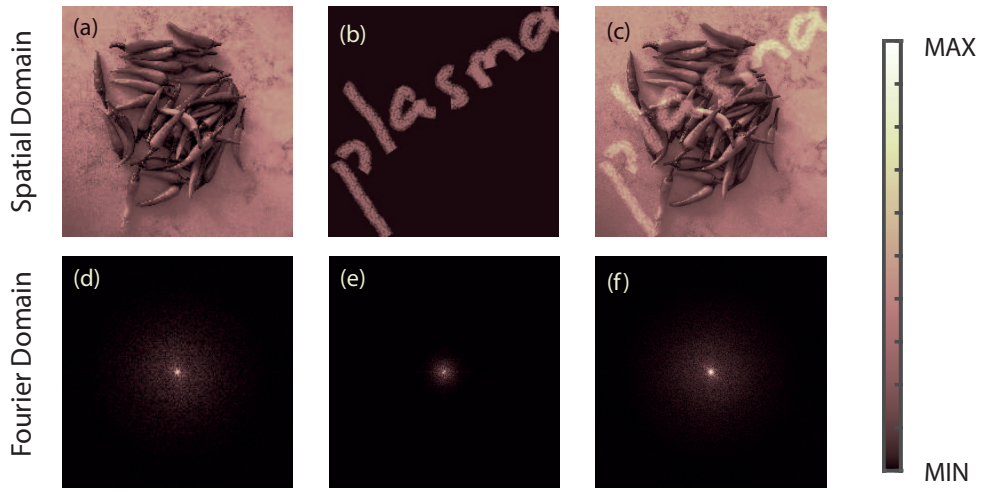

Figure 3.1: An example of the spatial domain and Fourier domain of images with different spatial structures and their combination.

of the chili peppers includes more higher frequency components as shown in figure 3.1d while the Fourier components of the plasma characters, as shown in figure 3.1e, are concentrated in the center, i.e., lower frequency.

The combination of the images of the chili pepper and word 'plasma' in both spatial domain and Fourier domain are shown in figure 3.1c and f. As they are mixed in both domains, it is nearly impossible to distinguish them without knowing one of them in advance. This is often a problem for optical diagnostics when the background interference from unwanted signals, e.g., the plasma emission, are strong and unpredictable.

3.1.3 Spatial and Fourier Domain of coded images

When discussing the concepts of spatial and Fourier Domain of an image, it is intuitive to start with the spatial domain and derive the functions in Fourier Domain. However, for the techniques used in this thesis, it is easier to think the other way around: if one would like to distinguish two signals in their Fourier domain as it is impossible to distinguish them in the spatial domain, what the Fourier domain should look like? And what is the corresponding spatial domain? It is then instinctive to start with a $F(\nu, \upsilon)$ with a fixed ν and υ, i.e., a delta point in the 2D Fourier Domain as the black dot shown in figure 3.2a.

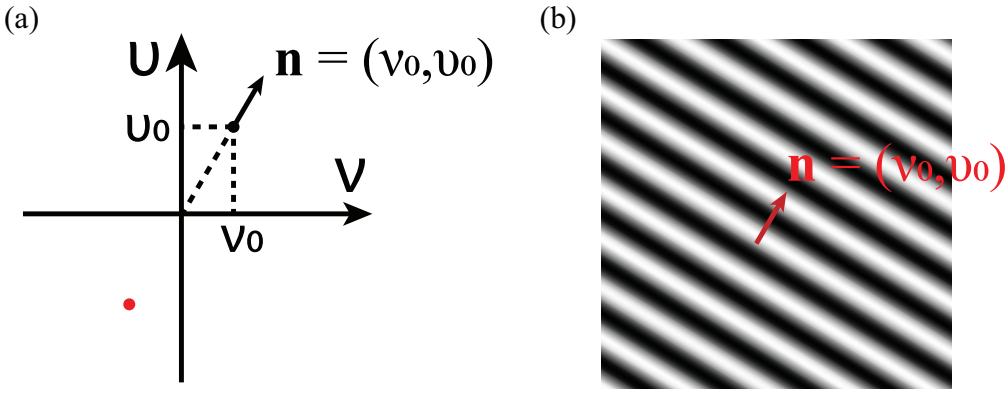

Figure 3.2: Function of a fixed ν and υ in the Fourier domain (a) and its real part as a function of x, y in the spatial domain.

Using Eq.3.2, for a fixed $\nu = \nu_0$ and $\upsilon = \upsilon_0$, the inverse Fourier transform is:

$$f(x, y) = e^{2\pi i(\nu_0 x + \upsilon_0 y)} \tag{3.3}$$

Applying the Euler's formula, $e^{ix} = cosx + isinx$, Eq.3.3 can be writen as:

$$f(x, y) = cos[2\pi(\nu_0 x + \upsilon_0 y)] + isin[2\pi(\nu_0 x + \upsilon_0 y)] \tag{3.4}$$

The real part of the Eq.3.4, i.e., the intensity of the imaging in spatial domain, $cos[2\pi(\nu_0 x + \upsilon_0 y)]$, is plotted in figure 3.2b as a function of x and y. It is a sinusoid pattern with the direction or normal $\mathbf{n} = (\nu_0, \upsilon_0)$ and frequency equal to $\sqrt{\nu_0^2 + \upsilon_0^2}$. If this sinusoid pattern could be introduced or coded in certain signal, the modulated signal will be separated from the unmodulated ones in the Fourier domain. Since cosine is an even function, the Fourier domain of a signal with sinusoid pattern will have another component with $\nu = -\nu_0$ and $\upsilon = -\upsilon_0$, as the red dot shown in figure 3.2a.

Two different sinusoid modulations are applied on images of the chili pepper and world 'plasma' in the spatial domain by multiplying the raw data with the corresponding sinusoid pattern (see figure 3.3a-b). In the Fourier domain as shown in figure 3.3d-e, two additional clusters show up as predicted. The central part, which represents the DC components, remains as for real images the intensity is always positive. Since the sinusoid pattern is multiplied on the chili pepper horizontally, the two frequency components in the Fourier domain also appear on the horizontal axis. In the meanwhile, the extra two clusters for the word 'plasma' appear on the vertical axis in the Fourier domain as the sinusoid pattern is applied vertically in the spatial domain.

The sinusoid modulation on the chili pepper has higher frequency than the one applied on the word 'plasma'. Hence, the two frequency components in

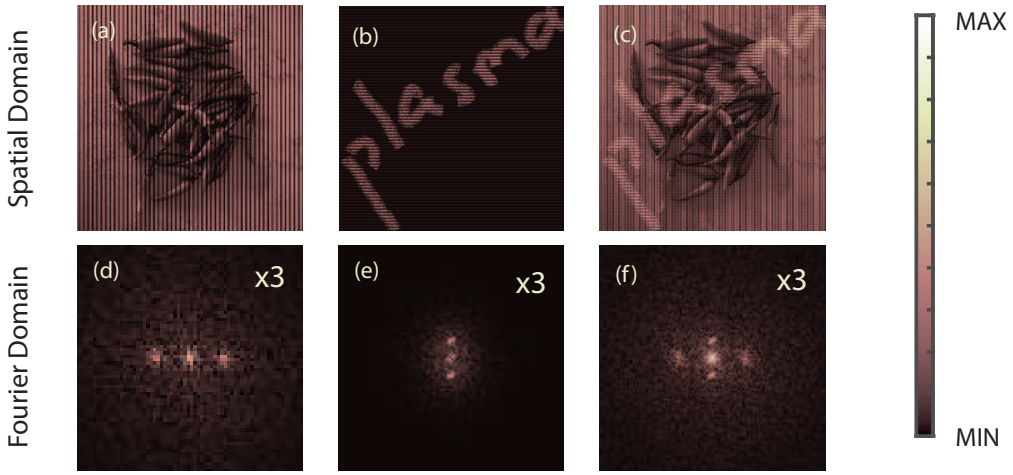

Figure 3.3: Examples of the spatial domain and Fourier domain of images encoded with different sinusoid modulations and their combination. The Fourier domain is shown with three times magnifications for a clearer view in the center.

the Fourier domain of the chili pepper are further away from the center part. This means that it is easier to separate the modulated components from the unmodulated components in the center if the modulation applied on the spatial domain has a higher frequency. Therefore, in real-life measurements, modulation should be implemented using the highest modulation frequency possible.

Signals with different modulations are added up together and are shown in figure 3.3c and f. While it is still nearly impossible to separate them in the spatial domain, it is possible to extract the information of the modulated signal in Fourier domain as signals with different modulations are well-separated. Extracting the modulated signal will be done by a lock-in algorithm which will be discussed later in Section 3.2. For the techniques that have been used in this thesis, encoding the target signal with sinusoid patterns are done in two ways: periodic shadowing (PS) or structured illumination.

3.1.4 Periodic shadowing

For periodic shadowing, a sinusoid pattern is introduced to the signal of interest right before the detection system. As the additional interference that is introduced in the detection system has no such structure, it is therefore possible to extract the native signal from the interference noise of the detection system. Periodic shadowing was first developed to solve the problem with stray light in spectroscopy [93] where a Ronchi grating was added on the entrance slit of

a spectrometer as shown in figure 3.4. Later on, a custom-made optical fiber bundle [94] was developed as an alternative to the Ronchi grating. As shown in figure 3.4, the input of the fibers is concentrated in a round shape with each individual fibers having a homogeneous collecting efficiency. And the output of the fibers is prearranged in a linear periodic form so that the periodic shadowing pattern could be achieved without any blockage of light compared with the usage of the Ronchi gratings.

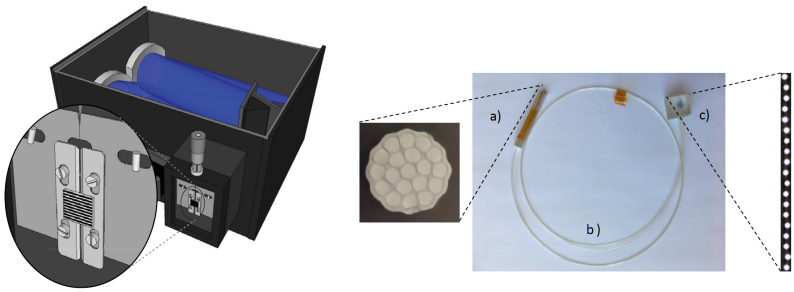

Figure 3.4: (Left) Schematic view of the Ronchi grid target on the entrance slit of a spectrometer. Figure adapted from [93]. (Right) Optical fiber bundle for periodic shadowing with (a) the input end, (b) the fiber and (c) the output end. Figure adapted from [93, 94].

The usage of the optical fiber bundle simplifies the alignment substantially, i.e., there is no need to image the target onto the entrance slit of the spectrometer. This is particular helpful for *in situ* measurements where experimental environments can be chaotic and optical access is most often very limited, for example in a high-pressure/vacuum chamber. However, since the light needs to be able to propagate in the fiber, the wavelength of signal is limited by the material of the fiber.

In paper I, periodic shadowing is applied in streak camera measurements for the first time. The space-charge induced temporal dispersion is minimized with the help of periodic shadowing while both temporal coverage and spatial information are maintained. More details about this project will be discussed in Section 4.2.

3.1.5 Structured illumination

Another way to code the sinusoid pattern into a signal is done by structured illumination for laser-related techniques. In the literature, it is called Structured Laser Illumination Planar Imaging (SLIPI). Instead of a laser sheet with homogeneous intensity in the probe volume, an additional sinusoid pattern is applied perpendicular to the propagation direction of the laser. Hence, only the laser-induced signal will be modulated. Structured illumination is particu-

larly useful for laser-related techniques when the background interference, e.g., plasma emission, is strong and rapidly varying.

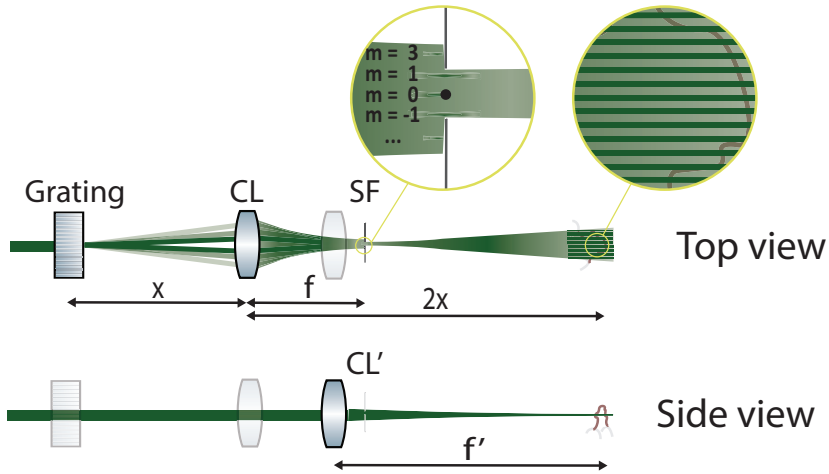

Figure 3.5: Optical arrangement for the creation of a modulated laser sheet. CL- vertically oriented cylindrical lens, SF- spatial filter, CL'- horizontally oriented cylindrical lens. Figure adapted from Paper II.

The easiest way to achieve a modulated laser sheet at the probe volume is to image a grating on the target. This will, however, generate residual lines from the higher harmonics of the grating, i.e., the modulation is not perfectly 'clean'. To get a clean pattern, a spatial filter is placed at the Fourier plane of the lens. The spatial filter will remove all the overtones and the 0th order in the center but the two fundamental frequencies of the grating. A sketch of this optical arrangement is given in figure 3.5. With this configuration, the modulated pattern will be the interference pattern of the two fundamental frequency components, which is a prefect sinusoid. Unlike the image of a grating which has a fixed location for certain image system, the interference pattern of the two frequency components covers a larger area as it exists wherever the two frequency components meet.

A drawback of applying a spatial filter is the loss of intensity. Customized diffractive optical elements (DOE) which preserve the energy mostly in the first orders is introduced to replace the grating to solve this problem. The DOE that has been used in this thesis (paper II and paper V) is manufactured by *HOLOOR* with $\approx 87\%$ energy stored in first orders. Although the energy left in the 0th order is less than 1% with this DOE, it is still critical to remove it with a spatial filter in the center. An example of how the sinusoid pattern will be like with a tiny existence of the 0th order is shown in figure 3.6: The amplitude of every other period will be weaker than expected.

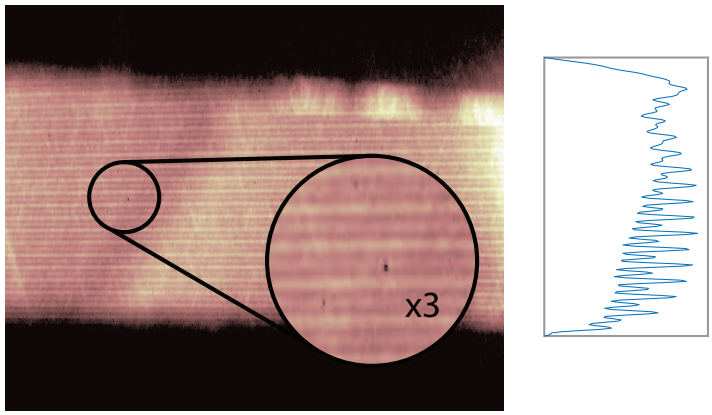

Figure 3.6: An example of the Rayleigh scattering signal with structured illumination. The periodic strips with one stronger and one weaker indicate the existence of the 0th order from the grating pattern of the DOE.

3.2 Lock-in analysis

A lock-in algorithm inspired by the lock-in amplifier [95] is used to extract information of the modulated signal. The lock-in amplifier refers to the electrical instrument that extracts signal information (both amplitudes and phases) from extremely noisy environment. A presumption for the lock-in amplifier to work is the knowledge of the modulation frequency of the target signal, i.e., the time-dependence of the signal. For images superimposed with certain sinusoid pattern using periodic shadowing or structured illumination, the details of the modulation frequency is known and can also be found in the Fourier domain. It is therefore possible to extract the modulated signal with a lock-in algorithm.

3.2.1 Mathematical description in spatial domain

Detailed description of the lock-in algorithm has been discussed in [93] when periodic shadowing was introduced and used in applications of spectroscopy for the first time. There the signal is analyzed independently for different wavelengths, i.e., in one dimension. In the following paragraphs, the mathematical description of the lock-in algorithm will be given in two dimensions which is necessary for analysis of an image.

An acquired image include both modulated signal and unmodulated signal can be represented as:

$$f(x,y) = A(x,y)sin[2\pi(\nu_0 x + \upsilon_0 y) + \phi_0] + B(x,y) \tag{3.5}$$

where $A(x,y)$ is the native signal to be modulated, i.e., the signal of interest, and $B(x,y)$ is the interference signal, i.e., the unmodulated signal. Similar to Eq.3.4, the sinusoid modulation applied on the signal of interest has the frequency $\sqrt{\nu_0^2+\upsilon_0^2}$, the direction $\mathbf{n}=(\nu_0,\upsilon_0)$ and the phase ϕ_0 at the origin of the Cartesian coordinate system with axis x and y.

To apply the lock-in algorithm, two reference signals with a $\pi/2$ relative phase shift and same frequency and orientation as the modulation pattern are introduced:

$$\begin{aligned} R_1(x,y) &= sin[2\pi(\nu_0 x+\upsilon_0 y)+\phi_{ref}] \\ R_2(x,y) &= sin[2\pi(\nu_0 x+\upsilon_0 y)+\phi_{ref}+\pi/2] \end{aligned} \tag{3.6}$$

Multiplying $f(x,y)$ with $R_1(x,y)$ and $R_2(x,y)$ and replace $\nu_0 x+\upsilon_0 y$ with a denotation X leads to:

$$\begin{aligned} &f(x,y)R_1(x,y) = A(x,y)sin(2\pi X+\phi_0)sin(2\pi X+\phi_{ref}) + B(x,y)sin(2\pi X+\phi_{ref}) \\ &f(x,y)R_2(x,y) = A(x,y)sin(2\pi X+\phi_0)sin(2\pi X+\phi_{ref}+\pi/2) \\ &+ B(x,y)sin(2\pi X+\phi_{ref}+\pi/2) \end{aligned} \tag{3.7}$$

Using the trigonometric function $sin\alpha sin\beta=\frac{1}{2}[cos(\alpha-\beta)-cos(\alpha+\beta)]$, Eq.3.7 can be written as:

$$\begin{aligned} &f(x,y)R_1(x,y) = \frac{1}{2}A(x,y)[cos(\phi_0-\phi_{ref})-cos(4\pi X+\phi_0+\phi_{ref})] \\ &+ B(x,y)sin(2\pi X+\phi_{ref}) \\ &f(x,y)R_2(x,y) = \frac{1}{2}A(x,y)[sin(\phi_0-\phi_{ref})-sin(4\pi X+\phi_0+\phi_{ref})] \\ &+ B(x,y)sin(2\pi X+\phi_{ref}+\pi/2) \end{aligned} \tag{3.8}$$

To select the signal of interest, $A(x,y)$, a low-pass filter cutting out all the components except for the first term on the right hand side of Eq.3.8 will be applied, resulting as:

$$\begin{aligned} f(x,y)R_1(x,y) &= \frac{1}{2}\widetilde{A}(x,y)cos(\phi_0-\phi_{ref}) \\ f(x,y)R_2(x,y) &= \frac{1}{2}\widetilde{A}(x,y)sin(\phi_0-\phi_{ref}) \end{aligned} \tag{3.9}$$

where the tilde assignment on $A(x,y)$ indicates the frequency filtering. The signal of interest can then be calculated as:

$$\widetilde{A}(x,y) = 2\sqrt{[f(x,y)R_1(x,y)]^2+[f(x,y)R_2(x,y)]^2} \tag{3.10}$$

3.2.2 An example

An example of how the lock-in algorithm is used is given in figure 3.7. To apply the low-pass filter on the images, the images are first converted to Fourier domain by applying the fast Fourier transform (FFT). The sketch of the Fourier domain is shown in figure 3.7b (left) with the DC component $B(x, y)$ in the center and two modulated components corresponding to $A(x, y)sin[2\pi(\nu_0 x + \upsilon_0 y) + \phi_0]$ aside, similar as the example given in figure 3.2. To move the modulated components in center, the Fourier domain was multiplied with two reference signals with a relative $\pi/2$ phase shift. Once the modulated components have been moved to the center, low-pass filters can be applied as shown in figure 3.7b (right). And finally the extracted signal is achieved by an inverse Fourier transform (iFFT).

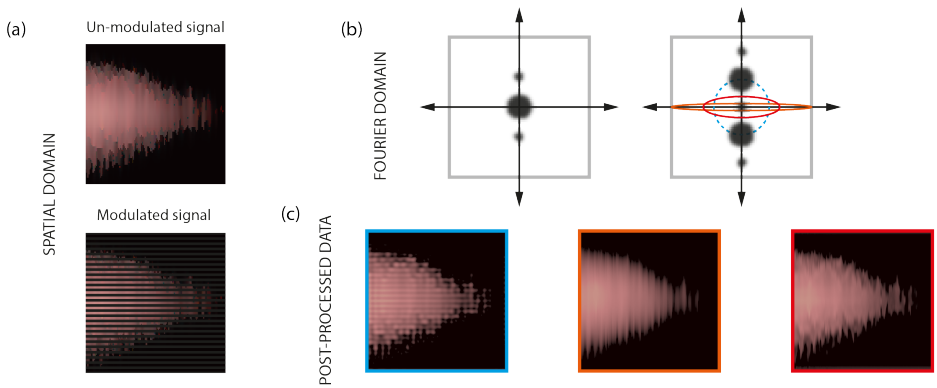

Figure 3.7: (a) The signal of interest with (bottom) and without (top) modulation. (b) Left: Fourier domain of the modulated signal. Right: Low-pass filters applied on the Fourier domain with the modulated component shifted to center. The post-processed data is shown in (c) with the same frame color as the filters applied with as indicated in (b). Figure adapted from Paper I.

The size and shape of the filter chosen is very important as it may make substantial difference in the final results. The post-processed data with three different filters is given in figure 3.7c. If some parts of the DC component is included by the filter, e.g., the blue on in figure 3.7, the modulation pattern will remain in the extracted signal, as shown in figure 3.7c with a blue frame. In general, the larger the filter is, the less spatial resolution is sacrificed. However, depending on the signal properties, including too many high frequency components where the signal to noise ratio is very low may add addition noise. Parameter study of the filter size of a real-life measurement will be discussed in next section as given in Fig.3.11.

3.3 Frequency Recognition Algorithm for Multiple Exposures

3.3.1 Principle of FRAME

Frequency Recognition Algorithm for Multiple Exposures (FRAME) was first proposed by Kristensson et al [96] to capture instantaneous 3D imaging of key species in a flame. Instead of a single modulation, FRAME encodes signals with multiple modulations which will later be deciphered by an algorithm. The modulation can be coded within the signal of interest (such as structured illumination) and/or right before the detection system (such as periodic shadowing). For example, if the signals with different modulations contains information at different times, it will be a videography technique with ultrafast temporal resolution as demonstrated in [97, 98]. If the modulations are coded at different locations, volumetric information could be reconstructed as presented in paper II. If the modulations are coded before the detection system, interference signals induced in the detection system can be reduced as presented in paper I.

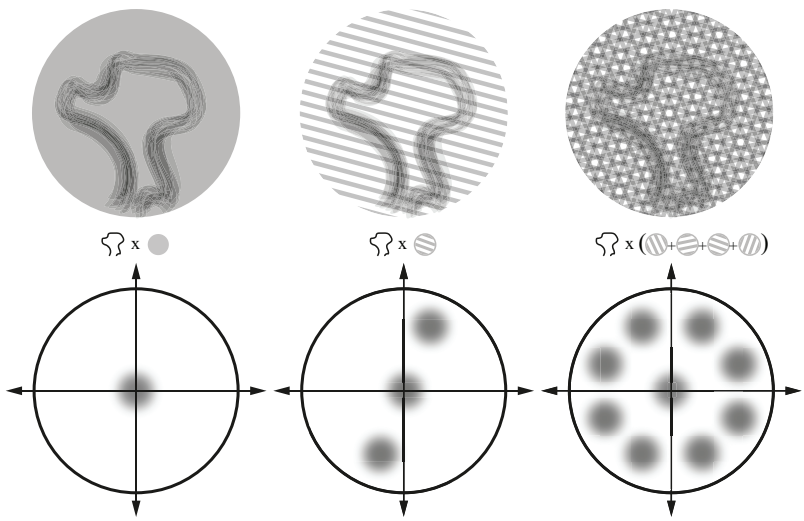

Figure 3.8: The spatial domain and Fourier domain of a target with homogeneous illumination (left), single modulated illumination (middle) and illumination with multiple modulations (right).

An example of the principle of FRAME is given in figure 3.8. Four different modulations is applied with same frequency but different directions. As the modulated components end up in different positions in the Fourier domain, it is therefore possible to extract them one by one using the lock-in algorithm discussed in previous sections.

The FRAME technique has been developed by the group led by Kristensson & Ehn since first published in 2017. Effect has been put to (1) apply FRAME on different applications and (2) increase the image storage capacity. With the initial number of modulation encoded to be four, it has been push up to 24 in [99] by combining both structured illumination and structured detection. Single-exposure videography using FRAME has been tested on pulse trains with sequence lengths ranging from 2 to 1024 image frames in [100]. More technique details regarding FRAME can be found in the thesis of Dr.Dorozynska [101] and the references therein.

3.3.2 FRAME for volumetric study

FRAME has been applied for 3D reconstruction of the ground state OH distribution around a gliding arc discharge in paper II. In this application, modulation was encoded to the signal by structured illumination. Instead of homogeneous illumination as used in conventional PLIF imaging, laser sheets with periodic intensity pattern were used. Four of these laser sheets were illuminating the target on top of each other with a gap of 0.5 mm. As illustrated in Fig.3.9, with the camera view perpendicular to the plane of the laser sheets, PLIF signal of OH from four different locations with different modulations will be recorded simultaneously in a single acquisition. Each individual PLIF image will later be extracted using a lock-in algorithm and the volumetric information of OH will be given by a 3D reconstruction based on a linear transition of the signal intensity between two neighboring layers of the PLIF images.

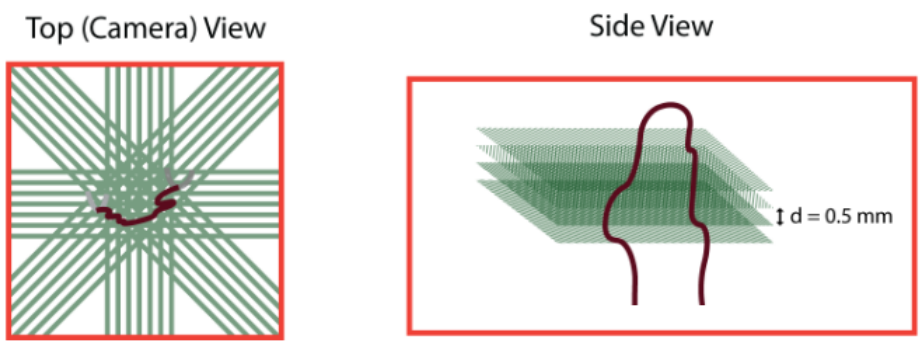

Figure 3.9: Laser sheets arrangement for volumetric study using FRAME. Figure adapted from Paper II.

An example of volumetric measurements of OH with FRAME is given in figure 3.10. The three enlarged sections in figure 3.10a represent three typical

situations: (I) only one modulation is captured, (II) no modulation is captured and (III) more than one modulation is captured. As predicted by the theory, wherever the modulation is captured in the raw data, the signal will remain in the extracted data. For example, in the center part of section I, only the horizontal modulation is captured. Therefore only the PLIF image with horizontal modulation has signal there. The same applies to section III where only the two PLIF images with the modulation captured in the raw data keep the signal at that region. Comparing section II and section III, it is noticeable that while the intensity of signal for those two sections has similar magnitude in the raw data, the signal of section III has much higher intensity in the extracted PLIF images. This is a great example of how the plasma emission background without any modulation is rejected with FRAME.

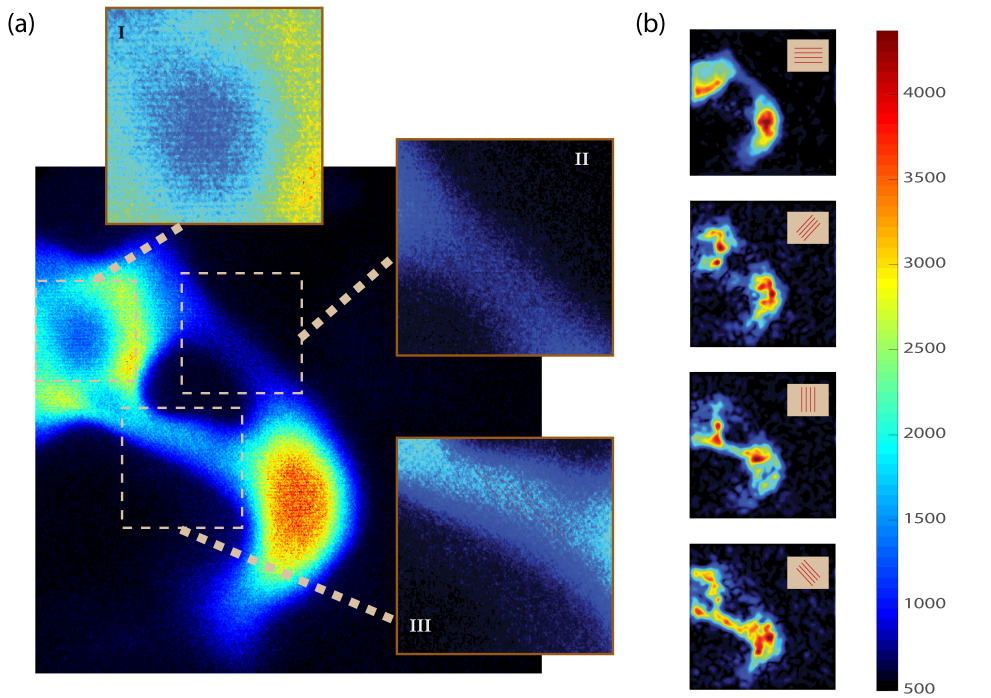

Figure 3.10: An example of the PLIF imaging with FRAME for OH around a gliding arc discharge. (a) Raw data with three zoomed sections for a clearer view of the modulation pattern. (b) Four extracted PLIF images presented with the corresponding modulation pattern on top.

As discussed in Section 3.2.2, the choice of the filter size is very important when extracting modulated signals. An example of how the size of the filter can affect the exacted data is given in figure 3.11 from the volumetric measurement of OH. Extracted PLIF images and the final 3D reconstruction with four different

filter sizes is demonstrated. In general, the larger the filter size is, the more details will be kept. However, if the filter is too big, interference from the neighbouring modulation will start to appear. For example, while the second and third PLIF images look very different with small filter as shown in figure 3.11e, they are almost identical in figure 3.11h where a large filter is applied. It is very important for the user of FRAME to choose a filter size that maximizes the signal-to-noise ratio without introducing any adjacent modulations. For this measurement, the filter for results shown in figure.3.11f is a good choice. As the size of this filter is less than 1% of the whole Fourier Domain, it shows a great potential of the image storage capacity of FRAME.

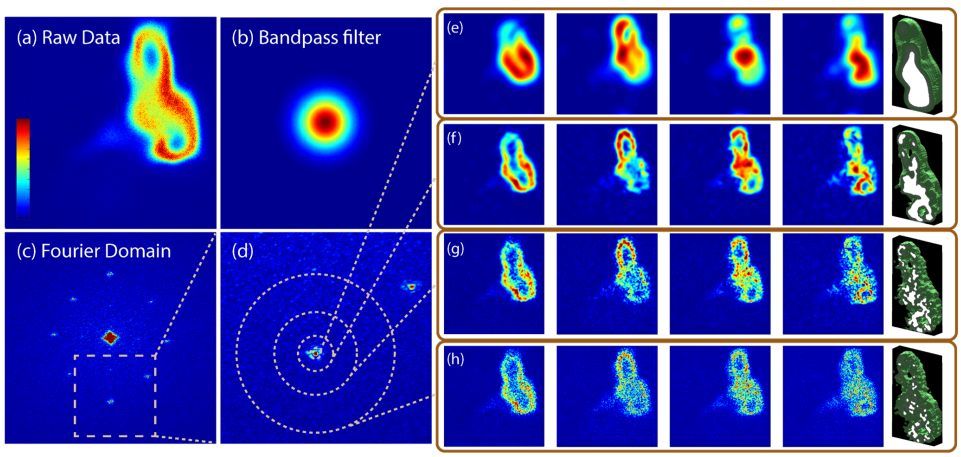

Figure 3.11: (a) Raw data captured by camera. A 2D Gaussian band-pass Filter (b) is used to select the isolated peaks of each layer in the Fourier domain (c). The size of the filter determines the resolution of the extracted images: the larger the filter size is, the more information is preserved (higher resolution) while the more interference from neighboring modulations will be included as well. (d-h)

Chapter 4

Experimental set-up and results

This chapter presents the experimental set-ups that has been used in this thesis, i.e., the streakcamera system (Paper I), the gliding arc set-up (Paper II, III & IV) and the nanosecond pulsed discharge system (paper V & VI). Results, not only the published ones, but also the detailed ones that have not been, neither will be, published, are discussed in detail. Some techniques that have been discussed in chapter 3 have been applied: Periodic shadowing was applied in the application with streak camera to reduce the temporal contrast of streak camera measurements (paper I); LIF with structured illumination was used to render 3D OH distribution around a gliding arc discharge channel together with FRAME (paper II); emission spectroscopy, LIF was carried out to characterize the flame for a large-scale industrial burner assisted by a rotating gliding arc system (paper III & V); and finally laser scattering with structured illumination, emission spectroscopy and LIF were used to study a lifted flat flame assisted by an ultrafast ns pulsed discharge (paper V & VI).

4.1 The streak camera

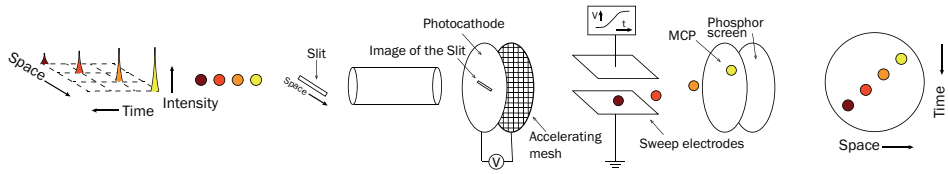

Figure 4.1: The principle of a streak camera.

The streak camera, first introduced by Courtney-Pratt in 1949 [102, 103] for the dynamic studies of fast transient phenomena, have the ability to simultaneously capture spatial and temporal information of a signal with subpicosecond resolution. The resolution of a state-of-the-art streak cameras is down to 800 fs (*HAMAMATRSU* with M16197-800 resolution option), which is far beyond the capability of traditional mechano-optical cameras. The working principle of streak cameras is presented in Fig.4.1. The signal of interest first passes a slit which is imaged on the photocathode (normally with certain de-magnification ratio: 1/2 as in paper I). The electrons generated by the photocathode will then be directed into a sweeping tube where a voltage ramp is applied. Electrons enter the sweeping tube at different times and therefore will experience different electric field that accelerate them to different perpendicular velocities. Eventually, the electrons with different velocities will arrive at the phosphor screen at different positions. Both the temporal and the spatial information along the slit axis will be visible on the final image, which is displayed to the right in figure 4.1.

4.1.1 Improved temporal contrast with periodic shadowing

The space charge effect [104] refers to the phenomenon that charged particles are repelled by other charged particles in space. For example, the velocity of electrons may be altered by repelling forces introduced by neighboring electrons. As a result, the velocity of the free electrons entering the sweep tube will be redistributed after being emitted from the photocathode. As any initial velocity difference of the electron when entering the sweeping tube will result in a temporal dispersion in the final image, the resolution in streak camera measurements is largely dependent on the space-charge-induced temporal dispersion. Much research has been carried out and proven successful in reducing this ef-

fect, for example, the accelerating mesh as shown in figure 4.1 can filter out the electrons which have non-zero velocity components in directions other than the propagation direction. More examples are given in paper I and the references therein.

In this thesis, periodic shadowing is applied to improve the temporal dispersion in streak camera measurements by tagging the signal with a sinusoidal pattern when entering the slit. The sinusoidal pattern was introduced in two ways: either by a Ronchi grating [93] or by a specially designed optical fiber bundle [94]. The experimental set-up, analysis process and results of the measurement of two consecutive scattered laser pulsed with FWHM around 250 ps are shown in figure 4.2. A clear drop of the signal intensity between the two pulses can be identified, indicating that the two peaks that were merged together were successfully separated by periodic shadowing. More results, including measurement of a single scattered laser pulse and measurement of the fluorescence lifetime of Rhodamine 610, were carried out and discussed in paper I. All results show that the improvement of temporal dispersion using periodic shadowing is most efficient at the rising/falling edge of a signal, i.e., when the change of signal intensity is dramatic. This is not surprising as the stronger the signal intensity is, the more deviated electrons there will be. And for the part where the signal is weaker, a little "leaked signal" from the stronger signal will make a huge difference.

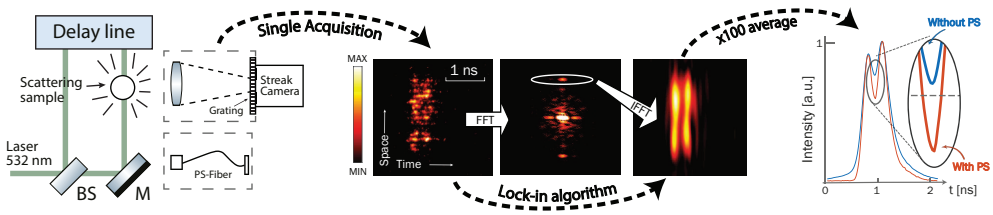

Figure 4.2: The principle of applying periodic shadowing for streak camera measurements including (left) a sketch of the set-up; (middle) an example of the analysis process of a single-shot imaging of two consecutive scattered laser pulses; and (right) the comparison of the temporal resolution acquired with/without periodic shadowing (PS). (Figure adapted from paper I.)

The difference of the modulation depth of the signal created by the grating and optical fiber bundle is demonstrated in figure 4.3a. Clearly, the fiber is better. As given in figure 3.4, the sinusoidal pattern of the signal is generated by a linear alignment of the fibers. In principle, no background interference will be introduced between two adjacent fibers. Whereas when the grating is used, background scattered light is able to enter the slit more easily due its higher acceptance angle and less efficient shielding. The temporal dispersion improvement for two consecutive signals is given in figure 4.3b where it is rated

by a parameter named the Michelson Contrast (see supplement material of paper I). The use of the optical fiber bundle not only provides higher modulation depth and better temporal contrast, the flexibility of the optical path via the fibers also allows for measurements to be carried out in complicated systems where optical access is limited. However, as different materials are required for light with different wavelength inside a fiber, broadband measurement for a single event using fibers might be difficult to achieve.

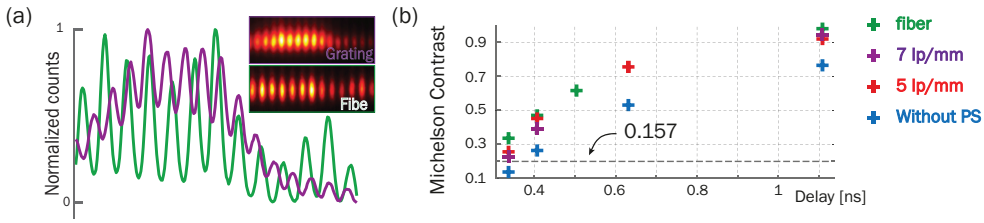

Figure 4.3: (a) The modulation depth of the signal created by the grating and fiber bundle. (b) Michelson contrast of the raw data (blue), grating of 5 lp/mm (red) and 7 lp/mm (purple) and fiber bundle of 4.8 lp/mm. The delay refers to the time difference between the two pulses. (Figure adapted from paper I.)

4.1.2 Improved effective dynamic range with periodic shadowing

The dynamic range of a streak camera is also limited by the space charge effect. To achieve higher dynamic range, optical beam deflection is proposed to replace the conventional electron beam deflection as shown in figure 4.1. For example, a streak camera with dynamic range over 3000 has been achieved using a solid-state waveguide as an alternative to the photocathode and sweeping tube [105]. Instead of a voltage ramp, the varying time of flight of the signal photons through the waveguide-based prism generates a linear mapping of time to space. The disadvantage of streak cameras based on optical beam deflection is the slow sweep rate [105], limiting the ultimate resolution of such a kind of streak camera.

Preliminary tests with the aim of increasing the dynamic range of a streak camera with periodic shadowing have been carried out. The results are shown in figure 4.4 where a femtosecond pulse train (FWHM around 50 fs) with a linearly decreasing intensity (50% less each pulse) was sent into a streak camera. Although the first pulse is twice as strong as the second one, the recorded intensity of the two differ much less. This is believed to be the result of photocathode saturation within the ultrashort pulse duration. The peak intensity of each pulse obtained with/without periodic shadowing is given in figure 4.4b. The range where the linearity of the peak intensity remains is wider for results obtained

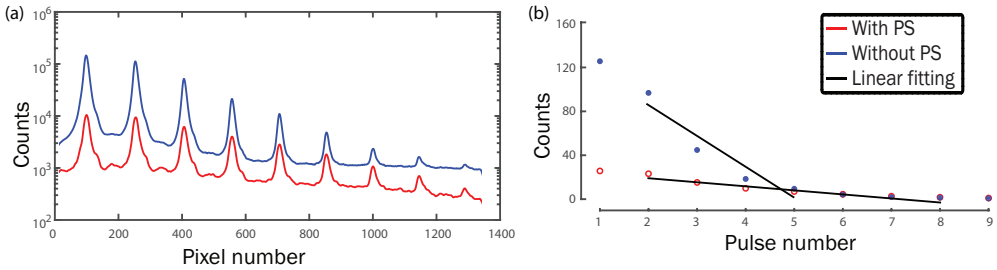

Figure 4.4: Measurement of a pulse train with a linear decrease in intensity. Single shot signal is given in red (with periodic shadowing (PS)) and in blue (without periodic shadowing) respectively in (a). The peak intensity of each pulse, normalized by the weakest peak, is given in (b).

with periodic shadowing: linear fitting with a R value equal around 0.90 can be attained from pulse 2 to pulse 8 with periodic shadowing but only from pulse 2 to pulse 5 without it. While further investigations are needed, this preliminary test showed the potential of achieving a higher effective dynamic range of streak camera by using periodic shadowing.

4.2 Volumetric study of hydroxyl radicals around a gliding arc discharge

As one of the representative radicals generated by gliding arc discharge due to electron-induced dissociation of water in ambient air [106, 107], ground-state OH has been measured to be distributed around the discharge column with a hollow structure and can thus be treated as a marker for the discharge channel [81, 108]. Ground-state OH is also important for plasma chemistry for its high oxidation potential (especially for the applications regarding pollutant gases decomposition) [109, 110]. For example, simultaneous PLIF of both toluene and OH showed that OH radicals induced by a GAD can effectively decompose toluene molecules [63].

When applying laser-induced techniques for plasma-related diagnostics, the interference of the luminous broadband plasma emission is always a problem (typical images of plasma emission are shown in Figure.1.3). For this project, where the task is to capture volumetric information of OH distribution in the vicinity of a gliding arc at atmospheric conditions, it is very important to be able to distinguish the LIF signal from the plasma emission. Therefore, structured illumination with FRAME is applied as the unmodulated plasma emission is inherently minimized by the FRAME approach.

An example of how OH distribution around a gliding arc can be misinterpreted due to the "3D-effect" is shown in Figure.4.5. With a fixed x-axis, the spread of 3D-effect-free OH distribution along the y axis is only half compared to traditional PLIF data. Therefore, volumetric, i.e., three dimensional, information

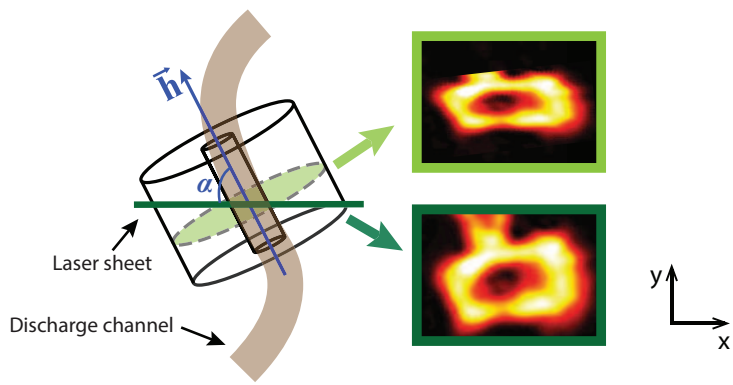

Figure 4.5: PLIF imaging of OH distribution around a gliding arc discharge channel with (bottom) and without (top) any 3D-effect. Severe distortions of the OH distribution can be seen from the one with 3D-effect.

of radical distributions is of utmost importance since plasma discharges have complex three-dimensional structures that display transient and unpredictable dynamics. Single-shot three-dimensional imaging of OH around a gliding arc discharge channel has been achieved in paper II using structured illumination and FRAME.

4.2.1 The gliding arc system

A schematic and a photo of the set up of the gliding arc discharge system are shown in Fig.4.6. The gliding arc discharge is driven by an AC power supply (Generator 9030E, 170 SOFTAL Electronic GmbH, Germany) at a frequency of 35 kHz, i.e. 28.6 ms per pulse. The voltage and the current can be measured with a high voltage probe (Tektronix 6015A) and a current monitor (Pearson Electronics, model 6585). The electrical power is calculated as the product of the measured voltage and current. For this project, the input power was limited to around 400 W. Two diverging electrodes were constructed with stainless steel tubes with an outer diameter of 3 mm. In order to avoid overheating, the tube is water cooled. The gas flow is injected from a hole with a diameter of 3 mm between the electrodes in order to drive the plasma column up along the electrodes. In this work, the gas flow rate was set between 10 to 20 l/min. For safety reasons, the gliding arc set up was shielded and grounded within a metal box with a ventilation system placed above it.

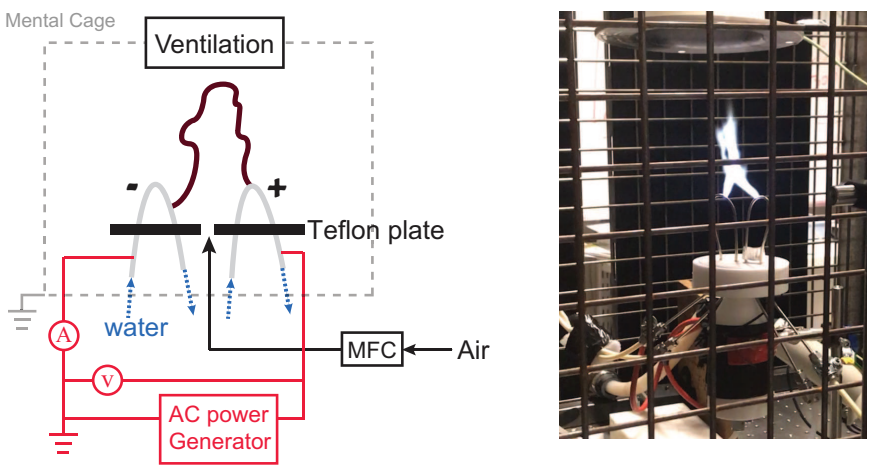

Figure 4.6: The sketch and a photo of the gliding arc set-up.

This gliding arc system has been investigated exceedingly by the group at the

combustion physics department of Lund university [58, 82, 108, 111, 112, 113, 114]. For example, the characterization of this system, including the electron number density and energy dissipation channels were analyzed using a current-voltage lumped model in [111]. Translational, rotational, vibrational and electron temperatures of the gliding arc discharge were measured by optical emission spectroscopy and laser-induced Rayleigh scattering in [58]. The effective removal of toluene using this system was reported in [63]. Simultaneous visualization of OH and CH_2O for a gliding-arc-assisted turbulent flame shows that the active species and thermal energy produced by the gliding arc stabilizes the flame [108]. A similar power supply from the same company (Generator 6030E), normally operating at a frequency of 31.25 kHz, has also been used by the group and reported in [81, 115].

4.2.2 Volumetric study of OH

Volumetric studies of OH around the gliding arc with different flow speeds were carried out using structured illumination LIF and FRAME. Four laser sheets were made parallel to each other with a gap of 0.5 mm as shown in figure 4.7. The LIF signal was directed to an iCCD camera (Gen 2 Istar, 1024 × 1024 pixels, Andor Instruments) by a mirror placed above the gliding arc. A band-pass Notch filter, centered at 310 nm ± 20 nm, was used to minimize the scattered laser light at 283.92 nm and broadband plasma emission. Single-shot images

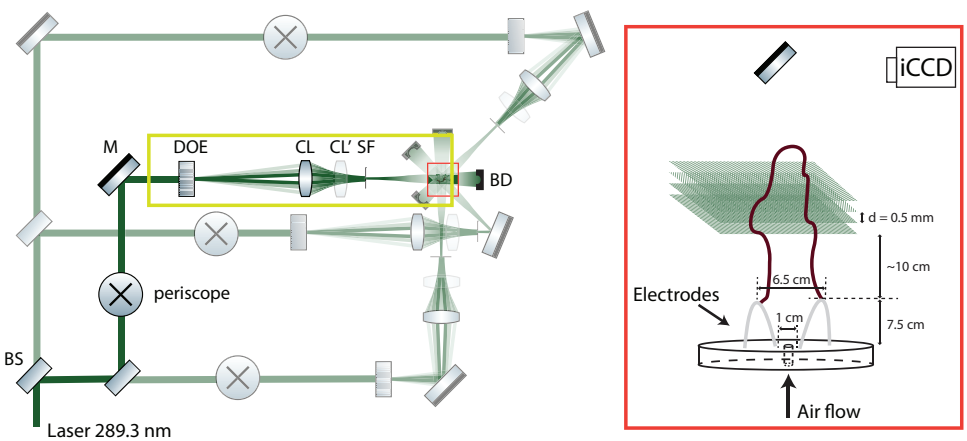

Figure 4.7: Optical arrangement for the experiment: BS- beam splitter, DOE- diffractive optical element, CL- vertically oriented cylindrical lens (f = 750 mm), CL- horizontally oriented cylindrical lens (f=1500 mm), SF- spatial filter, BD- beam dumps and d- separation distance between the laser sheets in the probe volume. The detailed optical arrangement of the modulated laser sheet creation as marked in the yellow box can be found in figure 3.5. Figure adapted from paper II.

were taken with a camera gate of 10 ns. The data analysis process including FRAME and 3D reconstruction is discussed in detail in paper II (figure 3) and section 3.3.1. In the following paragraphs, results, especially unpublished ones will be brought forward.

For this project, the investigation of the OH distribution around a gliding arc, the main focus was on the influence of the gas flow rate. Three different flow rates, 10, 15 and 20 l/min, were used. The maximum length of the gliding arc propagating along the gas flow is highly dependent on the gas flow rate [81]. The propagation of the gliding arc channel, i.e., the growth of the discharge channel, can be terminated by short-cutting and/or re-ignition events upstream of the discharge. The higher the flow rate is, the shorter the maximum length of the gliding arc will be. With a fixed position of the laser sheets, OH distribution around different parts of the gliding arc can be captured. Three examples of various positions of the cross section between the laser sheets and the gliding arc channel are shown in figure 4.8. The hollow structure of OH observed in the 3D reconstruction of the second example shown in figure 4.8 can never be achieved by any two dimensional images.

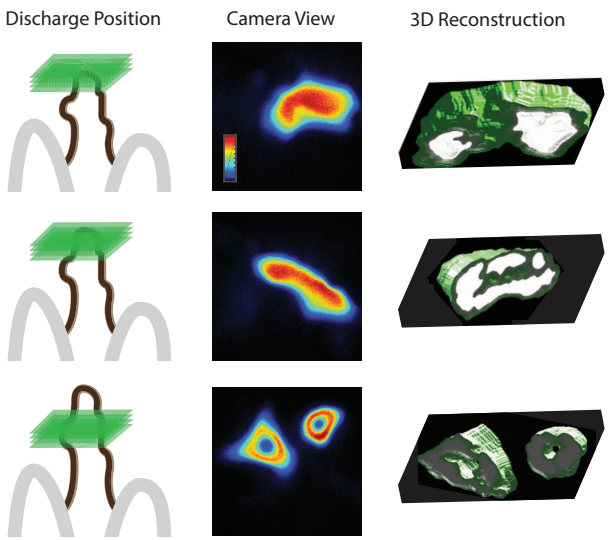

Figure 4.8: Examples of different results captured due to different positioning of the laser sheets in relation to the gliding arc.

When a complete hollow structure of OH distribution is captured, such as the third example given in figure 4.8. The angle between the propagating orientation of the discharge channel and the plane of the laser sheets can be calculated. This angle, denoted as α as shown in figure 4.5 and 4.9, can be used to render

3D-effect-free images by direct projection of the raw images to the plane perpendicular to the propagation of the gliding arc discharge. In figure 6 of paper II, the orientation of discharge channels from 6 pairs of ring-like OH distributions with respect to the position of the electrodes are shown. Here, the raw data, calibrated images without 3D-effect and the 3D reconstruction of the 6 pairs are shown in figure 4.9 with the same color code. Since $\alpha = 90°$ means that the laser sheets cross the discharge perpendicularly, i.e., no 3D-effect for the captured data, the smaller the α is, the more distortion can be observed between the raw images and calibrated 3D-effect-free images. For example, the ring-like OH structures given in figure 4.9a (top) and figure 4.9b (bottom) have been changed quite a lot by the projection process, while little difference can be noticed for the one in figure 4.9f (bottom right).

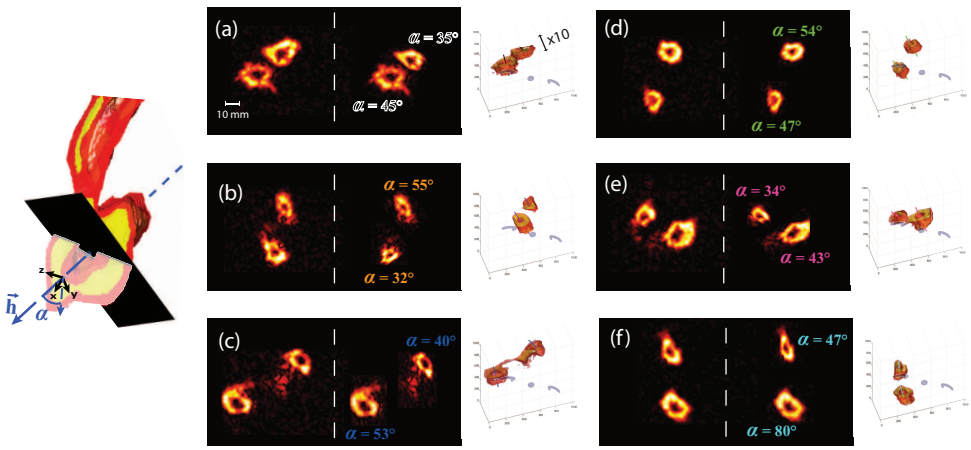

Figure 4.9: Examples of the raw PLIF images, 3D-effect-free imaging and 3D reconstruction of the OH around a gliding arc. The z axis of the 3D reconstruction is stretched tenfold for a better demonstration. The angle α of the plasma channel penetrating the ring-like OH distribution is indicated aside each ring.

The size of the calibrated ring-like OH distribution has been discussed and shown in figure 4.10 for different flow rates. The diameter of the OH distribution is denoted as D, while the diameter of the hollow structure inside the distribution is denoted as d. The hollow structure is referred to as the non-thermal-equilibrium zone as ground state OH is detected after turning off the power supply, indicating the existence of excited state of OH when the plasma is on [paper i]. The lower the flow rate is, the larger the size of the ring will be. If two such volumes merge, the local impedance will decrease. When the impedance through the volume, which has higher temperature and is rich with reactive and excited species, is lower than the impedance of the gliding arc channel downstream, a short-cutting event will take place. For a gliding arc running at lower flow rate, i.e., larger size of OH distribution, the likelihood of

short-cutting events will be higher (same as measured in figure 5 of [81]). As the total impedance of a gliding arc will be lowered after a short-cutting, higher probability of short-cuttings leads to lower probabilities of a re-ignition, which occurs when a new discharge channel is formed at the narrowest gap upstream between the electrodes. Re-ignition events completely terminate a gliding arc. Thus, a gliding arc channel can survive longer with less frequent occurring of re-ignitions, e.g., when operating with a lower flow rate with higher chance of short-cuttings.

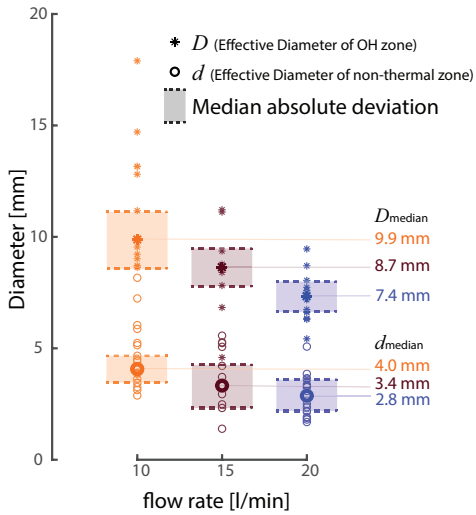

Figure 4.10: Effective diameters of 39 OH rings (D) and 55 non-thermal-equilibrium zones (d) at different flow rate conditions. Figure adapted from paper II.

4.3 The Siemens Energy burner

Another application for gliding arc discharges that has been studied in this thesis is a rotating gliding arc (RGA) system running in an industrial combustor. For industrial combustion applications, minimal NO_x emissions is crucial. A convenient and well-known solution to reduce these is to use lean premixed gas. The leaner the premixed gas can be, the less NO_x emission will be produced. However, when the premixed gas is too lean, the combustion becomes unstable and can no longer be sustained. One way to extend the Lean Blow-Out (LBO) limit of the flame is to use a plasma discharge. For example, a nanosecond repetitive pulsed discharge has been tested to extend the lean extinction limit of a swirled propane flame from global $\Phi = 0.4$ to 0.11 [22]. The active species, e.g., free electrons and atoms or molecules in excited states, generated by plasma discharge can help to stabilize the combustion at leaner conditions. In this thesis, a rotating gliding arc discharge generated by the same power supply as discussed in the section 4.2.1 has been applied in a downscaled Siemens Energy Dry Low Emission SGT-750 burner. Different diagnostic techniques have been used in order to study the plasma-assisted combustion process, including OH PLIF, high-speed videography of OH Chemiluminescence, flame emission spectroscopy and quantitative analysis of the CO and NO_x emission in the exhaust gas.

4.3.1 The Burner Configuration

A schematic of the Siemens Energy Dry Low Emission (DLE) SGT-750 burner (referred to as the Siemens Energy burner in this thesis) is shown in Figure.4.11. The principle and history of the development of DLE burners can be found in [116]. There are three stages of this burner: the Rich Pilot Lean (RPL), the Pilot and the Main. The high-voltage electrode was integrated inside the RPL of the burner with the wall of the RPL being grounded. The rotation of the discharge was achieved by two sets of swirler vanes, mounted on the exit of the Pilot and Main respectively. To carry out optical diagnostics, quartz windows were used downstream of the Main. When operating, the total thermal power of the flame was varied between 78 to 98 kW while the average power produced by the RGA was 75 to 82 W, which is merely 0.1 % of the total thermal power. Premixed methane-air flow was fed to the Pilot and Main with the air preheated to 400 $^{\circ}C$. Two different gases were sent to RPL in this project: air or oxygen. For safety reasons, the RPL is always full of air upon ignition of the flame. A schematic of the experiment set-up can be found in figure 2 of paper III.

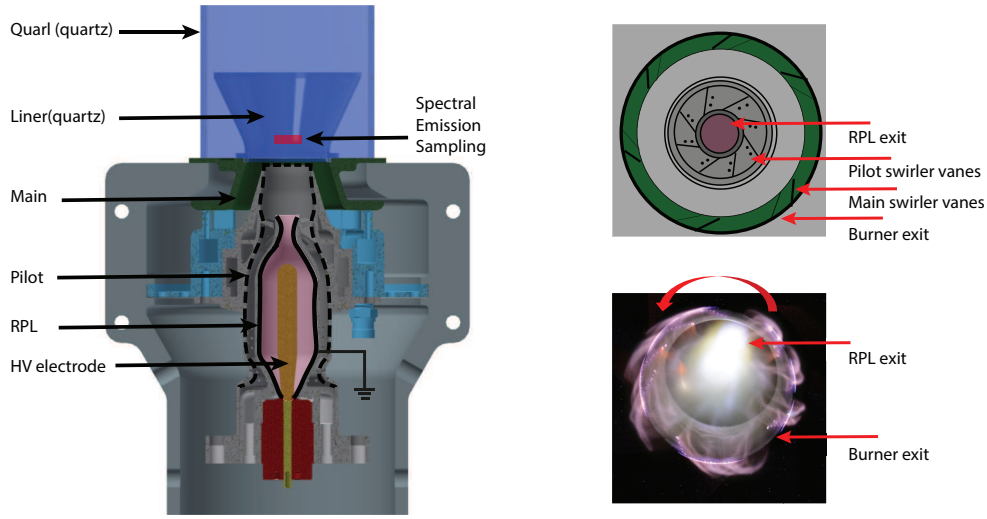

Figure 4.11: A stech of the Simens burner with the top view of the burner showing the pilot and main swirlers and a photo of the discharge captured by a standard digital camera. (Figure adapted from paper III.)

4.3.2 Stabilization of the flame

Stabilization of the flame was captured by both a standard digital camera and high-speed OH chemiluminescence. Photos of the flame for different global Φ with/without RGA are shown in figure 4.12. For this burner, a central recirculation zone (CRZ) anchoring on the Main exit created by the vortex breakdown of swirling flow will be observed if the flame is stable [117, 118, 119, 120]. The central recirculation zones, also named as inner recirculation zones, are created aerodynamically by the spiral motion of swirling flows. The flow structure of a typical gas turbine combustor is shown to the left in figure 4.12. When stabilization of a flame is lost, the flame will be stretched downstream as shown on the very left photos of each condition in figure 4.12. If the global Φ continues to go leaner, the flame will eventually blow out. It can be seen that the LBO limit is extended from global $\Phi = 0.48$ to 0.46 for air in PRL, and from 0.47 to 0.44 for oxygen in RPL respectively.

Besides the flame configuration, another parameter that has been used to characterize the flame stability is the CO emission level. The LBO event can be identified by an exponential increase of CO emission as plotted in figure 4.13. As the equivalence ratio goes down, the CO emission keeps decreasing until the LBO limit is reached, from which an dramatic increase of CO emission is observed. This shows that the LBO limit is a very important parameter for

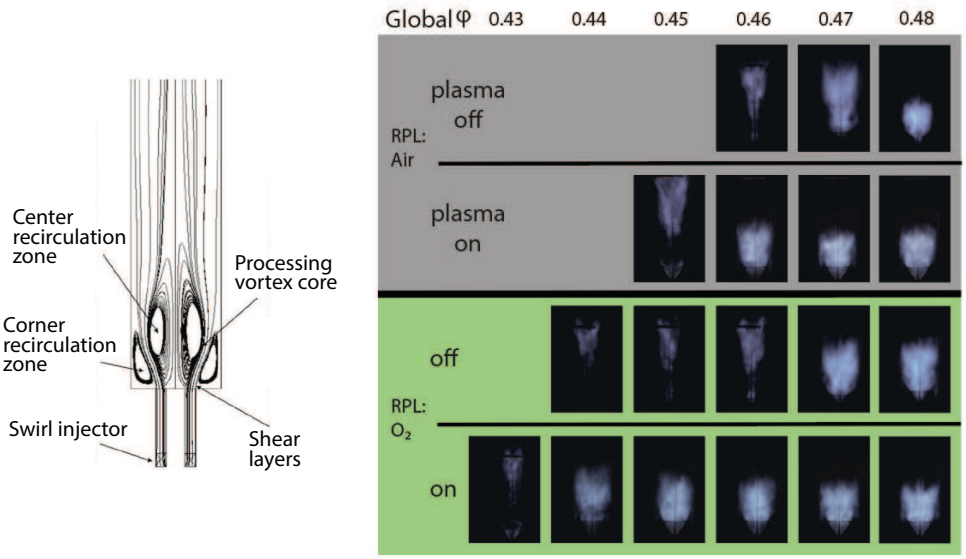

Figure 4.12: (left) Example of the flow structure of a gas turbine with coaxial swirl injector [121]. (right) Photographs of the flame configuration at different global ϕ with/without the RGA.

industrial gas turbines that operation at the lowest possible equivalence ratio before LBO is optimal for minimal CO and NO_x emission.

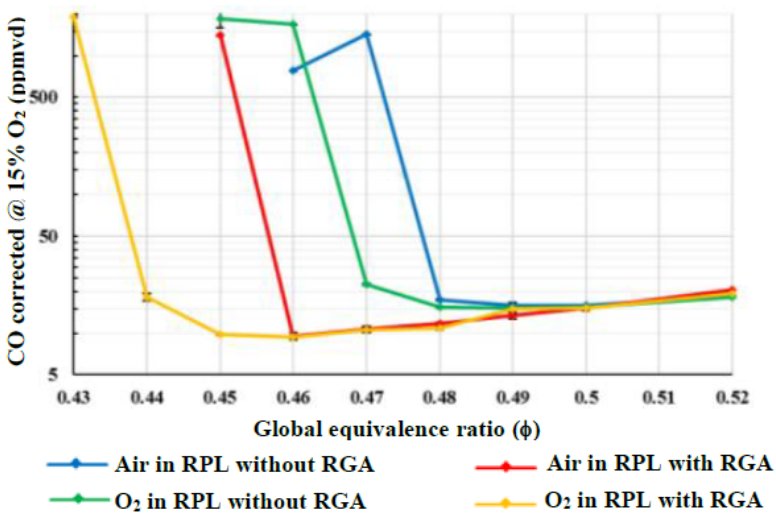

Figure 4.13: CO emission level for different gas injection in RPL at different global Φ. The unit used for the emission level, ppmvd (parts per million by volume dry), is a standard unit used for emission concentration. The @15 % O_2 indicates that all the values are normalized to a same O_2 level: 15%.

The stabilization process of a close-to-LBO flame, captured by high-speed (1 kHz) OH chemiluminescence, is presented in figure 4.14. While the flame configuration of $\Phi = 0.47$ with air in RPL was only a bit stretched out compared to the leaner case where $\Phi = 0.46$ as shown in figure 4.12, the OH chemiluminescence before and after the stabilization of the flame displays evident differences. When the RGA is turned on, a rotating flame kernel is introduced to the flame. Interactions between the flame kernel and the flame itself re-establishes the CRZ of the flame in approximately 10 ms. More information about the flame structure, analyzed by OH PLIF signal, can be found in paper IV.

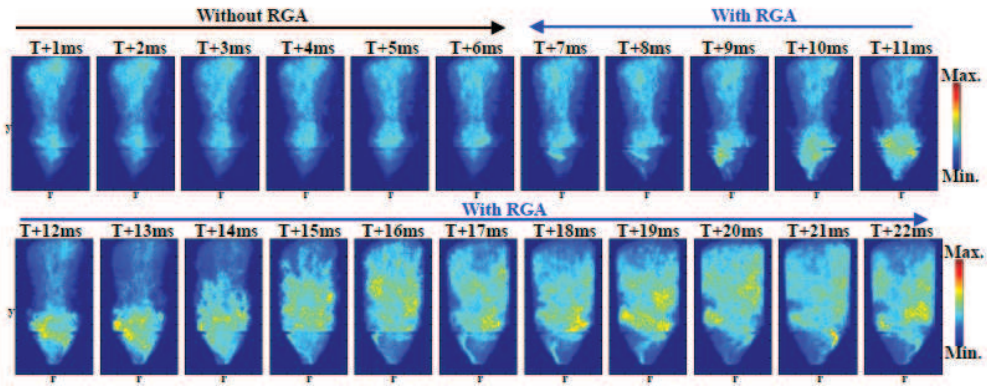

Figure 4.14: Chemiluminescence of OH showing the stabilization of a close-to-LBO flame (global $\Phi = 0.47$ with air in PRL) with the assistance of the RGA.

4.3.3 Optical emission of the flame

Optical emission of the flame was captured using two spectrometers: a fiber spectrometer (AvaSpec-ULS2048XL-EVO-RS-UA) and a Czerny-Turner spectrometer (Andor Shamrock 750, 1200 l/mm blazed at 300 nm) with a CCD camera (Andor iDus 420-OE). The fiber spectrometer covers a wide range between 200 nm to 1160 nm and was used to record the overall spectra of the flame emission. The Czerny-Turner spectrometer was used to capture the oxygen A band with higher resolution and sensitivity. The gate of the spectrometer was set to 500 ms for the fiber spectrometer and 1 s for the Czerny-Turner/CCD system.

Average spectra of the flame emission captured with global $\Phi = 0.49$ with/without the RGA is shown in figure 4.15. Without RGA, the $OH(A - X)$ peak around 310 nm and peaks in the near-infrared range were observed in the spectra from

the flame. No difference was observed for the OH peak when replacing the air with oxygen in the RPL, while the infrared peaks were slightly stronger with oxygen in RPL. However, when the RGA is turned on, a large number of ionized and/or excited molecules/atoms are created by the free electrons as well as considerable heat release. As a result, the flame emission gets more intense, where all peaks are approximately 2 to 3 times stronger compared with the spectrum of the pure flame. In addition, more peaks appear when the RGA is turned on: another band of the $OH(A-X)$ transition around 283 nm, the $CH(A-X)$ transition around 430 nm and two relatively strong peaks at 590 nm and 767 nm, which arise from the Sodium- (3p to 3s) and Potassium D-lines (4p to 4s).

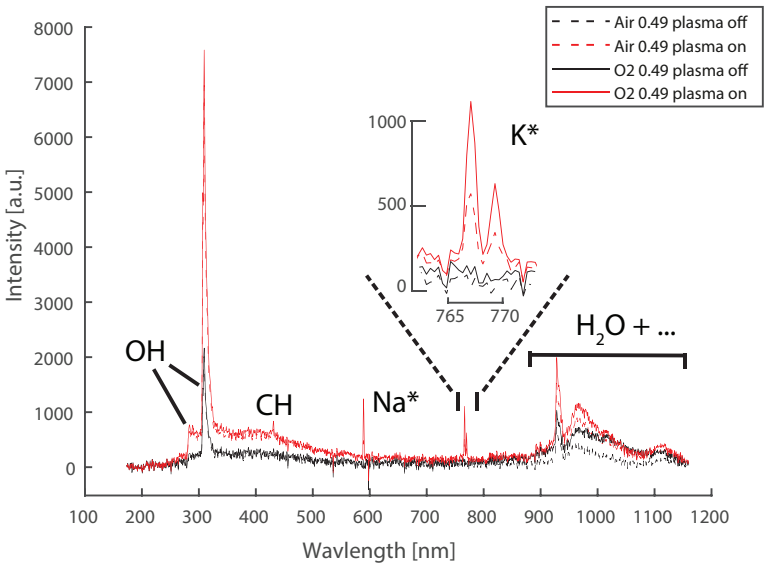

Figure 4.15: Average spectra (from 100 measurements) of the flame emission with/without RGA running at global $\Phi = 0.49$.

The spectra between 750 nm to 780 nm was also measured with the Andor spectrometer with higher resolution where the split between the pair of P and PQ lines of oxygen A band is well-resolved. Single-shot spectra of the molecular oxygen captured with/without RGA are shown in figure 4.16. Both the (0-0) band, i.e. the A band, and the (1-1) band are observed. For the A band, the whole band structure was captured with a band head of R and RQ branches around 760 nm and groups of P and PQ pairs on the longer wavelength range. For the (1-1) band, however, only the band head structure around 768 nm between the two K^* peaks was measured. For cases with air in the RPL, the emission becomes stronger when the flame is richer, while for RPL filled with O_2, non-linear increase of the emission was observed with a big jump when

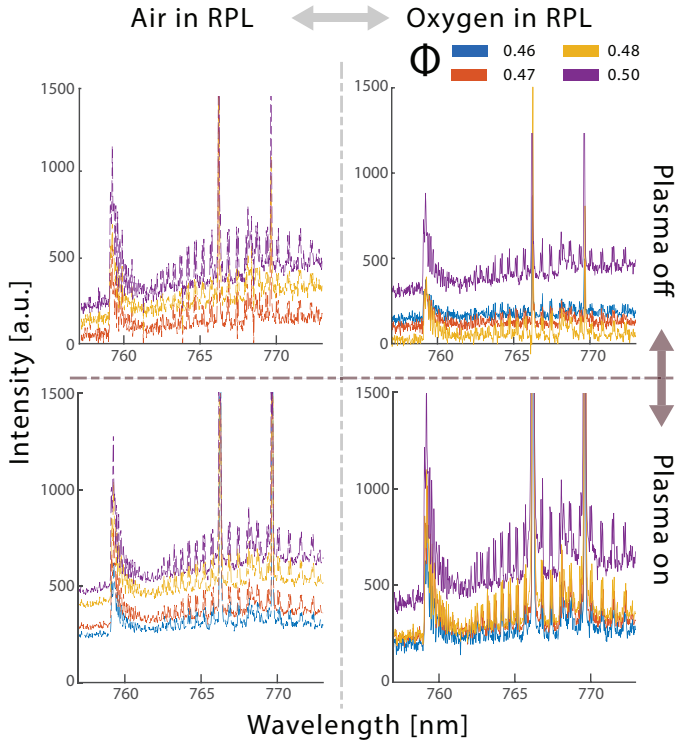

Figure 4.16: Single-shot spectra of the flame emission in different conditions. Note that the K^* peaks are out of the scale for a better presentation of the A band.

the equivalence ratio reaches 0.5. When the RGA was introduced in the RPL, the emission from molecular oxygen is approximately two times stronger with the RPL filled with O_2. This plasma-induced oxygen emission is, however, less obvious when the RPL is operating with air.

4.4 Nanosecond pulsed discharge

An nanosecond pulsed discharge (NPD), with a pulse duration of 4 ns (FWHM) and repetition rate of 1 Hz, has been applied on a lifted CH_4-Air flat flame at atmospheric pressure to study the formation dynamics of the discharge and plasma-assisted combustion. The flat flame is supported by a McKenna burner with a round flow stabilizer placed around 30 mm above the surface of the burner. To lift the flame, the equivalence ratio of the premixed flame was set to be 0.62 with 0.84 SLPM CH_4 and 13.5 SLPM Air. Two configurations of the electrodes are used as shown in figure 4.17a, with the pin-to-pin one reported in paper VI and the pin-to-plane one reported in paper VII. The power supply of the NPD is manufactured by *FID* with the operation range from 30 kV to 200 kV and a maximum repetition rate of 1 kHz.

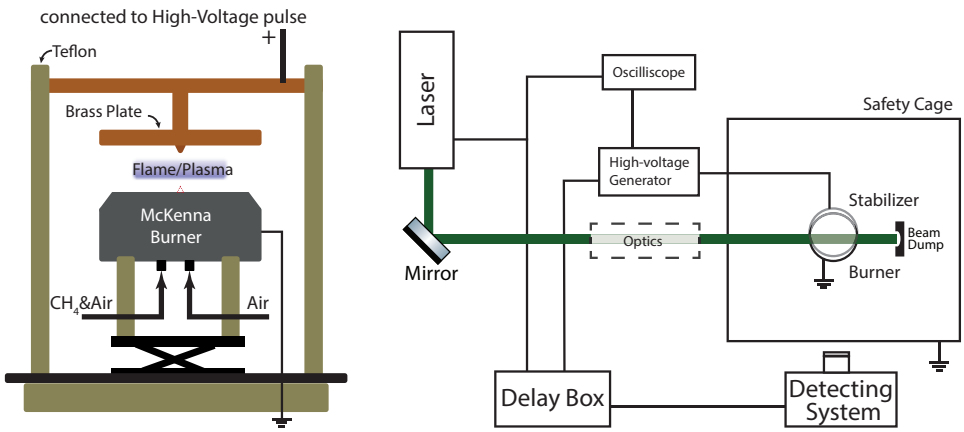

Figure 4.17: (a) Sketch of a the burner. The tip placed on the center of the burner surface (marked with dashed red line) is removed for the pin-to-plane electrode configuration. (b) Experimental set-up for NPD measurements. Laser system, optics and detecting system (either an iCCD/iCOMS camera or a spectrometer with a camera) are different for different measurements.

General experimental set-up for NPD measurements is given in figure 4.17b. For safety reasons, the burner is placed inside a mental cage which has to be locked before switching on the high-voltage power supply. The mental cage also works as a Faraday cage to shield the strong electromagnetic fields generated by the NPD which disturbs electronic devices such as the camera and the delay box. In addition, the ventilation exhaust, placed right above the burner, is turned on during the operation. The laser system, optical arrangement and the detecting system are different for different measurements. Detailed information regarding the specific equipment used in each set-up can be found in the corresponding publications.

The laser system, the high-voltage generator and the detecting system are synchronized by being externally triggered with signals generated from a delay box. The time jitter between the high-voltage pulse and the laser/camera imaging system is several nanoseconds, which is similar to the FWHM of the NPD. For dynamic studies of the discharge formation, jitter correction is required to arrange captured images in a correct time sequence. To compensate the time jitter, for each plasma formation event, the trigger signal to the laser/camera system and the monitor signal from the high-voltage pulse generator are captured simultaneously with a 6 GHz oscilloscope as shown in figure 4.18. In this way, the actual capturing time of each image in relation to the plasma discharge is known and the time jitter is corrected.

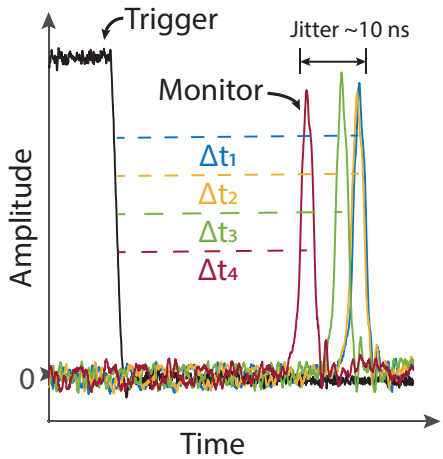

Figure 4.18: Time jitter between the high-voltage pulse and the laser/camera system. (Figure adapted from paper V.)

Laser scattering measurements were preformed to capture the formation dynamics of the discharge while LIF measurements of CH_2O were preformed to study PAC hundreds of nanosecond after the discharge. Optical emission spectrum of the plasma emission was captured, and both rotational and vibrational temperature were calculated by fitting the spectra of N_2 (C-B) transition with SPECAIR.

4.4.1 Formation dynamics of the NPD

Photographs of the flame during an NPD of 30 kV is shown on 4.19a. For the pin-to-pin electrode configuration, a discharge channel is created between the two tips with a secondary flame ignited in the unburnt region close to the anode. For

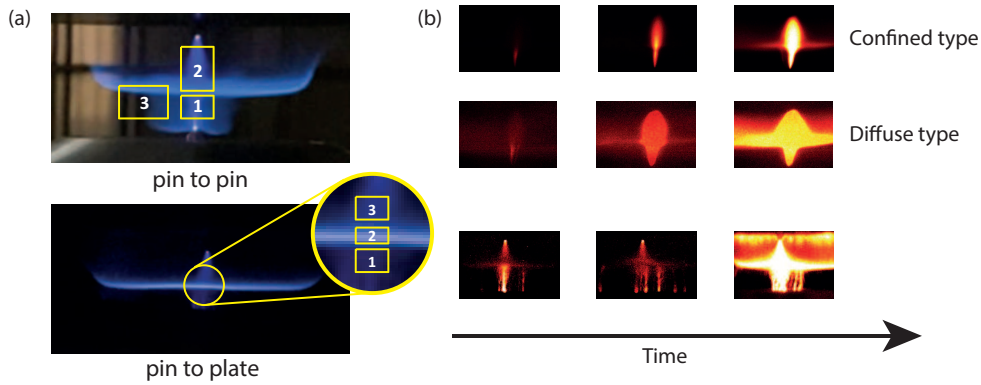

Figure 4.19: (Left) Photographs of the NPD-stimulated flame with pin-to-pin (top) and pin-to-plane (bottom) electrode configurations. The areas marked with yellow frames represent the three different regions of the flame for each configuration. (Right) Three images of the plasma emission captured during a discharge event. Two different types of discharge are observed for the pin-to-pin configuration. Note that same colorbar range was used for each image sequence with the exception of the pin-to-plane electrode configuration where the maximum value of the colorbar range for the last image is 4 times larger than the previous two.

the pin-to-plane electrode configuration, however, brush-like streamers between the anode and flamefront (region one) was observed. The bruch-like streamers can be seen more clearly from the plasma emission images captured with an iCCD camera, as shown on figure 4.19b.

Two different types of plasma were observed for the pin-to-pin electrode configuration: a confined type with strong emission from the discharge channel between the two tips, and a diffuse type where plasma emission is more diffuse and also one order of magnitude weaker. For this configuration, plasma emission always starts from a small area near the anode where the electrons start to build up. Once the discharge channel is formed, the intensity of the plasma emission increases immediately. The time when strong plasma emission from the streamer is observed is defined as time zero. The streamer formed with both the pin-to-pin and pin-to-plane electrode configuration is negative.

To further study the formation dynamics of the plasma, laser scattering with structured illumination is applied on the pin-to-pin configuration. With structured illumination, strong plasma emission is cleared out using a lock-in algorithm and imaging of laser scattering signal is achieved as shown in figure 4.20. Detailed information about the experimental set-up, optical arrangement and data analysis process can be found in paper V (figure 2 and figure 3). Similar to what is shown in figure 4.19, the plasma emission for the confined-type is so strong (approximately 10 times stronger than the diffuse type) that it is almost impossible to distinguish the scattered laser signal with sinusoid pattern. However, as strong as the plasma emission is, it is still possible to extract the

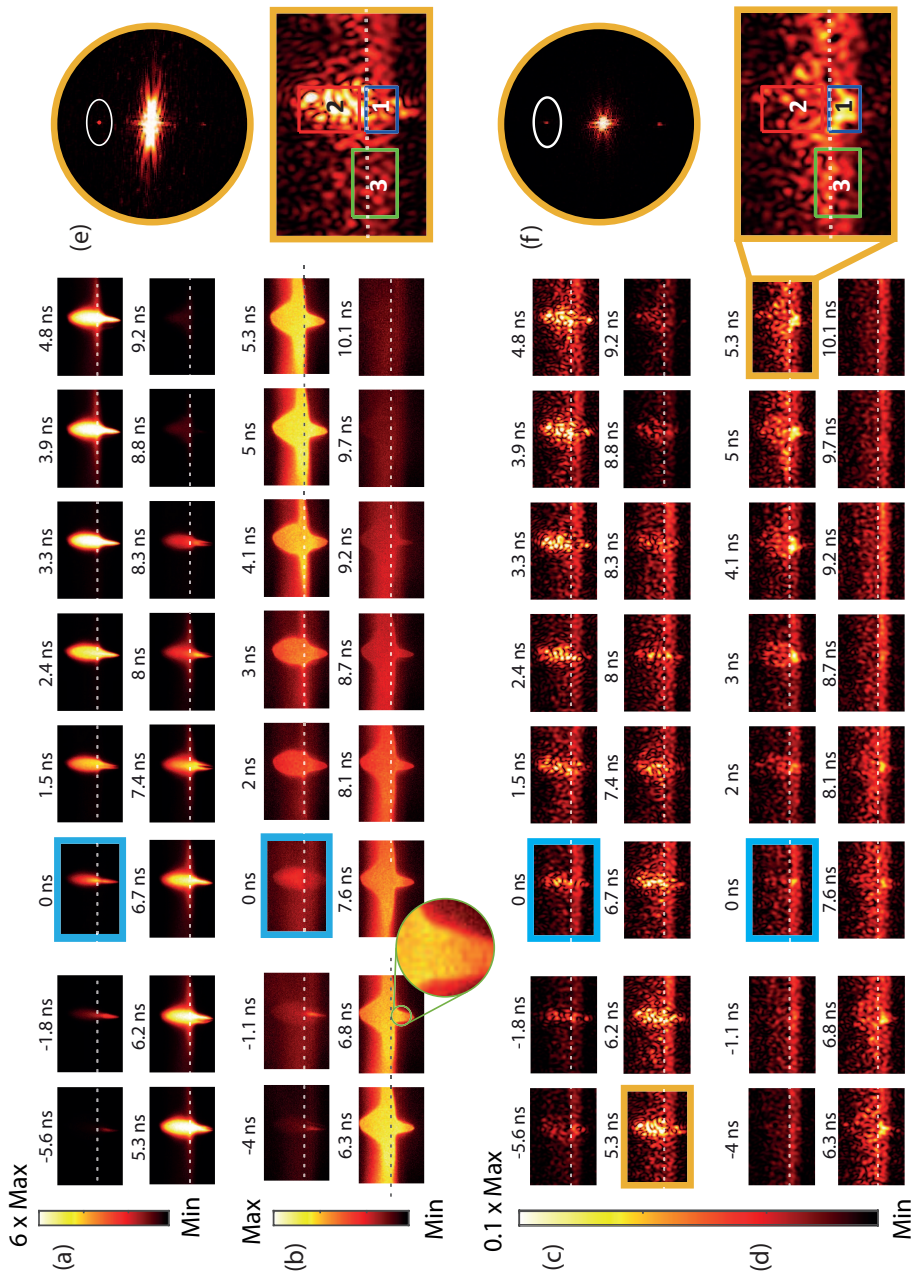

Figure 4.20: Single-shot imaging of the plasma emission and laser scattering with structured illumination at different times during a discharge with a pin-to-pin electrode configuration. (a-b) Raw data, (c-d) processed data and (e-f) the Fourier domain and magnified processed data at t = 5.3 ns for two different type of plasma. The dashed line on each image is the position of the flamefront.

modulated scattering signal out in the Fourier domain as shown in figure 4.20e-f. The Fourier domain of the image captured at t = 5.3 ns for the confined-type and diffuse-type plasma are given in figure 4.20e and f respectively. Although the dc component for the confined-type is much stronger, the modulated signal for the two types can both be well-separated from the unmodulated DC component. The processed images using an ellipse filter marked by the white circle in Fourier domain in figure 4.20e and f is given in figure 4.20b and d. The scattering signal for both types displays similar signal intensity regardless how strong the interference of the plasma emission is. Being able to deliver plasma-emission-free signals shows how powerful the laser/optical technique combining structured illumination and lock-in algorithm is for diagnostics of plasma-related phenomena.

The dynamics of the scattering signal from three different regions of the flame is analyzed separated. The three regions as marked in figure 4.19a and 4.20e-f are: region one, the unburnt region along the discharge channel between the two pins close to the anode; region two, the postflame region along the discharge channel close to the cathode; region three, the region aside from the center discharge channel including unburnt gas, flamefront and postflame. Temporal profiles of the average signal intensity from these three regions are plotted in figure 4.21. The results indicate that the distribution of laser scattering signal is different for the two plasma types. Stronger signal from region 2 is recognized

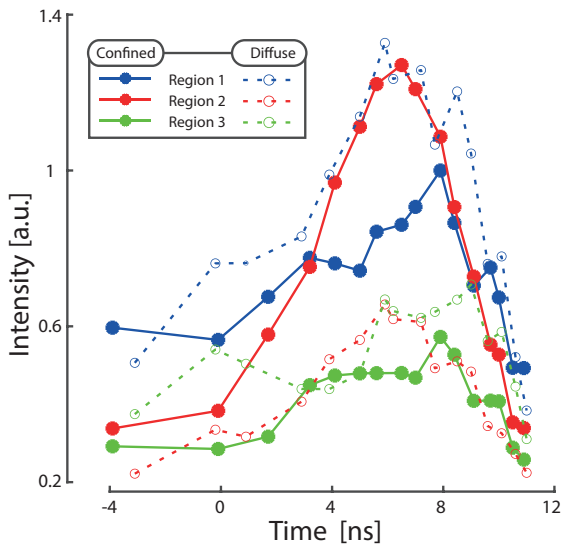

Figure 4.21: Temporal profile of the laser scattering signal captured at the three regions of the NPD-stimulated flame with a pin-to-pin electrode configuration.

for the confined-type while signal from region 1 is the strongest for the diffuse-type. The different signal distribution demonstrates that the diffuse-type plasma was formed in a larger volume of the flame while the confined-type is more concentrated in the discharge channel between the two electrodes. Assuming the scattering signals in region 1 and 3 are mainly from charged particles as these regions overlap with the path of discharge channel, the shift of the peak of the signal from region 1 (at around t = 5 ns, blue dashed line) to region 3 (at around t = 8 ns, green dashed line) can be an indicator of the plasma induced effect of the flame. Indeed, further investigations are required to confirm this speculation.

4.4.2 Temperature measurement

Optical emission from the three regions as marked in figure 4.19a with the pin-to-plane electrodes configuration was taken with a spectrometer (Shamrock 750,

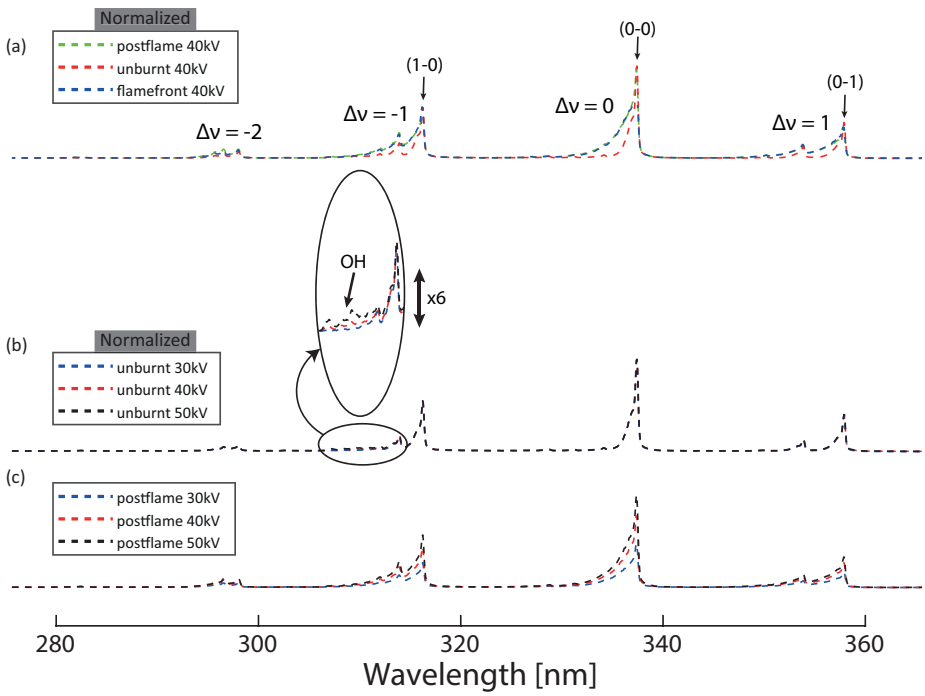

Figure 4.22: Averaged spectra (100 measurements) of the NPD-stimulated methane-air flame with pin-to-plane electrode configuration. The positions of the three regions (unburnt, flamefront and postflame) are marked in figure 4.19a. In (a) and (b), the intensity of the signal is normalized with respect to the peak of the (1,0) band from the unburnt region with an applied voltage of 40 kV. The peak of (0,0) band from flamefront with V = 40 kV shown in (a) was not captured as the camera was saturated.

Andor Instruments) and an iCCD camera (Gen 2 IStar, Andor Instruments). The spectrum between 275 nm to 365 nm was calibrated using a standard Deuterium lamp (Cathodeon R07). Several bands of the $N_2(C-B)$ transition were detected as shown on figure 4.22. Spectra taken with an applied voltage $V = 40$ kV are shown in figure 4.22a in which the signal intensity is normalized with respect to the peak of (1,0) band from the unburnt region. Different band structure indicates different rotational and vibrational temperatures which will be further discussed later in figure 4.23 and figure 4.24. Spectra from the unburnt, flame front and postflame regions were also analysed with different applied voltage (from 30 kV to 50 kV). Normalized spectra from all the three regions shows no difference in terms of the rotaional and vibrational distribution of $N_2(C-B)$, implying that the rotational and vibrational temperature of the $N_2(C)$ state is independent of the amplitude of the high voltage pulse in the range between 30 kV to 50 kV. However, enhanced OH peaks around 310 nm from the $OH(A-X)$ transition were observed with a higher voltage in the unburnt region as shown in figure 4.22b. The absolute intensity of the spectra, on the other hand, is stronger when the applied voltage $V = 50$ kV, indicating that a larger number of $N_2(C)$ are produced with higher electric field. An example of the nonnormalized spectra taken from the postflame region with different applied voltage of the NPD is shown in figure 4.22c. The integrated peak areas for groups of bands sharing a same $\Delta\nu$ are calculated. Peak areas with $V = 40$ kV and $V = 50$ kV is about 1.7 and 2.1 times larger than the ones with $V = 30$ kV respectively.

Rotational and vibrational temperatures were calculated by fitting the experimental data with theoretical spectra generated by a software named *SPECAIR*. For $N_2(C)$ with different vibrational temperatures, the line strength of bands with a same $\Delta\nu$ will be different. The higher the temperature, the vibrational states with a higher ν' will be more populated. The distribution of ro-vibrational states within a band, however, is more sensitive to the rotational temperature. Ro-vibrational states with a high J value will be more populated with a higher rotational temperature.

The spectrum of (0-1) (1-2) and (2-3) bands ($\Delta\nu = 1$) taken with grating of 300 l/mm were used to calibrate the vibrational temperature (See figure 4.23 for flamefront region). Before fine-tuning the vibrational temperature, rotational temperature were first found by fitting with band structure of (0-1). As shown in figure 4.23, the band structure of each individual band is not sensitive to vibrational temperature. The vibrational temperature of $N_2(C)$ in the unburnt-, flamefront- and postflame region is around 3200 K ($\pm 200K$), 3600 K ($\pm 200K$) and 4200 K ($\pm 200K$) respectively .

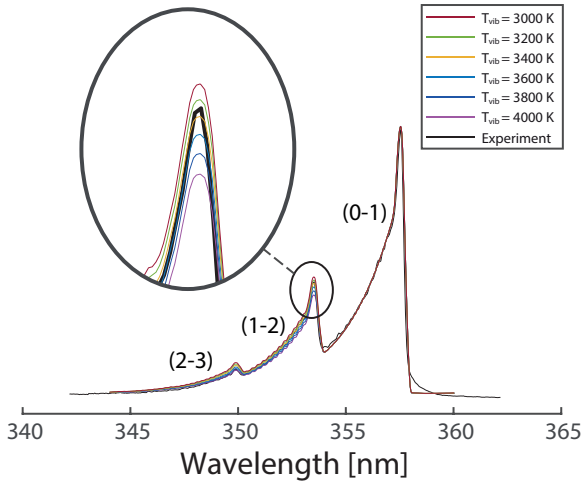

Figure 4.23: Spectral fitting for vibrational temperatures.

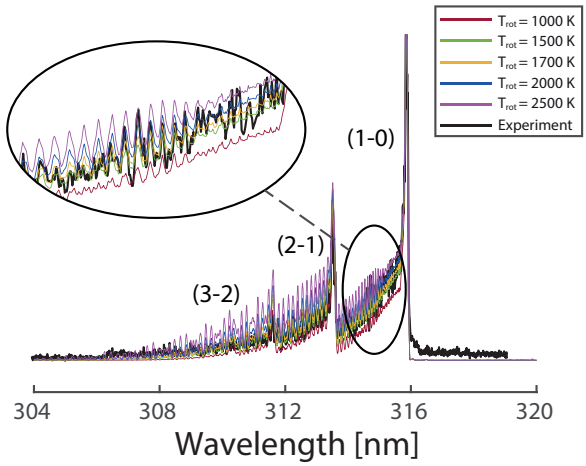

Figure 4.24: Spectral fitting for rotational temperatures.

Fine tunning of the rotational temperature could be achieved by fitting the spectrum of (3-2)(2-1)(1-0) bands ($\Delta\nu = -1$) taken with a grating of 2400 l/mm. The rotational temperature of postflame zone and flamefront zone is both around 1700 K while the rotational temperature of the unburnt region is about 300 K. These results coincide quite well with the translational temperature measured by structured Rayleigh scattering thermometry. This indicates that for this set-up, the gas temperature could be roughly represented by the rotational temperature of $N_2(C)$.

Chapter 5

Conclusions and Outlooks

In this thesis, coded imaging was introduced for diagnostics of plasma-related phenomena for the first time. In addition, plasma-assisted combustion phenomena and applications have been investigated in a laminar flat flame as well as in an down-scale industrial burner, respectively. Here in the final chapter of this thesis, a short conclusion and some outlooks of this work are given in the order as they were discussed in Chapter 4.

Periodic shadowing was applied for streak camera measurements where both higher temporal contrast and effective dynamic ranges have been achieved. Hence, we are able to more accurately describe temporal dynamics of both strong and weak swift signals simultaneously of transient phenomena. This technique is a great asset for plasma-related measurements to, for example, capture dynamics of plasma emission, of which the intensity may change dramatically within a few nanoseconds. This approach is both straightforward, cost-efficient and versatile, and I sincerely hope it will be implemented in future streak camera measurements.

FRAME was applied for 3D reconstruction of OH distribution around a gliding arc discharge while simultaneously mitigating plasma emission interference. The successful demonstration of this technique for volumetric studies of plasma-related diagnostics shows the potential of FRAME being used for other plasma-related phenomena. Volumetric information of rapid dynamics are particularly important for plasma-assisted turbulent combustion, where both the plasma and the turbulent flame are transient and have complex three-dimensional structures. Such investigations can be carried out for plasma-assisted combustion using both nanosecond pulsed discharge and gliding arc discharge.

Plasma-assisted combustion in a Siemens Energy Dry Low Emission burner using a rotating gliding arc was investigated where the lean-blow-out limit of the burner has been extended without any significant increase of NO_x emission by an addition of only 0.1% electrical energy. This is the first time that a rotating gliding arc has been applied in an industrial size burner with a total power above 50 kW. Further investigations of PAC using a rotating gliding arc could be carried out to mitigate thermoacoustic instabilities and increase fuel flexibility including multiphase non-fossil fuels. In a long term perspective, it could eventually be integrated in industrial facilities.

A considerable part of the thesis, on which most time and energy were spent, is investigations and applications using a nanosecond pulsed discharge. Build up and characterization of this system have been done with a load configuration where a lifted flat flame and both pin-to-pin and pin-to-plane electrode configurations were used. Various optical/laser techniques have been used to measure for example species distribution and temperature dynamics. Previous research has shown that secondary streamer produced by NPD starts to appear around 10 ns [122] and the shorter the rise time of a high-voltage pulse is, the higher yield efficiency of active species will be achieved [123]. The pulse duration of this power supple is only 4 ns (FWHM), which is shorter than most of other reported NPS with a FWHM of $\approx$ 10 ns. The mechanism of the breakdown and yield efficiency for active radicals, to name a few, is thus unique for this set-up and should hence be further investigated.

For future development of plasma-assisted combustion using this NPS, different electrode configurations and load geometry could be tested to, for example achieve fast breakdown process in order to avoid unnecessary gas heating, or create a plasma that distributed in a large volume. Plasma that can be formed within few nanosecond in a large volume is essential for plasma-assisted turbulent combustion due to the rapidly varying flow dynamics of a turbulent combustion.

As this thesis is mostly about the development of optical diagnostics of plasma-related phenomena and applications, optical/laser diagnostics techniques could be further developed for measurements of the key parameters in a plasma, such as the electron number density, reduced electric field, singlet oxygen, ozone, and electron/vibrational/rotational temperatures. For example, photolytic-interference-free PLIF imaging of OH could be carried out using laser with mode-locked lasers instead of conventional nanosecond lasers.

Reference

[1] Francis F Chen. *Introduction to Plasma Physics*. Springer Science & Business Media, 2012.

[2] Robert J Goldston. *Introduction to Plasma Physics*. CRC Press, 2020.

[3] Paul M Bellan. *Fundamentals of Plasma Physics*. Cambridge university press, 2008.

[4] Sneha Samal. Thermal plasma technology: The prospective future in material processing. *Journal of Cleaner Production*, 142:3131–3150, January 2017, doi:10.1016/j.jclepro.2016.10.154.

[5] J Reece Roth. *Industrial Plasma Engineering: Volume 2: Applications to Nonthermal Plasma Processing*. CRC press, 2001.

[6] S Müller and R-J Zahn. Air pollution control by non-thermal plasma. *Contributions to Plasma Physics*, 47(7):520–529, 2007, doi:10.1002/ctpp.200710067.

[7] Hyun-Ha Kim. Nonthermal plasma processing for air-pollution control: A historical review, current issues, and future prospects. *Plasma Processes and Polymers*, 1(2):91–110, 2004, doi:10.1002/ppap.200400028.

[8] Jim Van Durme, Jo Dewulf, Christophe Leys, and Herman Van Langenhove. Combining non-thermal plasma with heterogeneous catalysis in waste gas treatment: A review. *Applied Catalysis B: Environmental*, 78(3-4):324–333, 2008, doi:10.1016/j.apcatb.2007.09.035.

[9] Rino Morent, Nathalie De Geyter, Johan Verschuren, Karen De Clerck, Paul Kiekens, and Christophe Leys. Non-thermal plasma treatment of textiles. *Surface and coatings technology*, 202(14):3427–3449, 2008, doi:10.1016/j.surfcoat.2007.12.027.

[10] R Foest, E Kindel, A Ohl, M Stieber, and KD Weltmann. Non-thermal atmospheric pressure discharges for surface modification. *Plasma Physics and Controlled Fusion*, 47(12B):B525–B536, 2005, doi:10.1088/0741-3335/47/12B/S38.

[11] Thierry Paulmier and Laurent Fulcheri. Use of non-thermal plasma for hydrocarbon reforming. *Chemical engineering journal*, 106(1):59–71, 2005, doi:10.1016/j.cej.2004.09.005.

[12] Yun Yang. Methane conversion and reforming by nonthermal plasma on pins. *Industrial & engineering chemistry research*, 41(24):5918–5926, 2002, doi:10.1021/ie0202322.

[13] C Meyer, S Müller, EL Gurevich, and J Franzke. Dielectric barrier discharges in analytical chemistry. *The Analyst*, 136(12):2427–2440, 2011, doi:10.1039/C0AN00994F.

[14] Jing Hu, Wei Li, Chengbin Zheng, and Xiandeng Hou. Dielectric barrier discharge in analytical spectrometry. *Applied Spectroscopy Reviews*, 46(5):368–387, 2011, doi:10.1080/05704928.2011.561511.

[15] Beate Haertel, Thomas Von Woedtke, Klaus-Dieter Weltmann, and Ulrike Lindequist. Non-thermal atmospheric-pressure plasma possible application in wound healing. *Biomolecules & therapeutics*, 22(6):477, 2014, doi:10.4062/biomolther.2014.105.

[16] Hyun Woo Lee, Seoul Hee Nam, Abdel-Aleam H Mohamed, Gyoo Cheon Kim, and Jae Koo Lee. Atmospheric pressure plasma jet composed of three electrodes: Application to tooth bleaching. *Plasma Processes and Polymers*, 7(3-4):274–280, 2010, doi:10.1002/ppap.200900083.

[17] Gregory Fridman, Alexy Shereshevsky, Marie Peddinghaus, Alexander Gutsol, Victor Vasilets, Ari Brooks, Manjula Balasubramanian, Gary Friedman, and Alexander Fridman. Bio-medical applications of non-thermal atmospheric pressure plasma. In *37th AIAA Plasmadynamics and Lasers Conference*, page 2902, 2006.

[18] Yiguang Ju and Wenting Sun. Plasma assisted combustion: Progress, challenges, and opportunities. *Combustion and Flame*, 162(3):529–532, March 2015, doi:10.1016/j.combustflame.2015.01.017.

[19] Yiguang Ju and Wenting Sun. Plasma assisted combustion: Dynamics and chemistry. *Progress in Energy and Combustion Science*, 48:21–83, June 2015, doi:10.1016/j.pecs.2014.12.002.

[20] Steven Chu and Arun Majumdar. Opportunities and challenges for a sustainable energy future. *Nature*, 488(7411):294–303, August 2012, doi:10.1038/nature11475.

[21] A.Yu. Starikovskii. Plasma supported combustion. *Proceedings of the Combustion Institute*, 30(2):2405–2417, January 2005, doi:10.1016/j.proci.2004.08.272.

[22] S. Barbosa, G. Pilla, D. A. Lacoste, P. Scouflaire, S. Ducruix, C. O. Laux, and D. Veynante. Influence of nanosecond repetitively pulsed discharges on the stability of a swirled propane/air burner representative of an aeronautical combustor. *Philosophical Transactions of the Royal Society A: Mathematical, Physical and Engineering Sciences*, 373(2048):20140335, August 2015, doi:10.1098/rsta.2014.0335.

[23] Sergey Shcherbanev, Titouan Morinière, Roberto Solana-Pérez, Markus Weilenmann, Yuan Xiong, Ulrich Doll, and Nicolas Noiray. Anchoring of premixed jet flames in vitiated crossflow with pulsed nanosecond spark discharge. *Applications in Energy and Combustion Science*, 1–4:100010, December 2020, doi:10.1016/j.jaecs.2020.100010.

[24] Timothy Ombrello, Sang Hee Won, Yiguang Ju, and Skip Williams. Flame propagation enhancement by plasma excitation of oxygen. Part I: Effects of O3. *Combustion and Flame*, 157(10):1906–1915, October 2010, doi:10.1016/j.combustflame.

[25] Timothy Ombrello, Sang Hee Won, Yiguang Ju, and Skip Williams. Flame propagation enhancement by plasma excitation of oxygen. Part II: Effects of O2(a1Δg). *Combustion and Flame*, 157(10):1916–1928, October 2010, doi:10.1016/j.combustflame.2010.02.004.

[26] G. D. Stancu, F. Kaddouri, D. A. Lacoste, and C. O. Laux. Investigations of rapid plasma chemistry generated by nanosecond discharges in air at atmospheric pressure using advanced optical diagnostics. *40th AIAA Plasmadynamics and Lasers Conference*, (June):1–7, 2009, doi:10.2514/6.2009-3593.

[27] G D Stancu, F Kaddouri, D A Lacoste, and C O Laux. Atmospheric pressure plasma diagnostics by OES, CRDS and TALIF. *Journal of Physics D: Applied Physics*, 43(12):124002, March 2010, doi:10.1088/0022-3727/43/12/124002.

[28] Jiajian Zhu. *Optical Diagnostics of Non-thermal Plasmas and Plasma-assisted Combustion.* Thesis, Lund University, 2015.

[29] Massood Tabib-Azar and Pradeep Pai. Microplasma Field Effect Transistors. *Micromachines*, 8(4):117, April 2017, doi:10.3390/mi8040117.

[30] Yu. P. Raizer. *Gas Discharge Physics*, volume 1. Springer, 1991.

[31] Ulrich Kogelschatz. Dielectric-barrier discharges: Their history, discharge physics, and industrial applications. *Plasma chemistry and plasma processing*, 23(1):1–46, 2003, doi:10.1023/A:1022470901385.

[32] Xueji Xu. Dielectric barrier discharge—properties and applications. *Thin solid films*, 390(1-2):237–242, 2001, doi:10.1016/S0040-6090(01)00956-7.

[33] Andreas Schutze, James Y Jeong, Steven E Babayan, Jaeyoung Park, Gary S Selwyn, and Robert F Hicks. The atmospheric-pressure plasma jet: A review and comparison to other plasma sources. *IEEE transactions on plasma science*, 26(6):1685–1694, 1998, doi:10.1109/27.747887.

[34] H Eichhorn, KH Schoenbach, and T Tessnow. Paschen's law for a hollow cathode discharge. *Applied physics letters*, 63(18):2481–2483, 1993, doi:10.1063/1.110455.

[35] A Czernichowski. Gliding arc: Applications to engineering and environment control. *Pure and Applied Chemistry*, 66(6):1301–1310, 1994, doi:10.1351/pac199466061301.

[36] Michael R. Winchester and Richard Payling. Radio-frequency glow discharge spectrometry:: A critical review. *Spectrochimica Acta Part B: Atomic Spectroscopy*, 59(5):607–666, May 2004, doi:10.1016/j.sab.2004.02.013.

[37] Yu A Lebedev. Microwave discharges: Generation and diagnostics. In *Journal of Physics: Conference Series*, volume 257, page 012016. IOP Publishing, 2010.

[38] David Z Pai, Deanna A Lacoste, and Christophe O Laux. Transitions between corona, glow, and spark regimes of nanosecond repetitively pulsed discharges in air at atmospheric pressure. *Journal of Applied Physics*, 107(9):093303, 2010, doi:10.1063/1.3309758.

[39] I Adamovich, S D Baalrud, A Bogaerts, P J Bruggeman, M Cappelli, V Colombo, U Czarnetzki, U Ebert, J G Eden, P Favia, D B Graves, S Hamaguchi, G Hieftje, M Hori, I D Kaganovich, U Kortshagen, M J Kushner, N J Mason, S Mazouffre, S Mededovic Thagard, H-R Metelmann, A Mizuno, E Moreau, A B Murphy, B A Niemira, G S Oehrlein,

Z Lj Petrovic, L C Pitchford, Y-K Pu, S Rauf, O Sakai, S Samukawa, S Starikovskaia, J Tennyson, K Terashima, M M Turner, M C M van de Sanden, and A Vardelle. The 2017 Plasma Roadmap: Low temperature plasma science and technology. *Journal of Physics D: Applied Physics*, 50(32):323001, August 2017, doi:10.1088/1361-6463/aa76f5.

[40] GW McClure. LOW-PRESSURE GLOW DISCHARGE. *Applied Physics Letters*, 2(12):233–234, 1963, doi:10.1063/1.1753749.

[41] S Kanazawa, Moriwaki Kogoma, T Moriwaki, and S Okazaki. Stable glow plasma at atmospheric pressure. *Journal of Physics D: Applied Physics*, 21(5):838, 1988, doi:10.1088/0022-3727/21/5/028.

[42] T Yokoyama, Moriwaki Kogoma, T Moriwaki, and S Okazaki. The mechanism of the stabilisation of glow plasma at atmospheric pressure. *Journal of Physics D: Applied Physics*, 23(8):1125, 1990, doi:10.1088/0022-3727/23/8/021.

[43] Francoise Massines, Ahmed Rabehi, Philippe Decomps, Rami Ben Gadri, Pierre Ségur, and Christian Mayoux. Experimental and theoretical study of a glow discharge at atmospheric pressure controlled by dielectric barrier. *Journal of Applied Physics*, 83(6):2950–2957, 1998, doi:10.1063/1.367051.

[44] J-S Chang, Phil A Lawless, and Toshiaki Yamamoto. Corona discharge processes. *IEEE Transactions on plasma science*, 19(6):1152–1166, 1991, doi:10.1109/27.125038.

[45] A Fridman, A Chirokov, and A Gutsol. Non-thermal atmospheric pressure discharges. *Journal of Physics D: Applied Physics*, 38(2):R1, 2005, doi:10.1088/0022-3727/38/2/R01.

[46] Werner von Siemens. Ueber die elektrostatische Induction und die Verzögerung des Stroms in Flaschendrähten. *Annals de chime et de physique*, 102:66, 1857, doi:10.1002/andp.18571780905.

[47] G Borcia, CA Anderson, and NMD Brown. Dielectric barrier discharge for surface treatment: Application to selected polymers in film and fibre form. *Plasma Sources Science and Technology*, 12(3):335, 2003, doi:10.1088/0963-0252/12/3/306.

[48] Yushi Takenaka, Masaki Kuzumoto, Koji Yasui, Shigenori Yagi, and Motoshi Tagashira. High power and high focusing CWCO/sub 2/laser using an unstable resonator with a phase-unifying output coupler. *IEEE journal of quantum electronics*, 27(11):2482–2487, 1991, doi:10.1109/3.100887.

[49] S Wieneke, S Born, and W Viöl. Sealed-off CO2 lasers excited by an all-solid-state 0.6 MHz generator. *Journal of Physics D: Applied Physics*, 33(11):1282, 2000, doi:10.1088/0022-3727/33/11/306.

[50] B Gellert and U Kogelschatz. Generation of excimer emission in dielectric barrier discharges. *Applied Physics B*, 52(1):14–21, 1991, doi:10.1007/BF00405680.

[51] Karl H Schoenbach, Ahmed El-Habachi, Mohamed M Moselhy, Wenhui Shi, and Robert H Stark. Microhollow cathode discharge excimer lamps. *Physics of plasmas*, 7(5):2186–2191, 2000, doi:10.1063/1.874039.

[52] Kiara Heuer, Martin A Hoffmanns, Erhan Demir, Sabrina Baldus, Christine M Volkmar, Mirco Röhle, Paul C Fuchs, Peter Awakowicz, Christoph V Suschek, and Christian Opländer. The topical use of non-thermal dielectric barrier discharge (DBD): Nitric oxide related effects on human skin. *Nitric oxide : biology and chemistry*, 44:52–60, 2015, doi:10.1016/j.niox.2014.11.015.

[53] JY Jeong, SE Babayan, VJ Tu, J Park, I Henins, RF Hicks, and GS Selwyn. Etching materials with an atmospheric-pressure plasma jet. *Plasma Sources Science and Technology*, 7(3):282, 1998, doi:10.1088/0963-0252/7/3/005.

[54] Juergen Friedrich Kolb, A-A H Mohamed, Robert O Price, R James Swanson, Angela Bowman, RL Chiavarini, M Stacey, and KH Schoenbach. Cold atmospheric pressure air plasma jet for medical applications. *Applied Physics Letters*, 92(24):241501, 2008, doi:10.1063/1.2940325.

[55] SE Babayan, JY Jeong, VJ Tu, J Park, GS Selwyn, and RF Hicks. Deposition of silicon dioxide films with an atmospheric-pressure plasma jet. *Plasma Sources Science and Technology*, 7(3):286, 1998, doi:10.1088/0963-0252/7/3/006.

[56] Yuri P Raizer, Mikhail N Shneider, and Nikolai A Yatsenko. *Radio-Frequency Capacitive Discharges*. CRC Press, 2017.

[57] Carlos M Ferreira and Michel Moisan. *Microwave Discharges: Fundamentals and Applications*, volume 302. Springer Science & Business Media, 2013.

[58] Jiajian Zhu, Andreas Ehn, Jinlong Gao, Chengdong Kong, Marcus Aldén, Mirko Salewski, Frank Leipold, Yukihiro Kusano, and Zhongshan Li. Translational, rotational, vibrational and electron temperat-

ures of a gliding arc discharge. *Optics express*, 25(17):20243–20257, 2017, doi:10.1364/OE.25.020243.

[59] A. Czernichowski, H. Nassar, A. Ranaivosoloarimanana, A.A. Fridman, M. Simek, K. Musiol, E. Pawelec, and L. Dittrichova. Spectral and Electrical Diagnostics of Gliding Arc. *Acta Physica Polonica A*, 89(5-6):595–603, May 1996, doi:10.12693/APhysPolA.89.595.

[60] Weizong Wang, Danhua Mei, Xin Tu, and Annemie Bogaerts. Gliding arc plasma for CO2 conversion: Better insights by a combined experimental and modelling approach. *Chemical Engineering Journal*, 330:11–25, 2017, doi:10.1016/j.cej.2017.07.133.

[61] SR Sun, HX Wang, DH Mei, X Tu, and A Bogaerts. CO2 conversion in a gliding arc plasma: Performance improvement based on chemical reaction modeling. *Journal of CO2 Utilization*, 17:220–234, 2017, doi:10.1016/j.jcou.2016.12.009.

[62] Xin Tu and J Christopher Whitehead. Plasma dry reforming of methane in an atmospheric pressure AC gliding arc discharge: Co-generation of syngas and carbon nanomaterials. *International Journal of Hydrogen Energy*, 39(18):9658–9669, 2014, doi:10.1016/j.ijhydene.2014.04.073.

[63] Jinlong Gao, Jiajian Zhu, Andreas Ehn, Marcus Aldén, and Zhongshan Li. In-situ non-intrusive diagnostics of toluene removal by a gliding arc discharge using planar laser-induced fluorescence. *Plasma Chemistry and Plasma Processing*, 37(2):433–450, 2017, doi:10.1007/s11090-016-9771-9.

[64] Fengsen Zhu, Xiaodong Li, Hao Zhang, Angjian Wu, Jianhua Yan, Mingjiang Ni, Hanwei Zhang, and Alfons Buekens. Destruction of toluene by rotating gliding arc discharge. *Fuel*, 176:78–85, 2016, doi:10.1016/j.fuel.2016.02.065.

[65] André Anders. *Cathodic Arcs: From Fractal Spots to Energetic Condensation*, volume 50. Springer Science & Business Media, 2009.

[66] Alexander Fridman, Sergei Nester, Lawrence A Kennedy, Alexei Saveliev, and Ozlem Mutaf-Yardimci. Gliding arc gas discharge. *Progress in energy and combustion science*, 25(2):211–231, 1999, doi:10.1016/S0360-1285(98)00021-5.

[67] IV Kuznetsova, NY Kalashnikov, AF Gutsol, AA Fridman, and LA Kennedy. Effect of "overshooting" in the transitional regimes of the low-current gliding arc discharge. *Journal of Applied Physics*, 92(8):4231–4237, 2002, doi:10.1063/1.1505682.

[68] Alexander Fridman and Lawrence A Kennedy. *Plasma Physics and Engineering*. CRC press, 2004.

[69] Ozlem Mutaf-Yardimci, Alexei V Saveliev, Alexander A Fridman, and Lawrence A Kennedy. Thermal and nonthermal regimes of gliding arc discharge in air flow. *Journal of Applied Physics*, 87(4):1632–1641, 2000, doi:10.1063/1.372071.

[70] Yukihiro Kusano, Mirko Salewski, Frank Leipold, Jiajian Zhu, Andreas Ehn, Zhongshan Li, and Marcus Aldén. Stability of alternating current gliding arcs. *The European Physical Journal D*, 68(10):319, 2014, doi:10.1140/epjd/e2014-50343-8.

[71] B Benstaali, P Boubert, BG Cheron, A Addou, and JL Brisset. Density and rotational temperature measurements of the OH and NO radicals produced by a gliding arc in humid air. *Plasma chemistry and plasma processing*, 22(4):553–571, 2002, doi:10.1023/A:1021371529955.

[72] Takao Matsumoto, Douyan Wang, Takao Namihira, and Hidenori Akiyama. Energy Efficiency Improvement of Nitric Oxide Treatment Using Nanosecond Pulsed Discharge. *IEEE Transactions on Plasma Science*, 38(10):2639–2643, October 2010, doi:10.1109/TPS.2010.2045903.

[73] David Z. Pai, Kostya (Ken) Ostrikov, Shailesh Kumar, Deanna A. Lacoste, Igor Levchenko, and Christophe O. Laux. Energy efficiency in nanoscale synthesis using nanosecond plasmas. *Scientific Reports*, 3(1):1221, December 2013, doi:10.1038/srep01221.

[74] S. M. Starikovskaia. Plasma-assisted ignition and combustion: Nanosecond discharges and development of kinetic mechanisms. *Journal of Physics D: Applied Physics*, 2014, doi:10.1088/0022-3727/47/35/353001.

[75] E J M van Heesch, G J J Winands, and A J M Pemen. Evaluation of pulsed streamer corona experiments to determine the O^* radical yield. *Journal of Physics D: Applied Physics*, 41(23):234015, December 2008, doi:10.1088/0022-3727/41/23/234015.

[76] Ryo Ono, Yusuke Nakagawa, and Tetsuji Oda. Effect of pulse width on the production of radicals and excited species in a pulsed positive corona discharge. *Journal of Physics D: Applied Physics*, 44(48):485201, December 2011, doi:10.1088/0022-3727/44/48/485201.

[77] Douyan Wang and Takao Namihira. Nanosecond pulsed streamer discharges: II. Physics, discharge characterization and plasma processing.

Plasma Sources Science and Technology, 29(2):023001, February 2020, doi:10.1088/1361-6595/ab5bf6.

[78] Ryo Ono. Optical diagnostics of reactive species in atmospheric-pressure nonthermal plasma. *Journal of Physics D: Applied Physics*, 49(8):083001, March 2016, doi:10.1088/0022-3727/49/8/083001.

[79] Jiajian Zhu, Yukihiro Kusano, and Zhongshan Li. *Atmospheric Pressure Plasmas: Processes, Technology and Applications*. New York: Nova Science, Chapter2, 2016.

[80] V. M. Donnelly. Plasma electron temperatures and electron energy distributions measured by trace rare gases optical emission spectroscopy. *Journal of Physics D: Applied Physics*, 37(19):R217–R236, September 2004, doi:10.1088/0022-3727/37/19/R01.

[81] Jiajian Zhu, Zhiwei Sun, Zhongshan Li, Andreas Ehn, Marcus Aldén, Mirko Salewski, Frank Leipold, and Yukihiro Kusano. Dynamics, OH distributions and UV emission of a gliding arc at various flow-rates investigated by optical measurements. *Journal of Physics D: Applied Physics*, 47(29):295203, July 2014, doi:10.1088/0022-3727/47/29/295203.

[82] Jiajian Zhu, Jinlong Gao, Andreas Ehn, Marcus Aldén, Zhongshan Li, Dmitry Moseev, Yukihiro Kusano, Mirko Salewski, Andreas Alpers, Peter Gritzmann, et al. Measurements of 3D slip velocities and plasma column lengths of a gliding arc discharge. *Applied Physics Letters*, 106(4):044101, 2015, doi:10.1063/1.4906928.

[83] I. V. Adamovich, I. Choi, N. Jiang, J.-H. Kim, S. Keshav, W. R. Lempert, E. Mintusov, M. Nishihara, M. Samimy, and M. Uddi. Plasma assisted ignition and high-speed flow control: Non-thermal and thermal effects. *Plasma Sources Science and Technology*, 18(3):034018, July 2009, doi:10.1088/0963-0252/18/3/034018.

[84] P J Bruggeman, N Sadeghi, D C Schram, and V Linss. Gas temperature determination from rotational lines in non-equilibrium plasmas: A review. *Plasma Sources Science and Technology*, 23(2):023001, April 2014, doi:10.1088/0963-0252/23/2/023001.

[85] Banwell, Colin N and McCash, Elaine M and others. *Fundamentals for Molecular Spectroscopy*. McGraw-Hill, 1994.

[86] K. Huber. *Molecular Spectra and Molecular Structure: IV. Constants of Diatomic Molecules*. Springer Science & Business Media, June 2013.

[87] R. S. Mulliken. Interpretation of the Atmospheric Oxygen Bands; Electronic Levels of the Oxygen Molecule. *Nature*, 122(3075):505–505, October 1928, doi:10.1038/122505a0.

[88] Brian J. Drouin, D. Chris Benner, Linda R. Brown, Matthew J. Cich, Timothy J. Crawford, V. Malathy Devi, Alexander Guillaume, Joseph T. Hodges, Eli J. Mlawer, David J. Robichaud, Fabiano Oyafuso, Vivienne H. Payne, Keeyoon Sung, Edward H. Wishnow, and Shanshan Yu. Multispectrum analysis of the oxygen A-band. *Journal of Quantitative Spectroscopy and Radiative Transfer*, 186:118–138, January 2017, doi:10.1016/j.jqsrt.2016.03.037.

[89] Harold D. Babcock and Luise Herzberg. Fine Structure of the Red System of Atmospheric Oxygen Bands. *The Astrophysical Journal*, 108:167, September 1948, doi:10.1086/145062.

[90] Colin M. Western. PGOPHER: A program for simulating rotational, vibrational and electronic spectra. *Journal of Quantitative Spectroscopy and Radiative Transfer*, 186:221–242, January 2017, doi:10.1016/j.jqsrt.2016.04.010.

[91] Bo Zhou, Christian Brackmann, Qing Li, Zhenkan Wang, Per Petersson, Zhongshan Li, Marcus Aldén, and Xue-song Bai. Distributed reactions in highly turbulent premixed methane/air flames: Part I. Flame structure characterization. *Combustion and Flame*, 162(7):2937–2953, July 2015, doi:10.1016/j.combustflame.2014.12.021.

[92] M. Röder, T. Dreier, and C. Schulz. Simultaneous measurement of localized heat-release with OH/CH2O–LIF imaging and spatially integrated OH chemiluminescence in turbulent swirl flames. *Proceedings of the Combustion Institute*, 34(2):3549–3556, January 2013, doi:10.1016/j.proci.2012.06.102.

[93] Elias Kristensson, Joakim Bood, Marcus Alden, Emil Nordström, Jiajian Zhu, Sven Huldt, Per-Erik Bengtsson, Hampus Nilsson, Edouard Berrocal, and Andreas Ehn. Stray light suppression in spectroscopy using periodic shadowing. *Optics Express*, 22(7):7711, April 2014, doi:10.1364/OE.22.007711.

[94] Miaoxin Gong, Haisol Kim, Jim Larsson, Torsten Methling, Marcus Aldén, Elias Kristensson, Christian Brackmann, Tina Eschrich, Matthias Jäger, Wolfgang Kiefer, Wolfgang Kiefer, and Andreas Ehn. Fiber-based stray light suppression in spectroscopy using periodic shadowing. *Optics Express*, 29(5):7232–7246, March 2021, doi:10.1364/OE.410517.

[95] M L Meade. Advances in lock-in amplifiers. *Journal of Physics E: Scientific Instruments*, 15(4):395–403, April 1982, doi:10.1088/0022-3735/15/4/001.

[96] Elias Kristensson, Zheming Li, Edouard Berrocal, Mattias Richter, and Marcus Aldén. Instantaneous 3D imaging of flame species using coded laser illumination. *Proceedings of the Combustion Institute*, 36(3):4585–4591, January 2017, doi:10.1016/j.proci.2016.08.040.

[97] Andreas Ehn, Joakim Bood, Zheming Li, Edouard Berrocal, Marcus Aldén, and Elias Kristensson. FRAME: Femtosecond videography for atomic and molecular dynamics. *Light: Science & Applications*, 6(9):e17045–e17045, September 2017, doi:10.1038/lsa.2017.45.

[98] Vassily Kornienko, Elias Kristensson, Andreas Ehn, Antoine Fourriere, and Edouard Berrocal. Beyond MHz image recordings using LEDs and the FRAME concept. *Scientific Reports*, 10(1):16650, October 2020, doi:10.1038/s41598-020-73738-1.

[99] Karolina Dorozynska, Simon Ek, Vassily Kornienko, David Andersson, Alexandra Andersson, Andreas Ehn, and Elias Kristensson. Snapshot multicolor fluorescence imaging using double multiplexing of excitation and emission on a single detector. *Scientific Reports*, 11(1):20454, October 2021, doi:10.1038/s41598-021-99670-6.

[100] Simon Ek, Vassily Kornienko, and Elias Kristensson. Long sequence single-exposure videography using spatially modulated illumination. *Scientific Reports*, 10(1):18920, November 2020, doi:10.1038/s41598-020-75603-7.

[101] Karolina Dorozynska. *Frequency Recognition Algorithm for Multiple Exposures : Snapshot Imaging Using Coded Light*. Thesis, Lund University, 2020.

[102] JS Courtney-Pratt. A new method for the photographic study of fast transient phenomena. *Research; a journal of science and its applications*, 2(6):287–294, 1949.

[103] JS COURTNEYPRATT. A new photographic method for studying fast transient phenomena. *PROCEEDINGS OF THE ROYAL SOCIETY OF LONDON SERIES A-MATHEMATICAL AND PHYSICAL SCIENCES*, 204(1076):27–29, 1950.

[104] Zhensheng Tao, He Zhang, P. M. Duxbury, Martin Berz, and Chong-Yu Ruan. Space charge effects in ultrafast electron diffraction and

imaging. *Journal of Applied Physics*, 111(4):044316, February 2012, doi:10.1063/1.3685747.

[105] Chris H. Sarantos and John E. Heebner. Solid-state ultrafast all-optical streak camera enabling high-dynamic-range picosecond recording. *Optics Letters*, 35(9):1389, May 2010, doi:10.1364/OL.35.001389.

[106] TJ Dolan. Electron and ion collisions with water vapour. *Journal of Physics D: Applied Physics*, 26(1):4, 1993, doi:10.1088/0022-3727/26/1/002.

[107] Yukikazu Itikawa and Nigel Mason. Cross sections for electron collisions with water molecules. *Journal of Physical and Chemical reference data*, 34(1):1–22, 2005, doi:10.1063/1.1799251.

[108] Jinlong Gao, Chengdong Kong, Jiajian Zhu, Andreas Ehn, Tomas Hurtig, Yong Tang, Shuang Chen, Marcus Aldén, and Zhongshan Li. Visualization of instantaneous structure and dynamics of large-scale turbulent flames stabilized by a gliding arc discharge. *Proceedings of the Combustion Institute*, 37(4):5629–5636, 2019, doi:10.1016/j.proci.2018.06.030.

[109] Seiji Kanazawa, Hirokazu Kawano, Satoshi Watanabe, Takashi Furuki, Shuichi Akamine, Ryuta Ichiki, Toshikazu Ohkubo, Marek Kocik, and Jerzy Mizeraczyk. Observation of OH radicals produced by pulsed discharges on the surface of a liquid. *Plasma Sources Science and Technology*, 20(3):034010, 2011, doi:10.1088/0963-0252/20/3/034010.

[110] Ryo Ono and Tetsuji Oda. OH radical measurement in a pulsed arc discharge plasma observed by a LIF method. *IEEE Transactions on Industry applications*, 37(3):709–714, 2001, doi:10.1109/28.924749.

[111] Chengdong Kong, Jinlong Gao, Jiajian Zhu, Andreas Ehn, Marcus Aldén, and Zhongshan Li. Characterization of an AC glow-type gliding arc discharge in atmospheric air with a current-voltage lumped model. *Physics of Plasmas*, 24(9):093515, September 2017, doi:10.1063/1.4986296.

[112] Chengdong Kong, Jinlong Gao, Jiajian Zhu, Andreas Ehn, Marcus Aldén, and Zhongshan Li. Effect of turbulent flow on an atmospheric-pressure AC powered gliding arc discharge. *Journal of Applied Physics*, 123(22):223302, June 2018, doi:10.1063/1.5026703.

[113] Chengdong Kong, Jinlong Gao, Jiajian Zhu, Andreas Ehn, Marcus Aldén, and Zhongshan Li. Re-igniting the afterglow plasma column of an AC powered gliding arc discharge in atmospheric-pressure air. *Applied Physics Letters*, 112(26):264101, June 2018, doi:10.1063/1.5041262.

[114] Chengdong Kong, Jinlong Gao, Jiajian Zhu, Andreas Ehn, Marcus Aldén, and Zhongshan Li. Characteristics of a Gliding Arc Discharge Under the Influence of a Laminar Premixed Flame. *IEEE Transactions on Plasma Science*, 47(1):403–409, January 2019, doi:10.1109/TPS.2018.2877126.

[115] Kajsa Larsson, Dina Hot, Jinlong Gao, Chengdong Kong, Zhongshan Li, Marcus Aldén, Joakim Bood, and Andreas Ehn. Instantaneous imaging of ozone in a gliding arc discharge using photofragmentation laser-induced fluorescence. *Journal of Physics D: Applied Physics*, 51(13):135203, April 2018, doi:10.1088/1361-6463/aab05b.

[116] Arman Subash. *Laser-Based Investigations of Combustion Phenomena in Gas Turbine Related Burners*. Thesis, Lund University, 2018.

[117] Arman Ahamed Subash, Robert Collin, Marcus Aldén, Atanu Kundu, and Jens Klingmann. Investigation of Hydrogen Enriched Methane Flame in a Dry Low Emission Industrial Prototype Burner at Atmospheric Pressure Conditions. In *ASME Turbo Expo 2017: Turbomachinery Technical Conference and Exposition*. American Society of Mechanical Engineers Digital Collection, August 2017.

[118] Arman Ahamed Subash, Robert Collin, Marcus Aldén, Atanu Kundu, and Jens Klingmann. Laser-Based Investigation on a Dry Low Emission Industrial Prototype Burner at Atmospheric Pressure Conditions. In *ASME Turbo Expo 2016: Turbomachinery Technical Conference and Exposition*. American Society of Mechanical Engineers Digital Collection, September 2016.

[119] Atanu Kundu, Jens Klingmann, Arman Ahamed Subash, and Robert Collin. Flame Stabilization and Emission Characteristics of a Prototype Gas Turbine Burner at Atmospheric Conditions. In *ASME Turbo Expo 2016: Turbomachinery Technical Conference and Exposition*. American Society of Mechanical Engineers Digital Collection, September 2016.

[120] Atanu Kundu, Jens Klingmann, Arman Ahamed Subash, and Robert Collin. Fuel Flexibility of a Multi-Staged Prototype Gas Turbine Burner. In *ASME Turbo Expo 2017: Turbomachinery Technical Conference and Exposition*. American Society of Mechanical Engineers Digital Collection, August 2017.

[121] Ying Huang and Vigor Yang. Dynamics and stability of lean-premixed swirl-stabilized combustion. *Progress in Energy and Combustion Science*, 35(4):293–364, August 2009, doi:10.1016/j.pecs.2009.01.002.

[122] Takao Namihira, Douyan Wang, Takao Matsumoto, Sho Okada, and Hidenori Akiyama. Introduction of Nano-seconds Pulsed Discharge Plasma and its Applications. *IEEJ Transactions on Fundamentals and Materials*, 129:7–14, January 2009, doi:10.1541/ieejfms.129.7.

[123] Douyan Wang, Takao Matsumoto, Takao Namihira, and Hidenori Akiyama. Development of Higher Yield Ozonizer Based on Nano-Seconds Pulsed Discharge. *Journal of Advanced Oxidation Technologies*, 13(1):71–78, January 2010, doi:10.1515/jaots-2010-0110.

Acknowledgments

First and foremost I would like to thank my supervisor Andreas Ehn. Thank you for being both supportive and encouraging. Your passion and enthusiasm for science have been inspiring me through the whole journal. I am really appreciated that I can always get your help when I needed, especially when I had problems in the lab. Our cheerful and purely scientific discussions make the so-called stressful PhD journal full of happy memories. I am 99% sure that no one else can be a better supervisor for me, and it could easily be 100% with THE BBQ at the wonderful garden of Ehn's House.

I would like to thank my co-supervisors Joakim Bood and Marcus Aldén. Thank you Joakim for being very helpful even when you were not officially my co-supervisor. When I could not figure out a complicated problem about fundamental physics, I always think about discussing with you. Thank you Marcus for providing such a wonderful division for PhD students. Although we do not talk that much, your "small" comments, suggestions and scientific opinions are often very helpful. In addition, although not as my official co-supervisors, I really appreciate the mentoring I got from Tomas Hurtig regarding plasma-related problems, Elias Kristensson regarding FRAME and Christian Brackmann regarding lasers. Thank you all!

The working environment at combustion physics is very relaxing, efficient and pleasant, for this I would like to thank all my colleagues, especially Minna Ramkull, Cecilia Bille, Igor Buzuk and the former and current head of the division, Marcus Aldén and Per-Erik Bengtsson.

I would also like to thank Tomas Brage, for introducing me to Lund. Your generosity and willingness to help international students with multicultural background showed me that you are not only an accomplished professor but also a true educator.

From the very beginning, I actually missed the deadline for the application of

this position. Thankfully Zhongshan Li was so generous to introduce me to such a good position. I would also like to thank Bo Zhou, for the first few months of my PhD when we worked together in the lab. Although not easy, I did learn a lot from you.

Sharing equipments, thoughts and space in the lab are not easy. I am really appreciated for all my colleagues who are so generous to share with me, especially Dina Hot, Johan Zetterberg, Elias Kristensson, Joakim Bood, Mattias Richter, Alexander Konnov, Marco Lubrano Lavadera, Maria Ruchkina, Pengji Ding, Elin Malmqvist, Haisol Kim, Christian Brackmann and Per Samuelsson.

My dearest friends at combustion physics! Being a PhD student can be very hard sometimes, but working with nice colleagues makes it so much easier. Maria, you are an endless source of fun and excitement, I hope we can still ski together when we are at our 80's. Sandra, you are the nicest person I have ever met! Thanks for taking care of our office. Vasse, you are the best one to work with! Thanks for proofreading my OK-ish English writing, I hope you are not (yet) tired of correcting the same mistakes I made over and over again. My dear plasma group: Chengdong, your stubbornness towards science is a true virtue! Sebastian and Jonas, I could not tell how happy I am for your joining of the group. I enjoyed our Monday meetings very much! And also Kailun, thanks for working with me in the lab with an unconventional time schedule. Giota and Karolina, it is amazing that we actually managed to finish the 3D project in the end! I am also deeply impressed by the willingness to stand up for other people from both of you. Xin and Subash, somehow I ended up on the front cover of the nyheter while you two are the actual main contributor to the project. I hope you have enjoyed the project as much as I have. Haisol and Mannazhi, how pleasant to share almost all our PhD times together, thanks for being so tolerant to my harsh jokes on you all the time!

The list will never end but I have to, as once again I am writing at the last minute before the deadline. Christoffer, Pengji, Jim, Shen, Marco, Alex, David the Yrchmagnar, Ruike, Qingshuang, Zhenkan, Jinlong, Meng, Kailun, Edouard, Wubin, Sven-inge, and all my lovely colleagues, I will save my words on the personal copy I give to you later. It is almost 4am now, I sincerely hope you will not be too mad at me if I forgot your name or misspelled you name.

To my friends in the SPIE and OSA student chapter, Karolina, Isabel, Damiano, Haisol, Christoffer and Lisa; my friends in the Wechat group 索菲亚公园的邻居们, Xin, Qingshuang, Shichao, Lai; my friends from the Team Orchids, Magdalena, Samuel, Erik and Flip; and my friends from the badminton club: life is much easier and fun with all of you around!

Special thanks to my friends: Dr.Yang, Dr.Xian and Dr.Ding (应三位博士要求添加：排名不分先后). How lucky we are to still be friends after 15 years! Finally I am a Doctor too!!! Also Dr.Jia, thanks for your accompany from Chengdu to Shanghai and to Europe!

Finally I would like to thank my family, especially my mom and dad, for the endless love and support. I could never ever have done this without you. 谢谢我亲爱的家人给予我的爱与支持！我爱你们！ And my dearest Taoyan, for all your support and most importantly, for being there with me through the whole journey.

Printed by Media-Tryck, Lund 2022 NORDIC SWAN ECOLABEL 3041 0903

LUND UNIVERSITY

Division of Combustion Physics
Department of Physics

Lund University, Faculty of Engineering
ISBN: 978-91-8039-158-0
ISSN: 1102-8718
ISRN: LUTFD2/TFCP-242-SE